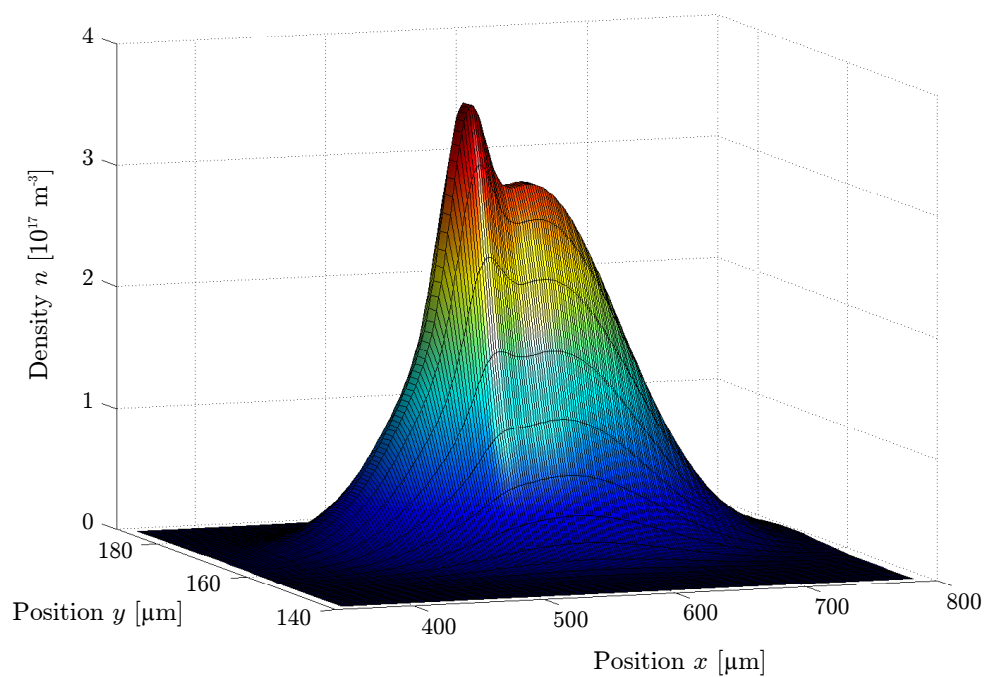


# A Crossed Optical Dipole Trap

Eine Diplomarbeit vorgelegt von

**Hannes Michael Gorniaczyk**

aus Schwäbisch Gmünd



Hauptberichter: Prof. Dr. TILMAN PFAU  
Mitberichter: Prof. Dr. PETER MICHLER

5. Physikalisches Institut Universität Stuttgart

15. Dezember 2011

## Erklärung

Hiermit erkläre ich, dass ich diese Arbeit selbständig verfasst und keine anderen als die von mir angegebenen Quellen und Hilfsmittel verwendet habe.

Stuttgart, den 15. Dezember 2011

Hannes Michael Gorniaczyk

## Cover Figure

The figure on the cover page shows the density distribution in a plane through the center of the crossed optical dipole trap as calculated in Section 5.3. The peak density is due to the characteristic dip in the potential landscape. This feature is referred to as *dimple*.

## Abstract

This thesis presents the setup of a crossed optical dipole trap, called *dimple*. The setup is characterized within experiments regarding the trap depth, the trap geometry and the stability in combination with dilute clouds of ultra-cold  $^{52}\text{Cr}$  atoms. Simulations of the particle dynamics in optical dipole traps support and clarify the experimental data. Simulating the cooling performance of demagnetization cooling the application of this technique in dimple trap geometries are suggested.

In dieser Diplomarbeit wird der Aufbau einer gekreuzten optischen Dipolfalle vorgestellt, den man *Dimple* nennt. Dieser Aufbau wird im Rahmen von Experimenten zur Fallentiefe, Fallengeometrie und Stabilität charakterisiert. Diese Experimente werden mit ultra-kalten verdünnten  $^{52}\text{Cr}$  Atomwolken durchgeführt. Die Messungen zu den Fallenfrequenzen werden mit Simulationen zur Teilchendynamik in optischen Dipolfallen unterlegt. Die Simulation zur Kühlleistung durch die Technik des Entmagnetisierungskühlens suggeriert, dieses Verfahren mit Dimple Fallengeometrien anzuwenden.

# Contents

<b>1</b>	<b>Introduction</b>	<b>3</b>
<b>2</b>	<b>Theory</b>	<b>4</b>
2.1	Ultra-Cold Gases . . . . .	4
2.1.1	Summary . . . . .	4
2.1.2	A Quantum Toolbox: Determining the Temperature . . . . .	7
2.2	Dipolar Interactions . . . . .	8
2.2.1	Introduction . . . . .	8
2.2.2	Demagnetization Cooling . . . . .	11
2.3	The Interaction between Light and Matter . . . . .	12
<b>3</b>	<b>Setup</b>	<b>15</b>
3.1	Loading a Hybrid Trap from a Beam . . . . .	15
3.2	Mechanical Setup . . . . .	17
3.3	Imaging . . . . .	17
3.4	Optics . . . . .	21
3.5	Power Characteristics . . . . .	23
3.6	Loading the Dimple . . . . .	27
<b>4</b>	<b>Trap Dynamics</b>	<b>28</b>
4.1	Simulations . . . . .	28
4.1.1	Harmonic Approximation . . . . .	28
4.1.2	Anharmonic Trap . . . . .	31
4.2	Experiments . . . . .	32
4.2.1	Laser Intensity Modulation . . . . .	33
4.2.2	Parametric Heating – Extraction of Results . . . . .	34
4.2.3	Influences on the Signal . . . . .	34
4.2.4	ODT ramp and Temperature. . . . .	36
4.2.5	The Position of the Dimple Focus. . . . .	37
4.2.6	Dimple Laser Power. . . . .	41
<b>5</b>	<b>Loading Performance</b>	<b>42</b>
5.1	Statistics . . . . .	42
5.2	The Temperature . . . . .	44
5.3	The Density Gain . . . . .	46
<b>6</b>	<b>The Stability of the Setup</b>	<b>52</b>
6.1	Lifetime . . . . .	52
6.2	Forced Evaporation . . . . .	53
<b>7</b>	<b>Prediction for Demagnetization Cooling</b>	<b>58</b>

**8 Summary and Outlook**

**62**

# Chapter 1

## Introduction

Being a growing field of study, ultra-cold gases with long-range interactions in particular gain more and more interest in the atomic physics community. Efforts have been made to even create a BOSE-EINSTEIN condensate of the most magnetic element, Dysprosium [26]. What makes elements with a large dipolar moment interesting? New quantum phases [11] can be studied and promising applications are established. A novel lossless cooling technique that bases on the dipolar momentum of quantum gases has been realized: demagnetization cooling [19].

We perform experiments with ultra-cold chromium ( $^{52}\text{Cr}$ ) atoms. With a magnetic moment of 6 BOHR magnetons  $\mu_B$ , dipolar interactions can play a considerable role in chromium compared to, e.g. alkali atoms. We have built up an experiment with a guided atomic beam that is continuously loaded into a hybrid magnetic trap and optical dipole trap [8]. For demagnetization cooling to be most efficient, the magnetic field and the temperature have to fulfill the ratio  $\frac{gs\mu_B B}{k_B T} \approx 1.31$ . The condition after the loading process is close to this criterion. Therefore, the application of this technique is suggested. The performance, however, is dependent on the geometry of the trap potential. In a harmonic potential, the cooling ratio  $\dot{T}$  is constant. But, using a dimple trap potential, the cooling rate will amplify with time. The self-amplification of the cooling rate is referred to as *runaway regime*.

This motivates to set up a a crossed optical dipole trap with two laser systems: one system crossing the other perpendicularly producing a narrow confinement.

In such a dimple configuration, we could investigate a second mechanism, that has not been studied experimentally for my knowledge. It is the loading of a conservative potential without dissipative processes, as described theoretically in [31]. Once atoms are in a deep potential – which could be realized with a dimple – collisions with incoming atoms can lead to an accumulation of particles in the potential only due to the mechanisms of elastic collisions which result in the loss of high-energy particles, *evaporation*. The prerequisite for this behavior has been stated [31]: The energy of the particle beam must not exceed one sixth of the potential depth. However, this condition will deviate in different trap geometries.

This work characterizes the setup of the dimple. It estimates the performance for demagnetization cooling and gives recommendations for possible modifications.

# Chapter 2

## Theory

The principle of operation in this work is to a considerably large extent based on the physics of light forces. Therefore, it is worthwhile studying the mechanisms that lead not only to an optical dipole trap itself, but also to a variety of properties that are discussed in this thesis. But still, the light-matter interaction is only the toolbox for the main subject of ultra-cold gases and BOSE-EINSTEIN-condensation with  $^{52}\text{Cr}$  atoms which will be subject to the first section. Since this thesis does not have its focus on theory of ultra-cold gases, we will not derive equations from first principles – this has already been done – but we will rather summarize all relevant properties and try and give intuitive pictures.

### 2.1 Ultra-Cold Gases

#### 2.1.1 Summary

Matter can be divided into two kinds of particles: bosons and fermions. They obey the BOSE and the FERMI-DIRAC statistics respectively. Symmetry considerations of the total wave function decide how one state corresponding to an energy level  $\epsilon$  of the system can be populated. The distribution functions are given by

$$f^{\text{FD}}(\epsilon) = \frac{1}{e^{(\epsilon-\mu)/(k_B T)} + 1} \quad (2.1)$$

$$f^{\text{BE}}(\epsilon) = \frac{1}{e^{(\epsilon-\mu)/(k_B T)} - 1} \quad (2.2)$$

and can be found in Figure 2.1.  $k_B = 1.3806488(13) * 10^{-23} \text{ J/K}^*$  denotes the BOLTZMANN constant and  $\mu$  is the chemical potential which accounts for particle conservation.

For high temperatures  $T$ , when  $k_B T/\mu \gg 1$ , the two distributions approximate the classical BOLTZMANN-distribution

$$f^{\text{B}}(\epsilon) = e^{(\mu-\epsilon)/(k_B T)}. \quad (2.3)$$

If we want to know which states are populated at a given temperature, we need to know the density of states. For a free particle in a Volume  $V$ , this is [30]

$$g(\epsilon) = \frac{V m^{3/2}}{\pi^2 \hbar^3 \sqrt{2}} \sqrt{\epsilon} \quad (2.4)$$

---

\*Source of all physical constants:  
The NIST Reference on Constants, Units and Uncertainty <http://physics.nist.gov> (2 Dec 2011).

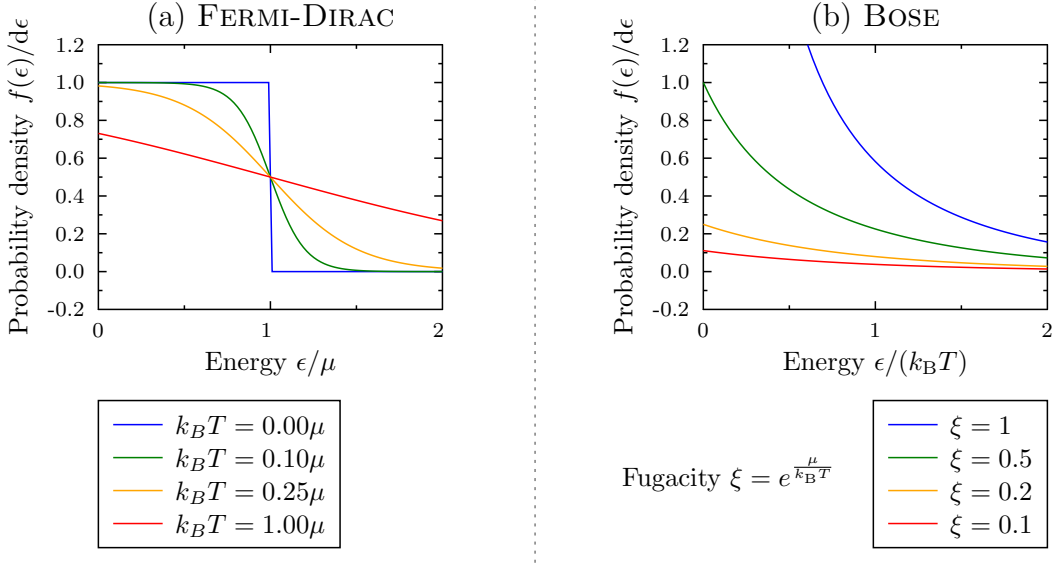


Figure 2.1: In FERMI-statistics (a), for  $T = 0$ , all states below the FERMI energy  $k_B T/\mu$  are occupied by one atom (PAULI exclusion principle). Note that the probability always corresponds to one state  $|k\rangle$ . If the energy  $\epsilon = \epsilon_k$  of state  $|k\rangle$  is degenerate, more than one atom can have the same energy. (An example is two electrons with different spins in a system without magnetic fields.) At finite temperatures, excited states get occupied, so the sharp boundary of the FERMI energy wipes out. In BOSE-statistics (b), states can be occupied multiple times (blue curve). At small temperatures, this leads to BOSE-EINSTEIN-condensation, i.e. a large fraction of atoms occupy one single state.

with  $m$  being the mass of the particle. For a particle in a 3D harmonic potential with frequencies  $(\omega_x, \omega_y, \omega_z)$ , the density of states writes

$$g(\epsilon) = \frac{1}{2\hbar^3 \omega_x \omega_y \omega_z} \epsilon^2. \quad (2.5)$$

We will now consider the case of  $N$  bosons without interactions – the *ideal Bose gas*. We introduce the fugacity [30]

$$\xi = e^{\frac{\mu}{k_B T}} \quad (2.6)$$

that includes the chemical potential. The BOSE-distribution thus writes

$$f^{\text{BE}}(\epsilon) = \frac{1}{e^{\epsilon/(k_B T)} \xi^{-1} - 1}. \quad (2.7)$$

It is plotted in Figure 2.1 (b) for various  $\xi$ .

For high temperatures, the chemical potential has to be smaller than the energy of the ground state  $\epsilon_g$  because the ground state is barely occupied at this condition. Also, since the distribution must be positive, the chemical potential must always be smaller than the energy of the ground state

$$f^{\text{BE}}(\epsilon) > 0 \Rightarrow \mu < \epsilon_g. \quad (2.8)$$

Therefore, an upper estimate of the mean occupation in any excited state  $|k\rangle$  with energy  $\epsilon_k$  can be stated [30]

$$f^{\text{BE}}(\epsilon_k) < \frac{1}{e^{(\epsilon_k - \epsilon_g)/(k_B T)} - 1} \quad \text{for } k \neq g. \quad (2.9)$$

With the condition that

$$N : \text{number of atoms} \quad (2.10)$$

is the available total occupation number, the difference between the total occupation of the excited states and  $N$  has to be the occupation of the ground state which can become very high. If the number of atoms occupying the ground state is in the order of  $N$ , it is called BOSE-EINSTEIN-condensation (BEC).

With further analysis [30] [21] [5], we find the *critical temperature*

$$T_C = \frac{\hbar\bar{\omega}}{k_B} \left( \frac{N}{\zeta(3)} \right)^{1/3} \quad (2.11)$$

at which pure quantum statistics leads to that phase transition, here calculated for a harmonic potential with a geometric mean oscillation frequency  $\bar{\omega} = (\omega_x\omega_y\omega_z)^{1/3}$ .  $\hbar = 1.054571726(47) * 10^{-34}$ Js is the reduced Planck constant and  $\zeta(3) \approx 2.6124$  is the RIEMANN zeta function:

$\zeta(\alpha) = \sum_{k=1}^{\infty} \frac{1}{k^\alpha}$  [30]. The energy of the particles  $k_B T_C$  is still much higher than the level spacings  $\hbar\omega_{i \in \{x,y,z\}}$  of the states in the potential. The tendency that bosons occupy one single state is also referred to as *Bosonic stimulation* or *Bose enhancement*.

In a figurative picture, one can also think of this mechanism in terms of the atomic wave functions with thermal DE BROGLIE wavelengths of

$$\lambda_{dB} = \frac{h}{\sqrt{2\pi m k_B T}}, \quad h = 2\pi\hbar : \text{Planck constant.} \quad (2.12)$$

At low temperatures,  $\lambda_{dB}$  becomes as large as the inter-atomic distance. Constructive interference of the wave functions will form one *giant matter wave*.

The critical temperature is dependent on the frequencies  $\omega_i$  and the atom number. Thus, it changes with experimental conditions. A significant parameter that classifies experiments in a unique way is the phase space density (PSD) [21]

$$\mathcal{D} = n\lambda_{dB}^3 \quad \text{with } n(\vec{r}) : \text{particle density at position } \vec{r}. \quad (2.13)$$

Equation (2.13) quantifies the figurative picture given above, since it compares the volume  $V_{dB}$  with edge length  $\lambda_{dB}$  with the volume  $V$  of one atom:

$$\mathcal{D} = \frac{V_{dB}}{V}. \quad (2.14)$$

From this formulation of the PSD, we expect the BOSE-EINSTEIN condensation to take place at  $\mathcal{D}_C \approx 10^0$ . In fact, a more accurate analysis [14] predicts the transition at

$$\mathcal{D}_C = \zeta\left(\frac{3}{2}\right) \approx 2.612. \quad (2.15)$$

**Interactions** As a matter of fact, there is a weak yet relevant interaction between the atoms, the s-wave scattering. This quantum scattering process can be modeled with the collision of hard spheres [3] [36]. The resultant interaction energy is only dependent on one single parameter, the scattering length  $a$  which can be thought of as the radii of the colliding spheres. For most elements, its value is about  $100a_0^*$ , with  $a_0 = 5.2917721092(17) * 10^{-11}$  m : BOHR radius.

A formalism for condensates is provided by the GROSS-PITAEVSKII-equation (GPE) within a mean field theory [30]. The time-independent version reads

$$\mu\phi(\vec{r}) = \left[ -\frac{\hbar^2}{2m}\nabla^2 + U(\vec{r}) + g|\phi|^2(\vec{r}, t) \right] \phi(\vec{r}, t). \quad (2.16)$$

\*For  $^{52}\text{Cr}$ , the scattering length is  $a = (112 \pm 14)a_0$  [37].

It is a Schrödinger equation with a nonlinear part added. The scattering length is included in the parameter  $g = \frac{4\pi\hbar^2 a}{m}$ . Since  $\phi(\vec{r})$  denotes the order parameter of the condensate and  $|\phi(\vec{r})|^2$  is the local density, the interaction energy depends on the density. We can compare the kinetic energy with the interaction energy [14]:

$$\frac{E_{\text{int}}}{E_{\text{kin}}} = N \frac{a}{a_{\text{ho}}}. \quad (2.17)$$

$a_{\text{ho}} = \sqrt{\frac{\hbar}{m\omega}}$  is the quantum harmonic oscillator length. If the kinetic energy can be neglected – referred to as THOMAS-FERMI regime – this giant matter wave resembles the shape of the confining potential landscape. In case of a parabolic potential, the density has the shape of an inverse parabola.

### 2.1.2 A Quantum Toolbox: Determining the Temperature

The determination of the temperature is essential to calculate the phase space density, see Equation (2.12). For this, one needs to analyze the dynamics of the thermal cloud. In all of the cases of

- a purely thermal atomic cloud,
- BOSE enhancement and
- a BEC

the wings of the density profiles along the ( $i \in \{x, y, z\}$ )-axis can be approximated [21] by a Gaussian

$$n_i(r_i) = n_0 \exp\left(-\frac{(r_i - r_{i,0})^2}{2\sigma_i^2}\right) \quad (2.18)$$

with the position  $r = (x, y, z)$ , the position  $r_0 = (x_0, y_0, z_0)$  of maximum particle density  $n_0$  and the width  $\sigma_i$  of the thermal cloud. The wings contain a fraction of the thermal cloud which is always present. Only in the thermal cloud, the temperature is well-defined and can thus be measured. The thermal cloud part performs an expansion  $\sigma_i = \sigma_i(t)$  as soon as all potentials originating from magnetic and light fields are switched off at time  $t = 0$ . After the time  $t = t_{\text{TOF}}$ , the cloud size  $\sigma_i$  is given by [21]

$$\sigma_i = \sigma_i^* \sqrt{1 + \omega_i^2 t_{\text{TOF}}^2}. \quad (2.19)$$

The star (\*) will denote in situ data, here  $\sigma^* = \sigma(t_{\text{TOF}} = 0)$ . There is an expression for the in situ cloud width at temperature  $T$  [21]

$$\sigma_i^* = \sqrt{2k_{\text{B}}T/(m\omega_i^2)}. \quad (2.20)$$

We substitute Equation (2.20) in Equation (2.19)

$$\boxed{\sigma_i = \sqrt{2k_{\text{B}}T/(m\omega_i^2) + 2k_{\text{B}}Tt^2/m}} \quad (2.21)$$

and get a helpful formula for the dynamics of a free expanding cloud. For large times  $t_{\text{TOF}} \gg \omega_i^{-1}$ , this function becomes linear in time:

$$\sigma_i = \sqrt{\frac{2k_{\text{B}}Tt_{\text{TOF}}^2}{m}} = t_{\text{TOF}} \sqrt{\frac{2k_{\text{B}}T}{m}}. \quad (2.22)$$

This simple dependency can and will be used to derive the temperature of a thermal cloud:

$$T = \left(\frac{\sigma_i}{t_{\text{TOF}}}\right)^2 \frac{m}{2k_{\text{B}}}. \quad (2.23)$$

The validity of this approximation can be investigated by varying  $t_{\text{TOF}}$  and probing the linearity of  $\sigma_i$ .

## 2.2 Dipolar Interactions

### 2.2.1 Introduction

New phenomena come to play if we prepare ultra-cold clouds with atoms or molecules that feature a high dipolar momentum. Examples are  $^{52}\text{Cr}$ ,  $^{166}\text{Er}$ ,  $^{164}\text{Dy}$  and atoms in RYDBERG states\*. Heteronuclear molecules can exhibit a much higher dipolar momentum. However, due to limited cooling techniques, they have not been BOSE-condensed yet.

**Dipolar Momentum and Energy of a Single Atom.** We treat the case of monatomic species in small electric fields in which the dipolar momentum can only be magnetic. It originates in the electronic and nucleonic spins and angular momenta. Depending on the mutual coupling strengths of the momenta and on the modulus  $B$  of the applied magnetic field  $\vec{B}$ , the single angular momenta and spins add up to a total angular momentum in different ways. In either case, the resultant total angular momentum of the atom precesses about the magnetic field with the quantization restriction for the projection  $m_F\hbar$  of the total angular momentum  $F$

$$m_F \in \{-F, -F + 1, \dots, F - 1, F\}. \quad (2.24)$$

The electronic dipolar momenta usually dominate the nuclear dipolar momenta due to the high mass of the nucleus because either magnetic momentum is in the order of the BOHR magneton  $\mu_B = \frac{e\hbar}{2m_e}$  and nuclear magneton  $\frac{e\hbar}{2m_p}$  respectively, with the elementary charge  $e = 1.602176565(35) * 10^{-19}$  C, the electron rest mass  $m_e = 9.10938291(40) * 10^{-31}$  kg and the proton mass  $m_p = 1.672621777(74) * 10^{-27}$  kg. For that reason, and because the element of study in this work,  $^{52}\text{Cr}$ , exhibits a total nuclear angular momentum of zero, we shall only treat the magnetic momentum of the electron.

The  $z$ -component of the electronic magnetic momentum is given by [5]

$$\mu_z = -g_J\mu_B m_J \quad (2.25)$$

where  $g_J$  denotes the LANDÉ factor<sup>†</sup>. The negative sign is due to the negative electron charge. The potential energy of the atom is given by

$$-\vec{\mu} \cdot \vec{B} = -\mu_z B = g_J\mu_B m_J B. \quad (2.26)$$

In case of an angular momentum of zero, e.g.  $^{52}\text{Cr}$ , the electron spin is the only contribution to the magnetic momentum. We shall write  $m_J = m_S$  and  $g_J = g_S$ .

**Interaction between Dipoles.** The atoms mutually interact with their dipolar momentum. The interaction energy is [23]

$$U_{\text{dd}} = \frac{\mu_0\mu^2}{2\pi} \frac{(\vec{e}_1 \cdot \vec{e}_2)r^2 - 3(\vec{e}_1 \cdot \vec{r})(\vec{e}_2 \cdot \vec{r})}{r^5} \quad (2.27)$$

for two particles with relative position  $\vec{r}$ , distance  $r$  and dipolar momenta polarized along  $\vec{e}_1$  and  $\vec{e}_2$  respectively as visualized in Figure 2.2.  $\mu_0 = 4\pi * 10^{-7} \frac{\text{N}}{\text{m}^2}$  denotes the permeability of vacuum and  $\mu = |\vec{\mu}|$ . If the atoms are polarized in the same direction, Equation (2.27) simplifies:

$$U_{\text{dd}} = \frac{\mu_0\mu^2}{2\pi} \frac{1 - 3\cos^2(\theta)}{r^3} \quad (2.28)$$

\*RYDBERG atoms show high polarizabilities and interact via coupling of oscillating dipolar momenta. It has been shown [25] that it is even possible to create homonuclear molecules with permanent electric dipolar momenta. Such molecules are realized with one atom in the ground state and one atom in the RYDBERG state.

<sup>†</sup>The LANDÉ factor is a measure for the ratio of the dipolar momentum and the total angular momentum. For the system of a single electron spin  $g_F \approx 2$ .

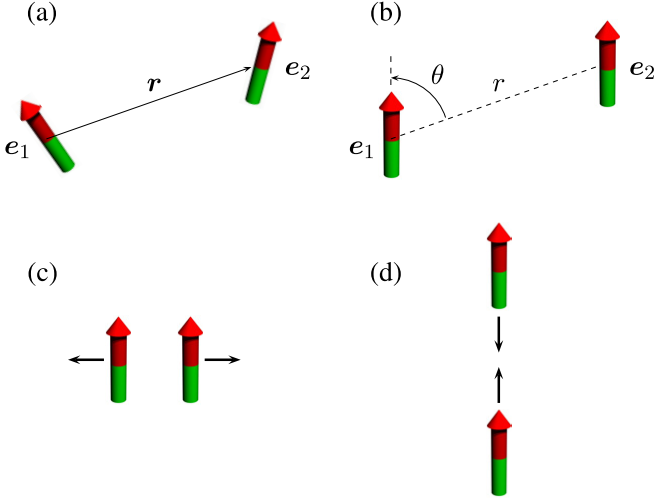


Figure 2.2: The orientations of two dipoles. (a) The general case of arbitrary orientations is considered in Equation (2.27). (b) Dipoles with a parallel alignment (e.g. along an applied magnetic field) are treated in Equation (2.28). Depending on  $\theta$ , the interaction is repulsive (c) at  $\theta = \pi/2$  or attractive (d) with  $\theta = \pi$  Source: [23].

Both equations (2.27) and (2.28) show the dependence on the square root of the magnetic momentum. This is why for  $^{52}\text{Cr}$  with  $m_S = \pm 3$  the interaction is  $6^2 = 36$  times larger\* than for alkali atoms with  $m_S = \pm 1/2$ .

The difference of the dipole-dipole interaction compared to the contact interaction [16] is the long-range and anisotropic character of the dipolar interaction. The anisotropy is self-evident due to the angular dependency. The long-range character is implied by the divergence of the total interaction potential at large distances [23] [2].

The dipolar interaction can be neglected in many phenomena because it is dominated by the contact interaction. Near magnetic fields at which FESHBACH resonances [20] [37] occur, the contact interaction can effectively be reduced until a regime is reached where the dipolar character of the atomic cloud becomes dominant [35]. Experiments in which the dipolar character is expressed most obviously are the  $d$ -wave collapse of a BEC [24] and the geometry-dependent stability of atomic clouds [27] [22].

**Dipolar Relaxation** When two dipolar particles scatter, they can perform elastic collisions, at which the internal states stay unmodified. Inelastic collisions are also possible and associated with the transition of the magnetic quantum number  $m_S \rightarrow m_S \pm 1$  in case of a pure spin magnetic momentum. If one of the two atoms changes its spin, it is referred to as *single spin flip* whereas we call the transition of both spins a *double spin flip*. Figure 2.3 visualizes and explains the scattering process.

The mechanism can be described with quantum scattering theory with the interaction energy of Equation (2.27) accounting for the dipolar part of the interaction [18] [12]. Since the interaction is anisotropic, it is necessary to average over all scattering angles if we want an expression for the mean cross sections for elastic and inelastic collisions. These cross sections are given by [12]

$$\sigma_0 = \frac{16\pi}{45} S^4 \left( \frac{\mu_0 (g_S \mu_B)^2 m}{4\pi \hbar^2} \right)^2 [1 + h(1)] \quad (2.29)$$

$$\sigma_1 = \frac{8\pi}{15} S^3 \left( \frac{\mu_0 (g_S \mu_B)^2 m}{4\pi \hbar^2} \right)^2 [1 + h(k_f/k_i)] \frac{k_f}{k_i} \quad (2.30)$$

$$\sigma_2 = \frac{16\pi}{45} S^2 \left( \frac{\mu_0 (g_S \mu_B)^2 m}{4\pi \hbar^2} \right)^2 [1 + h(k_f/k_i)] \frac{k_f}{k_i} \quad (2.31)$$

where  $k_i$  and  $k_f$  are the moduli of the wave vectors of the reduced mass  $m/2$  and given by the

\*provided the states of the two species have the same LANDÉ factor

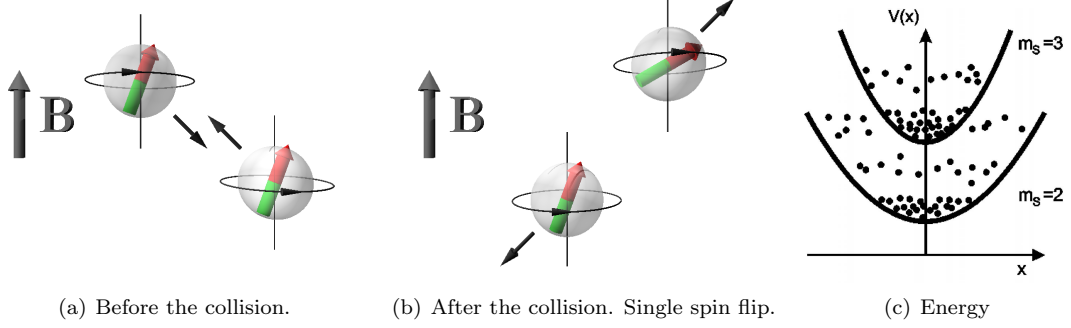


Figure 2.3: The kinetic energy can be stored or released in the magnetic potential of ZEEMAN substates (c). Since the magnetic potential is quantized, i.e. only distinct angles between magnetic momenta and the magnetic field are possible, not every collision changes the direction of the magnetic momenta. The magnetic momenta precess about the  $\vec{B}$  axis with the LARMOR frequency. In Figure 2.3(b), one atom has performed a single spin flip indicated with a larger angle between the magnetic field and the magnetic moment. Source of Figure 2.3 (c): [19].

kinetic energy

$$E_{\text{kin}} = \frac{\hbar^2 k^2}{m}. \quad (2.32)$$

For a single or double spin flip, the ratios  $k_f/k_i$  are given by

$$\frac{k_f}{k_i} = \sqrt{1 - \frac{mg_S\mu_B B}{2\hbar^2 k_i^2}} \quad (2.33)$$

$$\frac{k_f}{k_i} = \sqrt{1 - \frac{mg_S\mu_B B}{\hbar^2 k_i^2}} \quad (2.34)$$

respectively. The function  $h(x)$  is defined as

$$h(x) = -\frac{1}{2} - \frac{3}{8} \frac{(1-x^2)^2}{x+x^3} \log\left(\frac{(1-x)^2}{(1+x)^2}\right). \quad (2.35)$$

For the prediction of dipolar relaxation rates of a thermal cloud, we must account for the distribution of the relative velocities  $v$  given by the MAXWELL-BOLTZMANN distribution

$$f^{\text{MB}} = \sqrt{2/\pi} \left(\frac{m}{2k_B T}\right)^{3/2} v^2 \exp\left[-\frac{mv^2}{4k_B T}\right]. \quad (2.36)$$

The dipolar relaxation rates are given by [12]

$$\beta = \langle (\sigma_1 + 2\sigma_2)v \rangle_{\text{thermal}} = \int_0^\infty (\sigma_1 + 2\sigma_2)v f^{\text{MB}}(v) dv \quad (2.37)$$

The coefficient 2 in the term  $2\sigma_2$  expresses the fact that in a double spin flip, two dipolar relaxations take place.  $\beta$  is dependent on the density  $n(\vec{r})$  of the atomic cloud. The absolute dipolar relaxation rate is

$$\Gamma = n(\vec{r})\beta. \quad (2.38)$$

**Consequences** The phenomena arising with dipolar relaxations can limit experiments or lead to novel possibilities.

A strong limitation of purely magnetic atom traps are due to dipolar relaxations. A time invariant magnetic field cannot yield a local maximum of the modulus of the magnetic field  $B^*$ . Thus, only atoms in low field seeking states, i.e. states with a positive magnetic quantum number  $m_S > 0$  can be confined in all directions (in a magnetic field minimum). Atoms in low field seeking states can convert the potential energy into kinetic energy during an inelastic dipolar collision. The kinetic energy gain increases the temperature of the atomic cloud and can hence inhibit a cooling process.

On the contrary, dipolar relaxations can lead to the transfer of kinetic to potential energy. This phenomenon is subject to Section 2.2.2.

### 2.2.2 Demagnetization Cooling

We prepare an atomic cloud at temperature  $T$  in the lowest ZEEMAN state  $m_S = -S$  ( $m_S = -3$  for the  ${}^7S_3$  ground state of  ${}^{52}\text{Cr}$ ) in a magnetic field  $\vec{B}$  with  $|\vec{B}| = B$ . According to Section 2.2.1, there is a finite chance for inelastic collisions that change the ZEEMAN state  $m_S \rightarrow m_S \pm 1$ . If the state  $m_S - 1$  does not exist which coincides with our consideration, the magnetic quantum number can only increase:  $m_S \rightarrow m_S + 1$ . The difference of potential energy is positive and reads

$$\Delta E = E(m_S = -S + 1) - E(m_S = -S) = g_S \mu_B B. \quad (2.39)$$

Energy conservation demands that the kinetic energy the colliding particles is reduced by  $\Delta E$  ( $2\Delta E$ ) if a single (double) spin flip occurs. Classically, this is only possible if the kinetic energy of the particles before the collision is  $E_{\text{kin}} > \Delta E$  ( $E_{\text{kin}} > 2\Delta E$ ). The probability for this condition is provided by the thermal velocity distribution in Equation (2.36). Figure 2.4 b) shows which part of the MAXWELL-BOLTZMANN distribution can theoretically perform inelastic dipolar collisions regardless of finite cross sections. Even if at finite cross sections only a fraction of atoms fulfilling the energy requirement change their magnetic quantum number, the temperature decreases after rethermalization since kinetic energy is stored in potential energy – see Figure 2.4 c). With an optical pumping process in a lambda energy level configuration, the fraction of atoms in the  $m_S = -S + 1$  state can be re-transferred to the  $m_S = -S$  state provided the  $m_S = -S$  state is a dark state for the employed light with  $\sigma^-$  polarization. The energy  $\Delta E$  is diverted by a photon during the spontaneous decay from the excited state.

The cooling rate of demagnetization cooling has been studied theoretically [19]. It has been shown that, apart from other parameters like the density, the cooling rate depends on the ratio

$$\eta_b = \frac{g_S \mu_B B}{k_B T} = \frac{\Delta E}{k_B T} \quad (2.40)$$

which is called *cutoff parameter* because it sets the minimum kinetic energy for collisions above which dipolar relaxations are possible. On the one hand, a negligible fraction of atoms can perform inelastic collisions at high values of  $\eta_b \gg 1$  because the probability of a collision with a kinetic energy of  $\eta_b k_B T$  is small for  $\eta \gg 1$ . Also, the low probability of such kinetic energies imply a long time for rethermalization. On the other hand, a large kinetic energy can be dissipated within a single cooling cycle.

The temperature slope can be estimated [19]:

$$\dot{T} \approx -\frac{2}{3/2 + \alpha} \sqrt{\frac{k_B}{\pi m}} \frac{(\mu_0(2\mu_B)^2 m)^2}{30\pi \hbar^4} S^2 [(1 + \eta_b)S + (2 + 4\eta_b)e^{-\eta_b}] \eta_b e^{-\eta_b} n T^{3/2}. \quad (2.41)$$

The value  $\alpha = \sum_j \frac{1}{n_j}$  is given by the the best approximated low power law trap

$$U(x, y, z) = c_x x^{n_1} + c_y y^{n_2} + c_z z^{n_3}. \quad (2.42)$$

---

\*A local maximum requires a critical position  $\vec{r}_0$  where  $\vec{\nabla} B|_{\vec{r}=\vec{r}_0} = \vec{0}$  **and**  $\exists \epsilon \forall \vec{r} [|\vec{r} - \vec{r}_0| < \epsilon \Rightarrow B(\vec{r}) < B(\vec{r}_0)]$ .

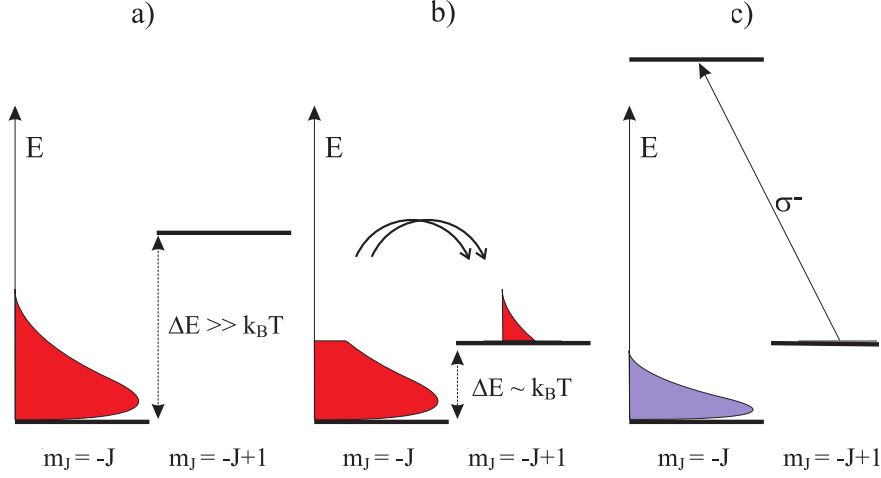


Figure 2.4: The scheme of demagnetization cooling. a) At high ZEEMAN splittings, the probability for an inelastic dipolar collision is low. b) If the ZEEMAN splitting is on the order of the thermal energy, colliding atoms can transfer kinetic energy in the potential energy of the neighbored ZEEMAN state. c) After the process b), the atomic cloud rethermalizes yielding a lower temperature. Atoms in the  $m_J = -J + 1$  state can be pumped back to the ground state  $m_J = -J$  with  $\sigma^-$  polarized light. Source: [9].

The influence of the trap geometry on the cooling process and the time evolution will be studied by means of the simulation of our setup in Chapter 7. The most efficient value of  $\eta_b$  has been calculated to be approximately 1.31 [19].

## 2.3 The Interaction between Light and Matter

**Introduction** Even though the light-matter interaction is to be treated with quantum electrodynamics, it is astonishing how many phenomena that take place on the length scale of an atom can still be described with a high precision in (the more intuitive) classical theories. One of these phenomena is the dipole force, a force on atoms that are exposed to and polarized by a light field with a frequency far off-resonant to atomic transitions. The described situation also includes a second force, the *scattering force*, which arises from absorption and reemission of photons. At high absorption rates, the classical model fails since it does not account for saturation. This mechanism can be studied in a *semiclassical* approach with a classical radiation field and a quantum mechanical atom [5]. It is the basic mechanism for laser cooling. Since this work concentrates on dipole traps which operate on the basis of the dipole force, we shall not penetrate the theory of laser cooling.

**The Dipole Force** In this classical approach, which is also called *Lorentz model*, we take an atom with complex polarizability  $\alpha(\omega)$  [17] [5] and expose it to the electric field

$$\vec{E}(\vec{r}, t) = \vec{e}\tilde{E}(\vec{r})e^{-i\omega t} + c.c. \quad (2.43)$$

of polarization  $\vec{e}$ , amplitude  $\tilde{E}(\vec{r})$  and frequency  $\omega$ . The electric field induces a dipole moment

$$\vec{p}(\vec{r}, t) = \alpha\vec{E}(\vec{r}, t) \quad (2.44)$$

that oscillates with the electric field and has an amplitude

$$\tilde{p} = \alpha\tilde{E}. \quad (2.45)$$

The intensity of the light is

$$I = 2\epsilon_0 c |\tilde{E}|^2. \quad (2.46)$$

The dipole moment has an energy in the oscillating field given by [17]

$$U = -\frac{1}{2} \langle \vec{p} \cdot \vec{E} \rangle_{\text{time}} = -\frac{1}{2\epsilon_0 c} \Re(\alpha) I. \quad (2.47)$$

The dependence of the intensity  $I = I(\vec{r})$  on the position is the reason for the **dipole force**, also referred to as *gradient force*.

$$\vec{F}(\vec{r}) = -\nabla U(\vec{r}) = \frac{1}{2\epsilon_0 c} \Re(\alpha) \nabla I(\vec{r}). \quad (2.48)$$

In homogeneous fields, the force is zero.

$$\nabla I = 0 \quad \Rightarrow \quad \vec{F} = 0. \quad (2.49)$$

Equations (2.47) and (2.48) form the basis for optical dipole traps.

The imaginary part of the polarizability accounts for absorption of energy from the driving field. It contributes to the out-of-phase component of the electronic oscillation. The absorbed power is [17]

$$P = \langle \dot{\vec{p}} \cdot \vec{E} \rangle_{\text{time}} = \frac{\omega}{\epsilon_0 c} \Im(\alpha) I. \quad (2.50)$$

This power is absorbed in terms of photons with energy  $\hbar\omega$ . The photons are re-emitted spontaneously. We can thus give a formula for the scattering rate

$$\Gamma_{\text{sc}}(\vec{r}) = \frac{P}{\hbar\omega} = \frac{1}{\hbar\epsilon_0 c} \Im(\alpha) I(\vec{r}). \quad (2.51)$$

The scattering of photons heats the cloud and can limit the desired performance of optical dipole traps. Contrarily, using the DOPPLER frequency shift, it can be taken use of for laser cooling as mentioned in the introduction of this section.

We reconsider the dipole force. The linearity of the intensity in Equation (2.47) to the trap potential motivates the study of the intensity profile of the laser beam that leads to an optical dipole trap. Laser beams in the TEM<sub>00</sub> mode are called *Gaussian beams*.

**The Gaussian Beam.** The intensity of a Gaussian beam at the cylindric coordinates  $(r, z)$  is given by

$$I(r, z) = I_0 \frac{1}{1 + \frac{z}{z_R}} \exp \left[ \frac{-2r^2}{w_0^2 \left( 1 + \left( \frac{z}{z_R} \right)^2 \right)} \right]. \quad (2.52)$$

$w_0$  is the beam waist at  $z = 0$ , it is where the intensity drops to  $I(r = w_0, z = 0) = I_0 e^{-2}$ .  $z_R$  is the RAYLEIGH range. It is given by  $w_0$  and the wavelength  $\lambda$  via

$$z_R = \frac{\pi w_0^2}{\lambda}. \quad (2.53)$$

The beam waist at the position  $z$  on the beam axis is given by

$$w_i = w_{0i} \sqrt{1 + \left( \frac{z - z_{\text{focus},i}}{z_{0i}} \right)^2}. \quad (2.54)$$

We use

$$z_{0i} = \frac{\pi w_{0i}^2}{\lambda} \Rightarrow w_{0i} = \sqrt{\frac{\lambda z_{0i}}{\pi}} \quad (2.55)$$

to express the beam waist at position  $z$  in terms of the RAYLEIGH range

$$w_i = \sqrt{\frac{\lambda z_{0i}}{\pi} \left( 1 + \left( \frac{z - z_{\text{focus},i}}{z_{0i}} \right)^2 \right)} \quad (2.56)$$

or in terms of the focal beam waist

$$w_i = w_{0i} \sqrt{1 + \left( \frac{\lambda(z - z_{\text{focus},i})}{\pi w_{0i}^2} \right)^2}. \quad (2.57)$$

---

The intensity of a Gaussian beam hence creates a potential for atoms c.f. Equation (2.47)

$$U(r, z) = \frac{-U_0}{1 + (z/z_R)^2} \exp\left(\frac{-2(r/w_0)^2}{1 + (z/z_R)^2}\right). \quad (2.58)$$

This potential will be analyzed in Section 4.1. The proportionality factor  $a$  for  $U_0 = a * I_0$  is dependent on the polarizability of the species exposed to the laser light and on the laser wavelength.

# Chapter 3

## Setup

For the understanding of this work, it is not crucial how we prepare a cold atomic beam. This has already been described in [15] [13] [1]. It is sufficient to start from an atomic beam prepared in the  ${}^7\text{S}_3$ ,  $m_S = +3$  state and guided radially by a quadrupole magnetic field which is created by a current through copper bars in IOFFE configuration. The beam has a radial temperature smaller than  $65 \mu\text{K}$  and the longitudinal temperature in the moving frame is below  $400 \mu\text{K}$  [8]. The mechanism which we use for loading the atoms into a conservative potential is discussed in Section 3.1. Detailed treatments can be found in [7] and [32].

### 3.1 Loading a Hybrid Trap from a Beam

In order to load an incident flux of atoms into an energy conservative trap, it is necessary to remove the directed kinetic energy with a dissipative process. As shown in Figure 3.1 (a), we create a magnetic potential barrier in direction of the beam  $\vec{e}_x$  for atoms in the  $m_S = +3$  state at which atoms lose their directed kinetic energy. At the position of the potential maximum which is chosen equal to the directed kinetic energy, an optical pumping process transfers the atoms into the  $m_S = -3$  state as shown in Figure 3.1(b). We use the  ${}^7\text{S}_3 \rightarrow {}^7\text{P}_3$  transition at  $427.2 \text{ nm}$ . The magnetic potential for atoms in the  $m_S = -3$  state is attractive, hence, a trap

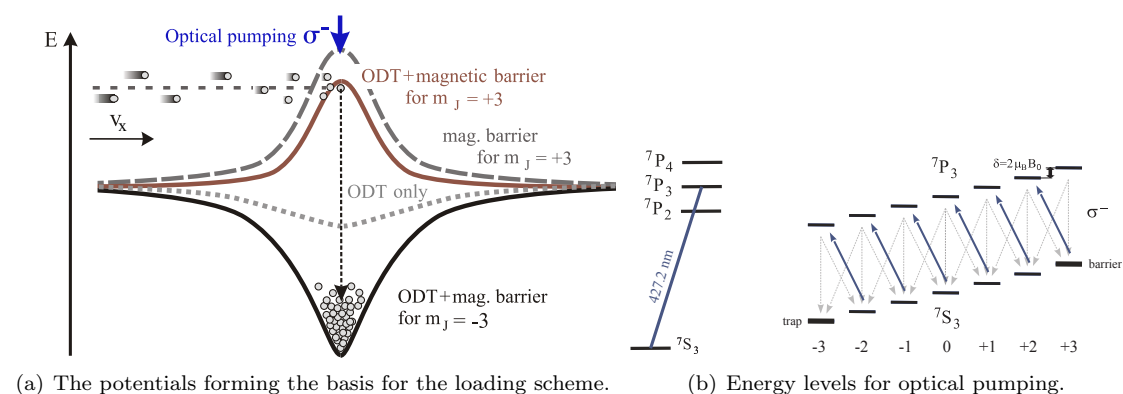
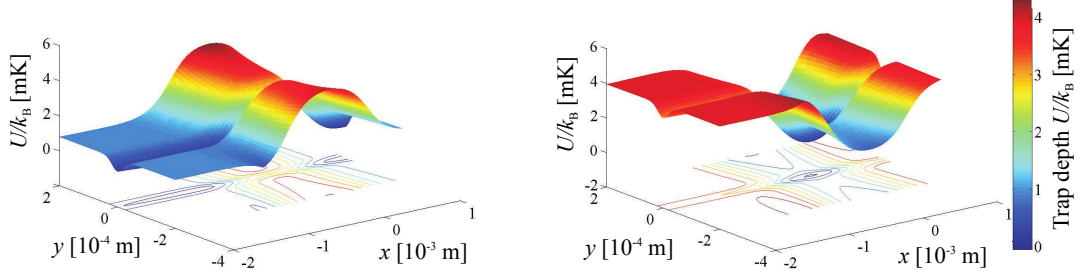


Figure 3.1: The loading scheme. (a) The guided atoms are in the  $m_S = +3$  state. Magnetic coils produce a repulsive potential. Incoming atoms lose their directed kinetic energy. On top of the potential hill, the atoms are exposed to a  $\sigma^-$  polarized laser beam that implements optical pumping (b) to the ground state  $m_S = -3$ . The magnetic potential for that state is attractive. This leads to an accumulation of atoms in the area of the potential minimum. Figures 3.1(a) and 3.1(b) modified from [8].

is realized in this direction. Since the potential landscape of the barrier is also repulsive in the  $\vec{e}_y$  direction (perpendicular to the atomic beam), we use an optical dipole trap (ODT) laser at a power of 90 W\* and a beam waist of 30  $\mu\text{m}$  to funnel the atomic beam to the maximum of the magnetic potential as shown in Figure 3.3. The potential landscape in the  $z = 0$  plane is shown



(a) Potential landscape for atoms in the  $m_S = +3$  state. (b) Potential landscape for atoms in the  $m_S = -3$  state.

Figure 3.2: The potential landscapes before (a) and after (b) the optical pumping process. The *hybrid trap* is the combination of the ODT laser along  $y = z = 0$  and a magnetic potential which changes its sign from (a) to (b). Figures modified from [7].

in Figure 3.2(a). For the realization of confinement in all directions after the loading process, the ODT is essential since the magnetic field is only attractive in two directions ( $\vec{e}_x$  and  $\vec{e}_z$ ) and repulsive in the third direction ( $e_y$ ). The radial confinement of the atomic beam by the ODT requires an axial overlap of the atomic beam with the ODT laser. We have realized this by adding a magnetic field that shifts the location of the potential minimum such that the atomic beam is guided onto the ODT axis, c.f. Figure 3.3.

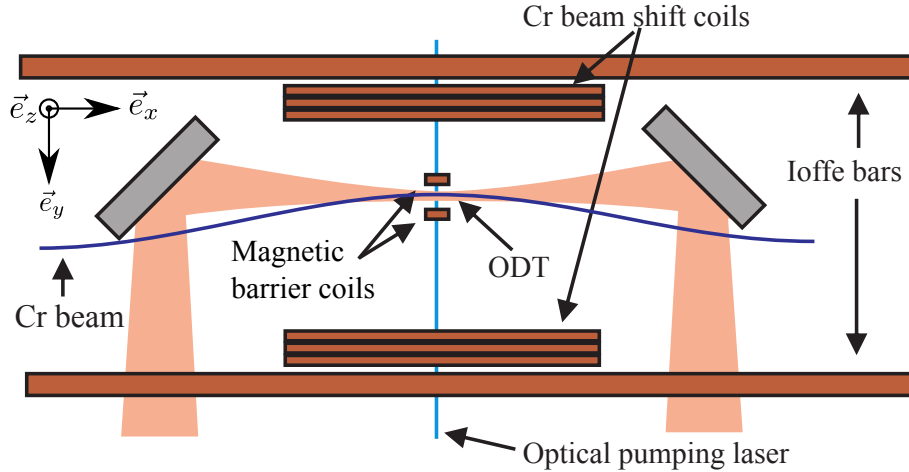


Figure 3.3: Schematic drawing of that part of the setup which provides the trapping mechanism for atoms from the atomic beam. The chromium beam is guided in the magnetic potential minimum created by the IOFFE bars and the “Cr beam shift coils”. That way, it can axially be overlapped with the ODT beam which funnels the atomic beam through the center of the barrier coils. Figure modified from [7].

The ODT laser provides a strong confinement in the  $x = 0$  plane. The confinement in  $\vec{e}_x$

\*Company: IPG, Model: YLR 300 W

direction is dominated by the magnetic potential and it is smaller than the confinement in  $\vec{e}_y$  and  $\vec{e}_z$ , resulting in a cigar shaped trap along the  $\vec{e}_x$  direction.

## 3.2 Mechanical Setup

As a basis for the development of the mechanical setup on which the optics are to be placed, these facts have to be accounted for:

1. Little space and limited optical access. The dimple laser has to be inserted in the plane orthogonal to the atomic beam. The imaging system with two probe laser beams, the optical pumping laser and the ODT are all aligned in that plane. It is necessary to plan at least space for
  - the laser outcoupler,
  - an acousto-optic modulator (AOM),
  - one telescope lens system before and one after the AOM, the ladder one should be on linear translation stages,
  - one mirror before the AOM,
  - two mirrors close to the chamber for tuning the position and the direction of the laser beam,
  - a beam dump and a mirror that reflects only the beams that have to be dumped.
2. If the setup is extended with optical tables, they have to be mounted with highest stability in order not to excite and thus heat the atomic cloud. Vibrations on the setup in the audio frequency will modulate the direction of the laser beam. If the vibration frequencies coincide with trap frequencies, heating effects will reduce the life time and the phase space density of the atomic cloud.

A setup has been designed and built according to Figure 3.4. Aluminum has been chosen as the construction material because it is paramagnetic with a magnetic susceptibility of  $\chi \approx 2.2 \times 10^{-5}$ . This reduces the influence on magnetic fields in contrast to ferromagnetic materials. For the same reason, construction materials with a low magnetic susceptibility have been chosen for the optical mounts. Moreover, due to the low hardness of aluminum compared to stainless steel, e.g., the setup can be modified more easily.

The aluminum board in the  $x = 0$  plane was mainly planned to reduce vibrations of the board in the  $y = 0$  plane on which the optical elements are mounted.

## 3.3 Imaging

Due to the mechanical setup for the dimple laser system, we needed to modify the imaging setup. The new setup is shown in Figure 3.5. I will mention the changes in the setup after describing the imaging system itself.

**Absorption Imaging.** The atomic transition  ${}^7S_3 \rightarrow {}^7P_4$  at 425.6 nm is used for absorption imaging. The large natural line width of  $2\pi \times 5$  MHz and the saturation intensity of  $8.5 \text{ mW} \cdot \text{cm}^2$  [1] feature a high absorption rate and thus a good contrast. The laser setup for the blue light at 425.6 nm is described in [4] [6] [7] [32]. We prepare the laser light in  $\sigma^-$  polarization using a polarizing cube and a  $\lambda/4$  retardation plate in combination with the magnetic field in  $\vec{e}_z$  direction created by a pair of coils shown in Figure 3.5. Since the laser light is absorbed by the atomic cloud, the resultant shadow cast can be projected onto a CCD camera. We use an electron

---

\*Source: <http://info.ee.surrey.ac.uk/Workshop/advice/coils/mu/>

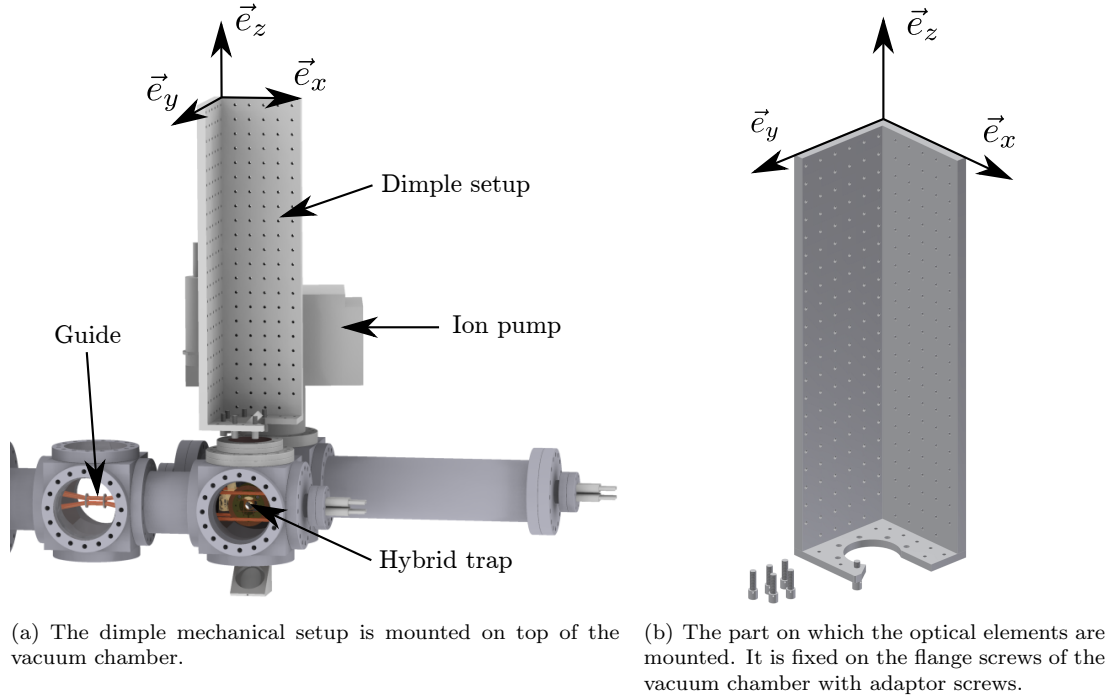


Figure 3.4: Drawing the mechanical setup. The parts in (b) have been designed using *Autodesk Inventor*. It has been built by the mechanical workshop, *Mechanische Werkstatt* of the Universität Stuttgart.

multiplying CCD camera\*. The aspheric lens ASPH with a focal length of  $f = 15 \text{ mm}$ <sup>†</sup> provides a high numerical aperture and creates an intermediate picture at a distance of about 8 cm which itself is mapped onto the camera with an aspheric lens of  $f = 100 \text{ mm}$  focal length. A notch filter removes stray light, especially infrared light from the ODT and from the dimple.

**Modifications** We needed to exchange a mirror with the dichroic mirror  $\text{DCM}_1$  in order to insert the dimple laser on the imaging axis. By moving the CCD camera, we could place the  $f = 100 \text{ mm}$  aspheric lens from the area between the vacuum chamber and  $\text{DCM}_1$  to a position right of  $\text{DCM}_1$ . That way, the dimple laser does not pass through the aspheric lens and the imaging system can be adjusted without effecting the dimple setup. For the same reason, a similar configuration, we changed the position of the quarter wave plate.

To determine the magnification of the modified imaging setup, we compare absorption pictures from before and after the modifications. Figure 3.6 shows an absorption picture after the modifications. We see two characteristic features in the picture that originate in irregularities of the barrier coils' glue. Since this feature is identified in all pictures, we can compare the pixel distance. We calculate a ratio of  $\frac{d_{\text{new}}}{d_{\text{former}}} = 0.8185$  of the pixel distances in the modified and the former setup. Based on the former magnification  $M_{\text{former}} = 5.58$ , we calculate the new magnification

$$M = 0.8185 * 5.58 = 4.57. \quad (3.1)$$

\*Company: *Andor*, Model: iXon DV885JCS-VP

<sup>†</sup>and a working distance of  $f^{\text{wd}} = 11 \text{ mm}$ , see Figure 3.8

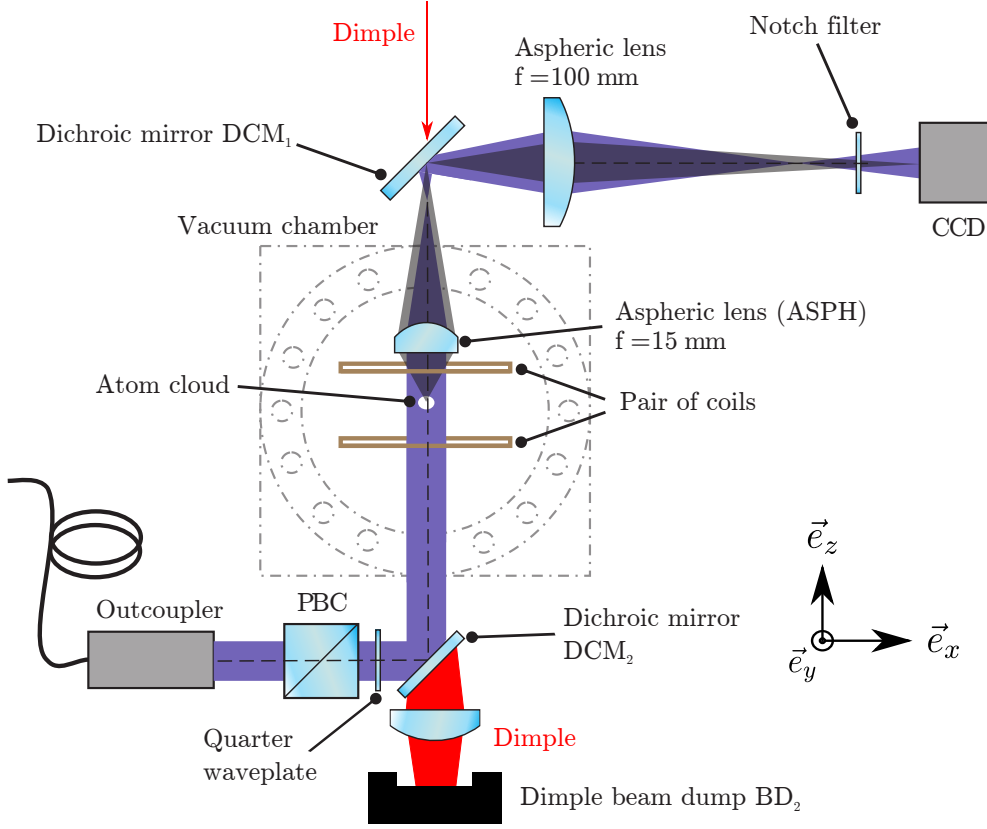


Figure 3.5: Imaging setup. The outcoupler and polarizing beam cube (PBC) have been rotated into the  $x$ - $z$  plane for clarity. In the experiment, they point towards  $\vec{e}_y$ . For absorption imaging, we create  $\sigma^-$  polarized light with a polarizing beam cube and a  $\lambda/4$  retardation plate. The shadow of the laser light is projected onto the CCD camera using two aspheric lenses. Parts of the dimple laser setup are foretold for Section 3.4. Figure modified from [7].

**Image Processing.** BEER's law relates the absorption of the laser light with the density of the atomic cloud. The integrated density along  $\vec{e}_z$ , called *column density* is [7]

$$\rho(x, y) = \frac{1}{\sigma_{sc}} \ln \left( \frac{I_0(x, y)}{I(x, y)} \right) \quad (3.2)$$

with the scattering cross section  $\sigma_{sc} = 8.65 * 10^{-10} \text{ cm}^2$  for the  $^{52}\text{Cr}$  transition  $7S_3 \rightarrow 7P_4$  and  $\frac{I(x, y)}{I_0(x, y)}$  is the ratio\* of intensity absorbed by the atomic cloud. The expression  $\ln \left( \frac{I_0(x, y)}{I(x, y)} \right)$  in Equation 3.2 is called absorbance or OPTICAL DENSITY (OD). A high optical density indicates a large number of atoms in the imaging direction. Figure 3.7 shows an example of the optical density from an absorption picture of an atomic cloud.

From the column density

$$\rho = \int_{-\infty}^{+\infty} n(x, y, z) dz. \quad (3.3)$$

we deduce a relation to the density. The density distribution in atomic clouds can often be described with Gaussian functions, more precisely as the product of the atom number  $N$  and the

\*Please note the inversion of the fraction.

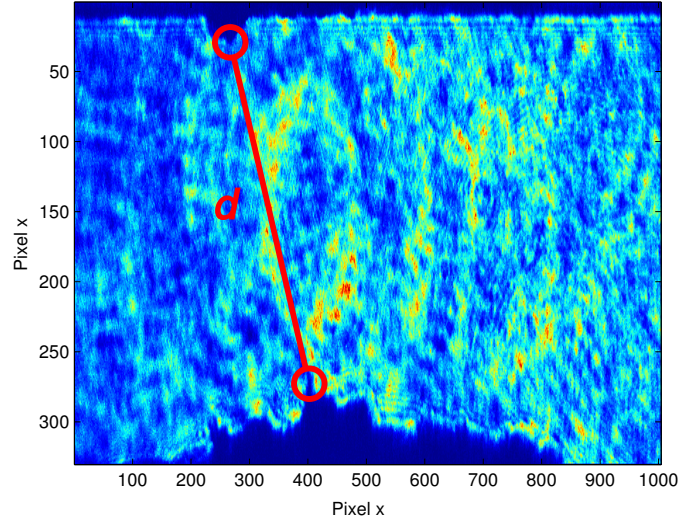


Figure 3.6: The magnification can be compared to the former setup with the pink drawn pixel distance  $d$  of two distinct features on top and on the bottom in the absorption picture. These features arise from the glue of the barrier coils.

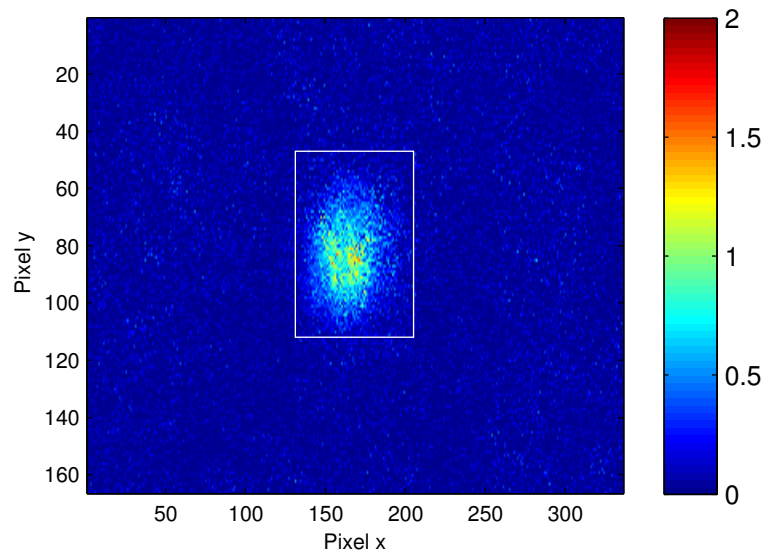


Figure 3.7: Example of the optical density from absorption imaging of an atomic cloud.

normed Gaussian functions

$$n(x, y, z) = N * n_x(x) * n_y(y) * n_z(z). \quad (3.4)$$

The column density can be written

$$\rho = \int_{-\infty}^{+\infty} N * n_x(x) * n_y(y) * n_z(z) dz = N * n_x(x) * n_y(y) * \int_{-\infty}^{+\infty} n_z(z) dz \quad (3.5)$$

$$\stackrel{\text{norm.}}{=} N * n_x(x) * n_y(y) \stackrel{(3.4)}{=} \frac{1}{n_z(z)} n(x, y, z).$$

This means that in every plane  $z = z_0$ , especially  $z = 0$ , the column density is a multiple of the density. For  $z = 0$ ,

$$\rho = n(x, y, 0) * \sigma_z \sqrt{2\pi}. \quad (3.6)$$

With the knowledge of the cloud width  $\sigma_z$  along  $\vec{e}_z$ , we get the density profile in the  $z = 0$  plane from the column density. Without the dimple, we have radial symmetry around the  $x$  axis:  $\sigma_z = \sigma_y$ . In this case, the three dimensional density distribution is measured with one absorption picture.

### 3.4 Optics

We use an Yb-fiber laser\* with a wavelength of 1064 nm and a maximum power of 20 W. This laser has a small coherence length of 0.7 mm [14]. We place the optical setup on an aluminum board described in Section 3.2. The schematic arrangement is shown in Figure 3.8. The beam waist of the laser after the fiber was measured with the *razor blade method*<sup>†</sup> to be 2.57 mm. We deploy an acousto-optical modulator (AOM)<sup>‡</sup> to control the laser power within an experiment for parametric heating experiments discussed in Section 4 and for a rapid switch-off studying expansion dynamics of atomic clouds, e.g. in Section 5.2.

To couple the laser beam in the AOM, we prepare a beam waist of 425  $\mu\text{m}$  using a lens system in a telescope configuration with a waist reduction of factor 6. We measure that the AOM has a cylindrical-lens-behavior for broader beams. This behavior can be due to inhomogeneous RF power in the crystal.

**Two-Frequency Operation.** We operate the AOM at two radio frequencies concurrently c.f. [10] using the first order diffracted at the 123 MHz sonic waves for experiments and dumping all other orders in the beam dump  $\text{BD}_1$ . We add sonic waves at a different frequency, 98 MHz. In this way, we can keep the power dissipated by the AOM constant and reduce effects like the deviation of the beam pointing direction, which can be up to 1 mrad [10]. The AOM is operated at 2.3 W. This value is set by the maximum power that can still be absorbed at either frequency. If the control voltage of the 98 MHz AOM driver is 0 V, 2.3 W are reached at a control voltage of  $U_{\text{Dimple}} = 7.95$  V at the 123 MHz. We employ electronics that regulate the applied voltage at the AOM driver at the compensation frequency depending on  $U_{\text{Dimple}}$ . This dependency is programmed with a lookup table of input values  $U_{\text{Dimple}}$  and output values  $U_{\text{out}}(U_{\text{Dimple}})$ . Figure 3.9 shows how the frequencies are mixed schematically. For the measurements of trap frequencies described in Section 4, a second control voltage,  $U_{\text{modulation}}$  is added to  $U_{\text{Dimple}}$ . This voltage is sinusoidal with a frequency of more than 1 kHz and with a small amplitude of less than 1 V. On that small time scale, thermal effects can be neglected at such amplitudes.

**Astigmatism.** Due to limited optical access, we need to shine the dimple laser in the vacuum chamber on axis with the imaging light. This is possible with dichroic mirrors shown in Figures 3.8 and 3.5. The dichroic mirrors are highly transmissive for the dimple laser wavelength and highly reflective for the imaging light at 425 nm. Since the dimple laser has to be convergent at

\*IPG PYL-20M-LP

<sup>†</sup>described in [http://qwiki.stanford.edu/index.php/How\\_To\\_Measure\\_A\\_Beam\\_Waist](http://qwiki.stanford.edu/index.php/How_To_Measure_A_Beam_Waist), 13 Dec 2011

<sup>‡</sup>Crystal Technology Inc., Model: 3110-199, S/N: 09410, 2 W maximum radio frequency (RF) input power

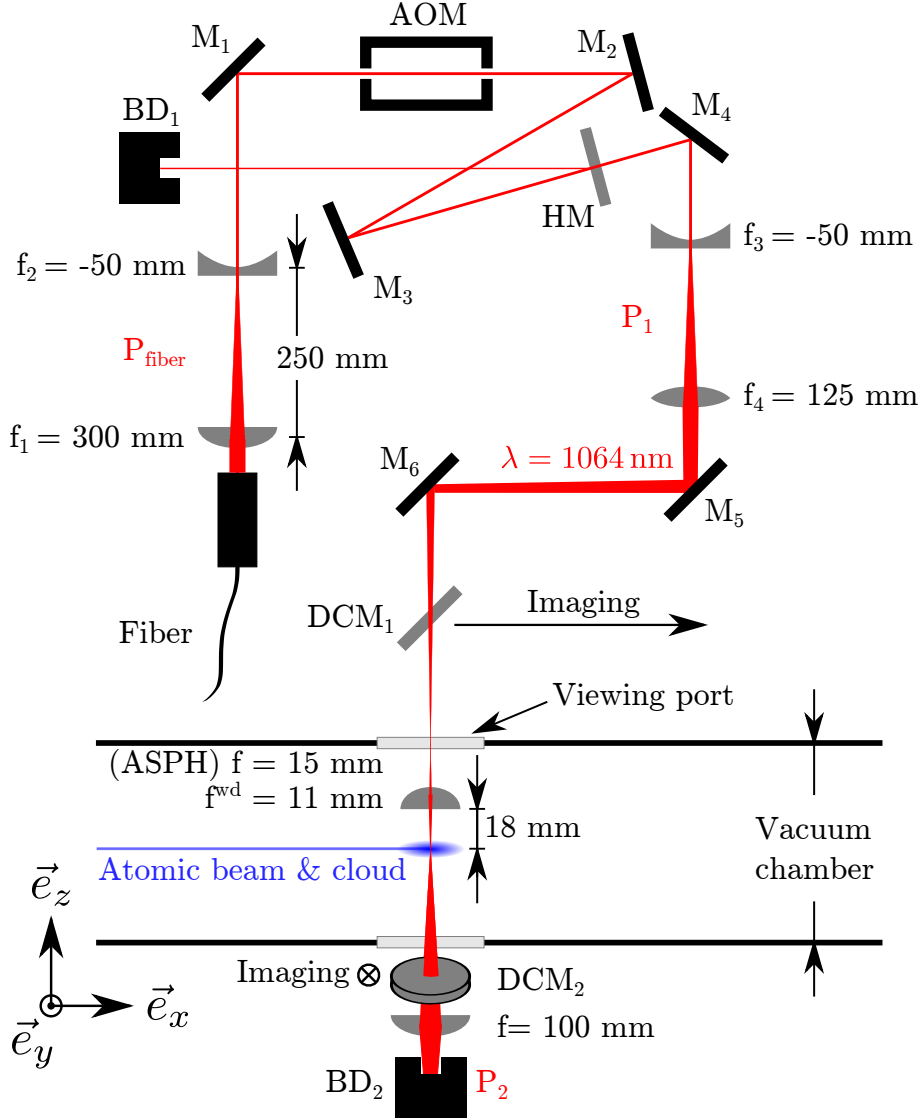


Figure 3.8: The optical setup of the dimple laser system.  $f$ ,  $f_1$ - $f_4$ : focal lengths of respective lenses.  $M_1$ - $M_6$ : mirrors. HM: one half of a mirror which reflects all unwanted diffraction orders to the beam dump.  $DCM_{1,2}$ : dichroic mirrors with a high reflectivity for 425 nm light and a high transmissivity for infrared light, used to enable imaging on the dimple laser axis.  $BD_{1,2}$ : beam dumps. The laser beam is accessible for a measurement of the laser powers  $P_{1,2, \text{fiber}}$  at the respective positions. AOM: acousto-optic modulator. The diffraction from the AOM is in  $\vec{e}_y$  direction and thus the diffraction orders are projected onto each other from this point of view.

the dichroic mirror  $DCM_1$ , the beam waist of one direction is effectively reduced by anisotropic refraction. This leads to an astigmatism. The refraction at the surfaces of  $DCM_1$  is shown with a simulation in Figure 3.10. The astigmatism causes a reduction of the maximum beam intensity. However, this reduction can be compensated by a reduction of the beam waist. The astigmatism is also subject to the results of Section 4.2.5.

**How to Set the Focus.** Figure 3.8 shows that the focal length of ASPH does not coincide with the distance between ASPH and the atomic cloud. If it did, a collimated beam would have

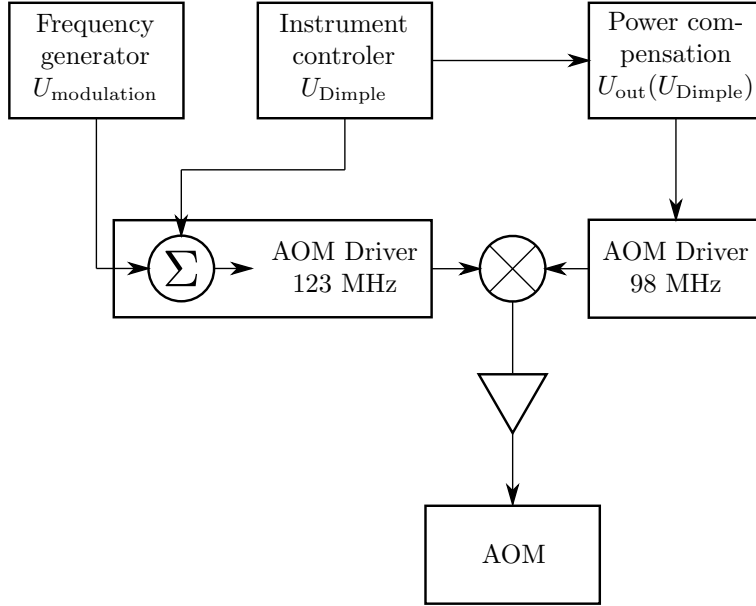


Figure 3.9: Schematic AOM mode of operation.  $\otimes$  and  $\nabla$  symbolize a frequency mixer and an RF amplifier respectively.  $\Sigma$  symbolizes a voltage summer. We control two voltages:  $U_{\text{Dimple}}$  and  $U_{\text{modulation}}$ , with  $U_{\text{modulation}} \neq 0$  only if we want to modulate the laser intensity.  $U_{\text{Dimple}} + U_{\text{modulation}}$  controls the RF power at 123 MHz whereas the voltage  $U_{\text{out}}$  controls the RF power at 98 MHz. An electronic circuit regulates the voltage  $U_{\text{out}}$  in dependence on  $U_{\text{Dimple}}$  such that the power dissipated by the AOM stays constant at all times. We use the first diffraction order of the laser at the 123 MHz sonic waves and dump all other diffraction orders.

its focus at the position of the atoms and one could set the beam waist of the focus by the radius of the collimated beam. The deviation from this ideal case complicates the path of rays necessary for the right focus position. We have simulated feasible positions and focal lengths of the lenses  $f_3$  and  $f_4$  with *ZEMAX\**. We have included  $\text{DCM}_1$ , the viewing port and ASPH in the calculations and have taken account for limited space between  $M_4$  and  $M_5$ . For standard focal lengths of  $f_3 = -50$  mm and  $f_4 = 125$  mm, we have simulated 276.5 mm for the optical path length between  $f_4$  and the atomic beam and a spacing of 288.2 mm between  $f_3$  and  $f_4$ . We have confirmed the calculation within measurements in a test setup. Further, the calculations show that it is a good approximation to fine-tune the  $z$  component of the focal position with the  $z$  component of the lens position of  $f_4$ . The  $z$  component of the lens position of  $f_3$  alters the beam waist, however, it changes the position of the focus at the same time. The focus shift can be reverted by tuning the position of  $f_4$ .

We conduct measurements in a test setup, since the final setup does not allow such measurements due to limited accessibility. Since tolerances and uncertainties, e.g. in terms of the position of the aspheric lens in the vacuum chamber, play a considerable role in the real setup, it is important to know the quantitative effect of tuning the lens positions of  $f_3$  and  $f_4$  and the beam direction via  $M_5$  and  $M_6$ . The effects of the optical elements are summarized in Table 3.4.

### 3.5 Power Characteristics

For an estimation of the laser power at the position of the atoms, we measure the laser powers at positions as close as possible above ( $P_1$ ) and below ( $P_2$ ) the vacuum chamber. The available

\*Software for optical system design by the company *Radiant ZEMAX LLC*

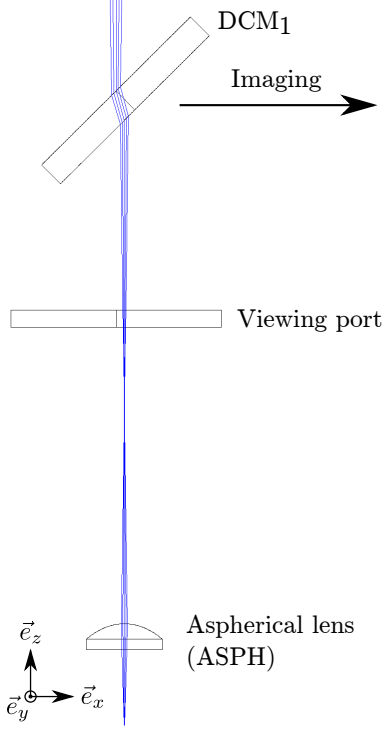


Figure 3.10: The dimple laser beam is shone in  $-\vec{e}_z$  direction through the dichroic mirror  $\text{DCM}_1$  which is needed for the imaging light. The convergence of the dimple laser beam leads to an astigmatism. The reason for the astigmatism is the radial symmetry break: The left rays are less refracted than the right rays, whereas in the direction  $\vec{e}_y$ , all rays are refracted equally.

measurement positions are between the lenses  $f_3$  and  $f_4$  of the last telescope and at the position of the beam dump under the vacuum chamber. The measured laser powers are  $P_1 = 410 \text{ mW}$  and  $P_2 = 250 \text{ mW}$  respectively. Thus, the ratio of the power in the beam dump amounts to

$$T_1 = P_2/P_1 = 0.6098 = 60.98 \% \quad (3.7)$$

which is the transmission factor of the optical parts considered here.

The transmission ratio  $T_{\text{dichroic}}$  of the dichroic mirrors has been measured to be between 93 and 94 % and the transmission  $T_{\text{aspheric}}$  of the aspheric lens in the vacuum chamber is 84 %. The transmission of the view ports of the vacuum chamber is  $T_{\text{air} \leftrightarrow \text{glass}} = 96 \%$  per contact plane (air  $\leftrightarrow$  glass). Adding up these transmissions, the overall transmission

$$T_2 = T_{\text{air} \leftrightarrow \text{glass}}^4 * T_{\text{aspheric}} * T_{\text{dichroic}}^2 = 0.96^4 * 0.84 * 0.935^2 = 0.6237 = 62.37 \% \quad (3.8)$$

Degree of freedom	Step size	New focus position
$M_5 : \vec{e}_y$ vertical	1 turn cw	$280 \mu\text{m} \vec{e}_y$
$M_5 : \vec{e}_x$ horizontal	1 turn cw	$-350 \mu\text{m} \vec{e}_x$
$M_6 : \vec{e}_y$ vertical	1 turn cw	$500 \mu\text{m} \vec{e}_y$
$M_6 : \vec{e}_x$ horizontal axis	1 turn cw	$650 \mu\text{m} \vec{e}_x$
$f_4 : -\vec{e}_z$ towards $M_5$	$5 \text{ mm} \hat{=} 10 \text{ turns}$	$-550 \mu\text{m} \vec{e}_z$
$f_3 : -\vec{e}_z$ towards $M_5$	move 10 mm	$-600 \mu\text{m} \vec{e}_z$

Table 3.1: The dependence of the angles of  $M_5$  and  $M_6$  and of the lens positions of  $f_3$  and  $f_4$  on the focal position. Degree of freedom (first column) which is deviated by the value of the second column leads to a change of the focal position according to column three. *cw* means *clockwise* here. See Figure 3.8 for the orientation of the axes.

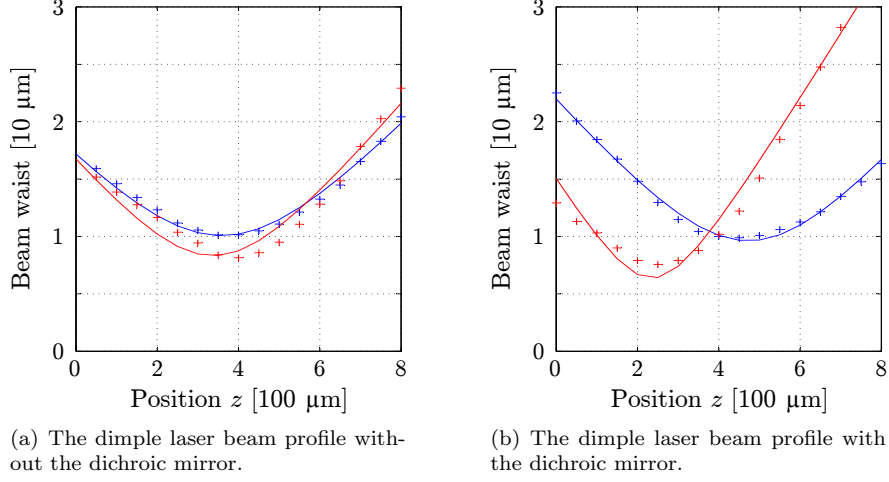


Figure 3.11: Astigmatism due to the dichroic mirror DCM<sub>1</sub>. The figures show the beam radius in  $\vec{e}_x$  (blue) and  $\vec{e}_y$  (red) directions in terms of the position  $z$  along the beam. Solid lines denote the fit of the data using Equation (2.57). The foci are at the same position in Figure 3.11(a). We measure an astigmatism shown in Figure 3.11(b) if the dichroic mirror is inserted in the setup under an angle of  $45^\circ$  according to Figure 3.8. The relative shift of the foci in  $\vec{e}_z$  direction leads to a reduction of the maximum laser intensity. However, regardless the astigmatism, the beam radius in the test setup is  $10\ \mu\text{m}$  in both directions – see Figure 3.11(b) at  $z = 400\ \mu\text{m}$ . This results in the desired intensity.

is in very good agreement with Equation (3.7):

$$T_{\text{error}} = T_2 - T_1 = -0.0140 = -1.4\%. \quad (3.9)$$

This allows a calculation of the laser power at the position of the atoms. The value

$$\begin{aligned} T &= T_{\text{air} \leftrightarrow \text{glass}}^2 * T_{\text{aspheric}} * T_{\text{dichroic}}^1 \pm T_{\text{error}} \\ T &= 0.96^2 * 0.84 * 0.935^1 \pm 0.014 = 0.72 \pm 0.014 \\ T &= 72.38 \pm 1.4\% \end{aligned} \quad (3.10)$$

is the fraction of the laser power of  $P_1$  (from the measurement point between  $f_3$  and  $f_4$ ) which is transmitted to the atoms. The error in Equation (3.10) is small compared to the uncertainty of the power measurement itself. The absolute laser power can be measured within a precision of about

$$P_{\text{error}} = 5\%. \quad (3.11)$$

In conclusion, adding these errors the laser power at the position of the atoms is

$$\boxed{P = 0.72(6) * P_1.} \quad (3.12)$$

We have measured the powers at different laser currents  $I_D$  and AOM driver voltages  $U_{\text{Dimple}}$ . They are scaled by the factor of Equation (3.12) and plotted in Figures 3.12 and 3.13. With the linear fits in these figures, one can give an explicit formula for the resulting power:

$$P \approx \frac{P_{\text{fit}}(I_D)}{P_{\text{max}}} \frac{P_{\text{fit}}(U_{\text{Dimple}})}{P_{\text{max}}} * P_{\text{max}}, \quad P_{\text{max}} = 9.45\ \text{W} \quad (3.13)$$

$$\boxed{P \approx (U_{\text{Dimple}}/[V] * 1.000(2) - 1.05(8)) * (0.338(0) * I_D/[A] - 0.086(14))\ [\text{W}]} \quad (3.14)$$

for  $U_{\text{Dimple}} \in [1.5\ \text{V}, 7.5\ \text{V}]$ .

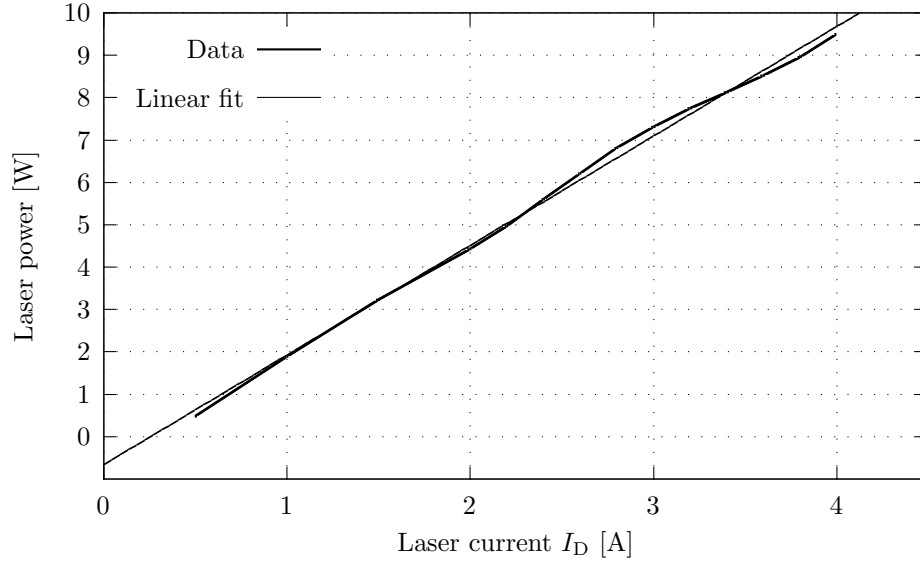


Figure 3.12: The expected laser power at the position of the atoms computed according to Equation (3.12) is shown with respect to the laser control current  $I_D$ . It was obtained by a power measurement between the lenses  $f_3$  and  $f_4$  of the second telescope. The linear fit  $P(I_D) = 2.59(4) * I_D - 0.66(11)$  provides a convenient reference.

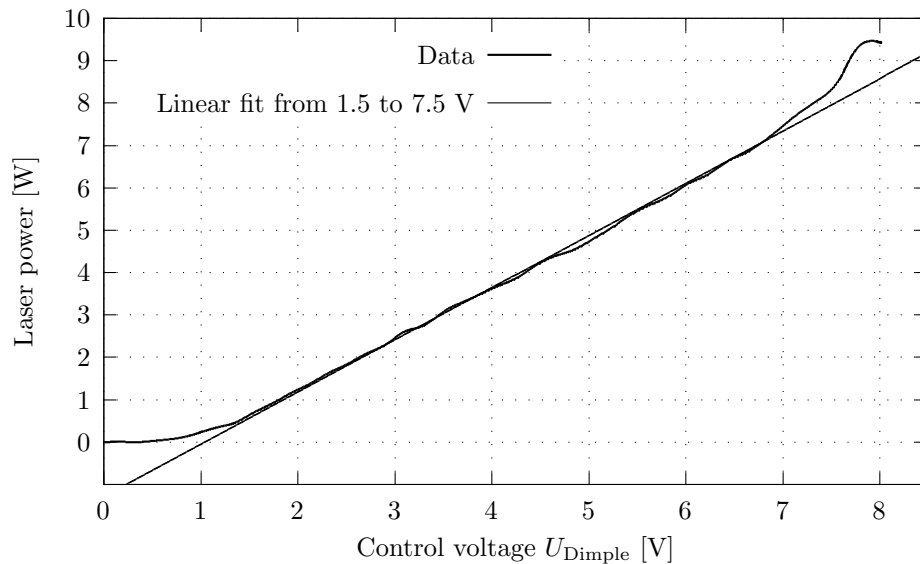


Figure 3.13: The power at the position of the atoms shows a linear dependence on the AOM control voltage  $U_{\text{Dimple}}$  between 1.5 and 7.5 Volts:  $P(U_{\text{Dimple}}) = 1.233(2) * U_{\text{Dimple}} - 1.29(1)$ . The data was obtained measuring the power of the stray light near the beam dump with a photo diode and scaling it to the maximum power at the position of the atoms.

### 3.6 Loading the Dimple

**ODT Ramp** For a maximum number of atoms in the dimple potential, it is best to ramp down the ODT potential. To find a ramp  $P_{\text{ODT}}(t)$  we split the ramp in three linear parts and scan the time for each ramp that leads to the highest gain in phase space density. The resultant ramp is summarized in Table 3.6.

The three parts of the ODT power ramp.			
Power at the beginning of the ramp	Power at the end	Ramp duration	Resulting slope
90 W	20 W	1 s	-70 W/s
20 W	5 W	1 s	-15 W/s
5 W	0 W	0.3 s	-16.7 W/s

Table 3.2: This ramp of the ODT results in the highest phase space density in the dimple. The parameters were obtained scanning the ramp durations (see text). In principle, the second and third ramps could be merged together, as they have about the same slope.

To achieve such a ramp, the motorized rotation stage of the ODT attenuator has to start rotating at the beginning of the second linear ramp.

**Evaporation Ramps.** We perform forced evaporation in the dimple to lower the temperature of the atomic cloud for stability considerations in Section 6.2. Table 3.6 shows how we ramp down the dimple potential in time.

The three parts of the dimple power ramp.			
Power at the beginning	Power at the end	Ramp duration	Resulting slope
$P(7.95 \text{ V}) = 9.45 \text{ W}$	$P(7.95 \text{ V}) = 9.45 \text{ W}$	0.2 s	0 W/s
$P(7.95 \text{ V}) = 9.45 \text{ W}$	$P(4.00 \text{ V}) = 3.61 \text{ W}$	1.5 s	-3.9 W/s
$P(4.00 \text{ V}) = 3.61 \text{ W}$	$P(3.00 \text{ V}) = 2.45 \text{ W}$	0.75 s	-1.5 W/s
$P(3.00 \text{ V}) = 2.45 \text{ W}$	$P(1.70 \text{ V}) = 0.87 \text{ W}$	0.5 s	-3.2 W/s

Table 3.3: These parameters are used for forced evaporation. They were obtained with similar methods to Table 3.6. The last ramp power sets the temperature of the atoms that remain in the trap. Thus, it is varied in experiments which investigate temperature behaviors.

# Chapter 4

## Trap Dynamics

### 4.1 Simulations

From the result of Equation (2.58), the equation for the Potential  $U(r, z)$ , we deduce the dynamics of atoms in an optical dipole trap. As this equation can be approximated harmonically for small distances from the radial center, simplifications occur.

In the following sections, we are interested in the radial direction of the potential landscape. For this purpose, and for the sake of simplicity, we can absorb the axial part in  $U_0$  and  $w_0$ :

$$U_0 \stackrel{\text{def.}}{=} U_0(z) = \frac{-U_0}{1 + (z/z_R)^2} \exp\left(\frac{1}{1 + (z/z_R)^2}\right) \quad (4.1a)$$

$$w_0 \stackrel{\text{def.}}{=} w(z) = w_0(z=0)(1 + (z/z_R)^2) \quad (4.1b)$$

Therefore, without restriction of any kind, Equation (2.58) reads

$$U(r, z) = -U_0 \exp(-2(r/w_0)^2) \quad (4.2)$$

Later, the  $z$ -dependence will be taken into account again.

#### 4.1.1 Harmonic Approximation

We expand Equation (4.2) to a second order Taylor polynomial at  $r = 0$

$$U(r) = -U_0 + 2U_0(r/w_0)^2 + \mathcal{O}(4). \quad (4.3)$$

The approximation

$$U(r) \approx -U_0 + 2U_0(r/w_0)^2 \quad (4.4)$$

is thereby valid if  $r^4 \ll w_0$ . The harmonic approximation is compared with  $U(r)$  in Figure 4.1.

The general solution of the equations of motion

$$m\ddot{r}(t) = -\frac{d}{dr}(-U_0 + 2U_0(r(t)/w_0)^2) \quad (4.5)$$

$$\ddot{r}(t) = \frac{-4U_0}{mw_0^2}r(t) \quad (4.6)$$

is given by

$$r(t) = A * e^{i(\omega_r t + \varphi)} = A * (\cos(\omega_r t + \varphi) + i \sin(\omega_r t + \varphi)) \quad (4.7)$$

with the angular frequency of

$$\omega_r = \sqrt{\frac{4U_0}{mw_0^2}}. \quad (4.8)$$

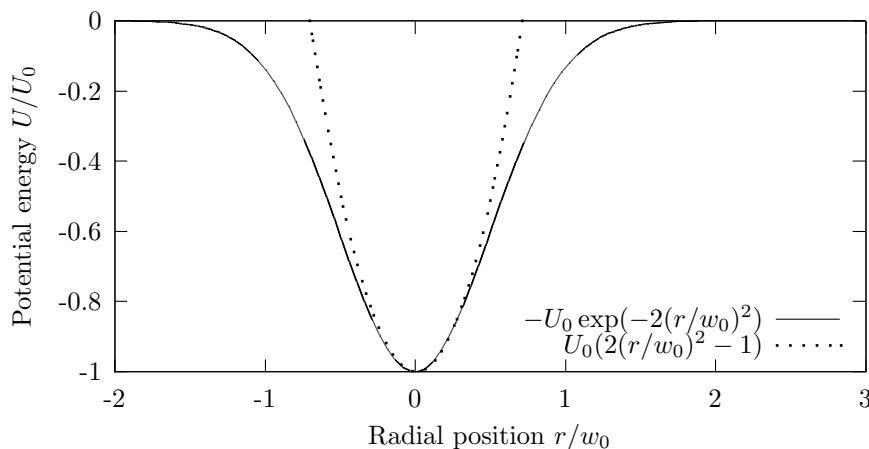


Figure 4.1: Depicted with a solid line is the potential energy for atoms in an optical dipole trap along the radial direction. The potential energy scale is in terms of the maximal trap depth  $U_0$  and the position in terms of the beam waist  $w_0$ . The second order Taylor expansion is a good approximation for atoms occupying the bottom of the potential. For example, if the atomic cloud is thermalized and not in contact with a particle reservoir, the approximation can be applied.

Of course, only the real part

$$\Re(r(t)) = A * \cos(\omega_r t + \varphi) \quad (4.9)$$

can be observed in a classical treatment. The benefit of a harmonic potential sure is that all trajectories have the same frequency and a sinusoidal behavior.

For more than one concentric harmonic potentials with maximum depths of  $\{U_0^i\}_{i \in \mathbb{N}}$  and waists of  $\{w_0^i\}_{i \in \mathbb{N}}$ , the trap frequency can be stated with a calculation similar to the one from above:

$$\omega_r = \sqrt{\frac{4}{m} \sum_i \left( \frac{U_0^i}{(w_0^i)^2} \right)} = \sqrt{\sum_i ((\omega_r^i)^2)}. \quad (4.10)$$

In the following part, we will derive equations with a close link to the experiments.

The trap depth

$$U_0 = a * I \quad (4.11)$$

has a linear dependence on the intensity  $I$  with a proportionality constant of

$$a = 0.273 * 10^{-36} \frac{\text{Jm}^2}{\text{W}} \quad \text{for } ^{52}\text{Cr} \text{ with } \lambda = 1064 \text{ nm} \quad [14] \quad (4.12)$$

at the typical optical dipole trap wavelength  $\lambda$ . The intensity of the beam

$$I = \frac{2P}{\pi w_0^2} \quad (4.13)$$

can be expressed in terms of the laser power  $P$ , which can easily be measured and which in contrast to  $I$  stays constant as the beam con- or diverges. With equations (4.11) and (4.13), the trap frequency Equation (4.8) simply becomes

$$\omega_r = \sqrt{\frac{8aP}{m\pi w_0^4}} = \sqrt{\frac{8aP}{m\pi}} * w_0^{-2}. \quad (4.14)$$

However, in the experiment, we have to take an aspect ratio of  $w_x/w_y \neq 1$  into account, i.e. an **elliptic beam profile** and the loss of the cylindrical symmetry ( $r \rightarrow x, y$ ). Also, there is always a

finite **astigmatism** involved which leads to  $x$ - and  $y$ -foci at different positions:  $z_{\text{focus},x} \neq z_{\text{focus},y}$ . If the the distance between the foci is on the same length scale as the RAYLEIGH length of either direction or larger, it cannot be neglected any more as it changes the intensity

$$I = \frac{2P}{\pi w_x w_y} \quad (4.15)$$

due to the ellipticity of the beam spot. The trap frequencies

$$\omega_x = \sqrt{\frac{4aI}{mw_x^2}} \quad (4.16a)$$

$$\omega_y = \sqrt{\frac{4aI}{mw_y^2}} \quad (4.16b)$$

thus write

$$\omega_x = \sqrt{\frac{8aP}{m\pi w_x^3 w_y}} \quad (4.17a)$$

$$\omega_y = \sqrt{\frac{8aP}{m\pi w_y^3 w_x}}. \quad (4.17b)$$

These two equations can be solved for the beam waists:

$$w_x = \left( \frac{8aP\omega_y}{m\pi\omega_x^3} \right)^{1/4} \quad (4.18a)$$

$$w_y = \left( \frac{8aP\omega_x}{m\pi\omega_y^3} \right)^{1/4}. \quad (4.18b)$$

Now, we can express the trap depth in terms of either the beam waists or the trap frequencies:

$$U_0 = \frac{2aP}{\pi w_x w_y} = \sqrt{\frac{maP\omega_x\omega_y}{2\pi}} \approx 6.12 * 10^{-32} \text{Js} * \sqrt{P\omega_x\omega_y} \quad (4.19)$$

In the middle of the foci, i.e., at the position where the beam profile is circular, the trap frequencies are the same ( $\omega_x/\omega_y = 1$ ) and the beam waists at that position are

$$w_{i \in \{x,y\}} = \left( \frac{8aP}{m\pi} \right)^{1/4} \frac{1}{\sqrt{\omega_i}} = w_r \quad (4.20)$$

like in the non astigmatic case.

For an experimental physicist, it is important to know the sensitivity of the available tuning parameters, one of which is certainly the axial focus position

$$z_{\text{focus}} \stackrel{\text{def.}}{=} (z_{\text{focus},x} + z_{\text{focus},y})/2, \quad (4.21)$$

defined as the middle of the astigmatic foci. We would like to derive formulae for the  $z$ -dependence of  $U(z)$  and  $\omega_i(z)$ . Therefor we insert Equation (2.57) into Equation (4.19):

$$U(z) = \frac{2aP}{\pi w_{0x} w_{0y}} \left[ 1 + \left( \frac{\lambda(z - z_{\text{focus},x})}{\pi w_{0x}^2} \right)^2 \right]^{-1/2} \left[ 1 + \left( \frac{\lambda(z - z_{\text{focus},y})}{\pi w_{0y}^2} \right)^2 \right]^{-1/2} \quad (4.22)$$

With formulae (2.57) and (4.17 a,b), we can express the  $z$ -dependence of the trap frequencies in terms of the beam waists:

$$\omega_x = \sqrt{\frac{8aP}{m\pi w_{0x}^3 w_{0y}}} \left[ 1 + \left( \frac{\lambda(z - z_{\text{focus},x})}{\pi w_{0x}^2} \right)^2 \right]^{-3/4} \left[ 1 + \left( \frac{\lambda(z - z_{\text{focus},y})}{\pi w_{0y}^2} \right)^2 \right]^{-1/4} \quad (4.23)$$

$$\omega_y = \sqrt{\frac{8aP}{m\pi w_{0y}^3 w_{0x}}} \left[ 1 + \left( \frac{\lambda(z - z_{\text{focus},y})}{\pi w_{0y}^2} \right)^2 \right]^{-3/4} \left[ 1 + \left( \frac{\lambda(z - z_{\text{focus},x})}{\pi w_{0x}^2} \right)^2 \right]^{-1/4} \quad (4.24)$$

The trap frequency in  $\vec{e}_z$  direction is given by [14]

$$\omega_z = \sqrt{\frac{2U_0}{mz_0^2}}. \quad (4.25)$$

The derivation is the same as the derivation of equation 4.8: second order Taylor expansion and solution of the differential equation. With relation (2.55), we can derive a formula that links the trap frequencies  $\omega_r$  and  $\omega_z$  in case of a circular beam profile:

$$\omega_z = \sqrt{\frac{2U_0}{mz_0^2}} = \sqrt{\frac{2U_0\lambda}{m\omega_0^2 z_0 \pi}} = \sqrt{\frac{4U_0}{m\omega_0^2}} \sqrt{\frac{\lambda}{2\pi z_0}} = \omega_r \sqrt{\frac{\lambda}{2\pi z_0}} \quad (4.26)$$

### 4.1.2 Anharmonic Trap

In the experiment, we have the dimple potential inside the ODT potential. If we are interested in the trap frequencies of the dimple, we have to take into account that the atoms can have energies that exceed the trap depth of the dimple  $U_0$ , but are still confined by the ODT. This means that a large fraction of atoms is at energies where the harmonic approximation from Equation (4.4) is invalid. The theoretical description becomes more complicated, since the equation of motion of a classical particle

$$m\ddot{x}(t) = -\frac{dU(x(t))}{dx} = 2U_0 \frac{x(t)}{w_0^2} \exp\left(-2\left(\frac{x(t)}{w_0}\right)^2\right) \quad (4.27)$$

is highly nonlinear! However, with the aid of computer power, we can still solve this differential equation numerically. Figure 4.2 shows the trajectories for three particles with different energies. Note that we will only perform a classical simulation. For a quantum mechanical treatment, one would have to treat the problem of the following nonlinear Schrödinger equation:

$$\left( \frac{\hbar^2}{2m} \frac{d^2}{dx^2} + U_0 e^{-(\hat{x}/w)^2} \right) \Psi = E\Psi. \quad (4.28)$$

For the sake of simplicity, we stick to Equation (4.27) and the MAXWELL-BOLTZMANN-distribution

$$f(E) = 2\sqrt{E/\pi}(k_B T)^{-3/2} e^{-E/(k_B T)}. \quad (4.29)$$

In this simulation, only energies below the trap depth  $E < U_0$  are considered, so the distribution is normalized to the truncated version. The initial conditions are

$$\text{Position } x = x(E) \in [0, 10w_0 = 160 \mu\text{m}] \quad (4.30a)$$

$$\text{Velocity } \dot{x} = 0. \quad (4.30b)$$

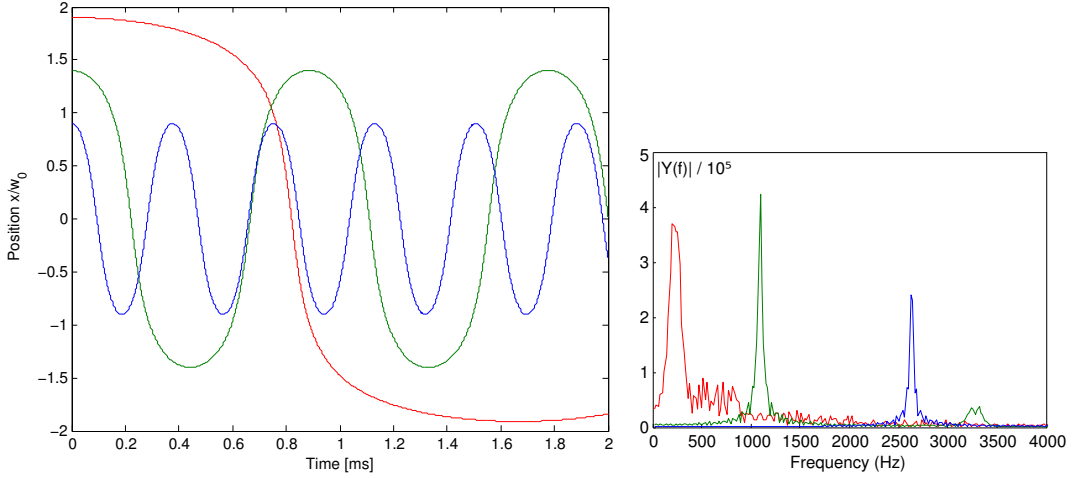


Figure 4.2: Trajectories of three trapped  $^{52}\text{Cr}$  atoms with different energies in an ODT (classical calculation). The higher the energy, the lower the frequency of the oscillation as particles are exposed to weak restoring forces in the wings of the potential. Clearly, the sinusoidal behavior vanishes for high amplitudes.

The trajectories are calculated until the atom crosses  $x = 0$  which happens at one quarter of a period  $t_0 = T/4$ . So, the frequency  $\omega = 8\pi/t_0$  is obtained.\* The probability to find an atom in the trap frequency interval  $[\omega - d\omega/2, \omega + d\omega/2]$  can be calculated

$$f((E(\omega)) dE = f((E(\omega)) \frac{dE}{d\omega} d\omega \stackrel{\text{def.}}{=} f_\omega(\omega) d\omega. \quad (4.31)$$

The calculated probability density  $f_\omega(\omega) d\omega$  is plotted in Figure 4.3.

The simulations show that for a measurement of the trap frequencies, it is crucial to have a cold atomic cloud compared to the trap depth  $U_0/k_B$ .

## 4.2 Experiments

In Section 3.5, an expectation value for the laser power at the position of the atoms has been deduced. However, as can be seen from Equation (4.19), the trap depth is proportional to  $(w_x w_y)^{-1}$ . If the setup differs from the optics simulations and the preliminary setup, the beam waists  $w_x$  and  $w_y$  will differ from the desired value, i.e.  $10 \mu\text{m}$ , and therefore the trap depth will change as well. To check the resulting trap depth, we perform *parametric heating* experiments. In these experiments, the power of the laser beam is modulated around its average power  $P$ :

$$P_{\text{mod}}(t) = P(1 + M \sin(\omega t)) \quad (4.32)$$

with the control voltages at the 123 MHz AOM driver

$$U(t) = U_{\text{Dimple}} + \tilde{U}_{\text{mod}} \sin(\omega t). \quad (4.33)$$

For the measurements in this chapter, we set  $U_{\text{Dimple}} = 6 \text{ V}$  to the linear regime of the power characteristics  $P(U_{\text{Dimple}})$  in Figure 3.13. Usual values of the relative modulation  $M$  are from 0.1 to 1%. †

\*The reason why the frequency is not taken from the Fourier transform is computational. For the Fourier transform, it is best to have many oscillations. For 150 oscillations, more than  $10^7$  time steps are necessary for the amplitude to stay constant, which is a sign of sufficient resolution. Since these data points have to be saved in an array, limited memory becomes an issue.

†In the early measurements, it is convenient to start with a higher modulation like 5% for a clear yet coarse signal.

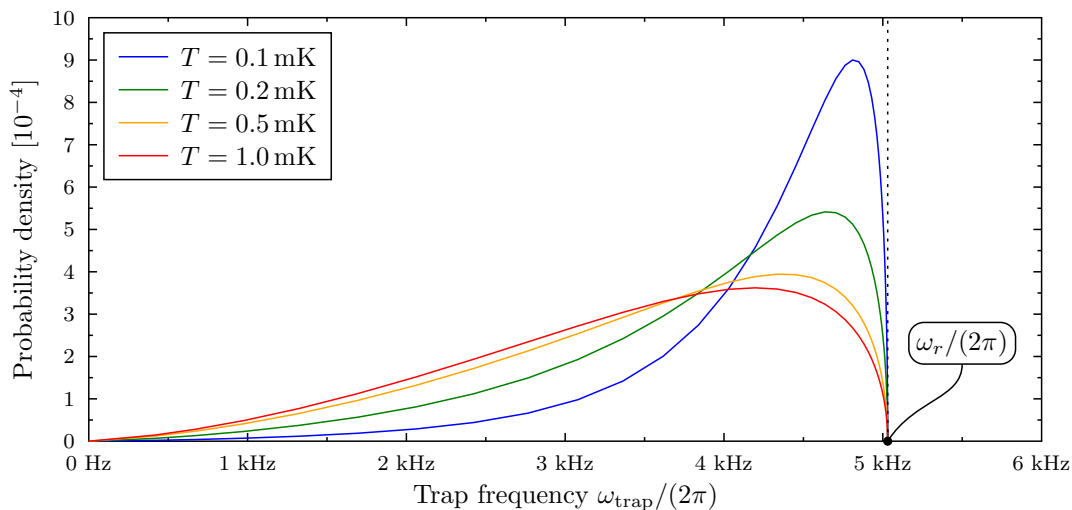


Figure 4.3: This figure shows the distribution of trapped chromium atoms in the dimple over the trap frequencies for a trap depth of  $U_0 = 0.4$  mK and a beam waist of  $16 \mu\text{m}$ . At small temperatures (blue) compared to the trap depth  $U_0/k_B$ , the atoms are more likely to have a small oscillation amplitude compared to the laser waist  $x_0/w_0$  and therefore have trap frequencies closer to  $\omega_r$ , the trap frequency of the harmonically approximated potential.

The modulation can excite atoms if its frequency  $\omega$  is twice as high as the oscillation frequency of the atoms,  $\omega_r$  in the harmonic approximation. This can be understood in the following figurative description: If the trap is deeper once an atom travels towards the center than it is by the time when it leaves the center again, it will gain kinetic energy.

Therefore, having obtained this frequency  $\omega = 2\omega_r$ , the atomic cloud will heat up and atoms with high energies will leave the trap.

### 4.2.1 Laser Intensity Modulation

Before conducting the actual parametric heating experiments, it is desirable to know how well the setup modulates the laser intensity and how the control parameters map onto the modulation. For this, stray light of the laser intensity is detected with a photo diode in the area of the beam dump  $\text{BD}_2$ . The signal was recorded for one second with a sample rate of 500 kHz using a digital oscilloscope\*. A fast Fourier transformation (FFT) has been calculated, see Figure 4.4.

From the amplitude of the peak frequency of the FFT, one can deduce the modulation amplitude. This has been done for the following frequency/control voltage combinations:

Frequency $f = \omega/(2\pi)$ [kHz]	1	1	6	6	6	10	10	20	20
Modulation voltage $\tilde{U}_{\text{mod}}$ [V]	0.2	0.5	0.1	0.2	1	0.2	0.5	0.2	0.5

Table 4.1: Parameters for the modulation strength measurement of Figure 4.5.

The obtained modulations in Figure 4.5 are normalized to  $\tilde{U}_{\text{mod}} = 1$  V, which leads almost to the same values at one frequency. It shows that the electronics works linearly, in particular the summation of the modulation voltage  $U_{\text{Modulation}}$  and the constant voltage  $U_{\text{Dimple}}$ . From

\*Lecroy waveRunner 64Xi 600 MHz 60 GS/s

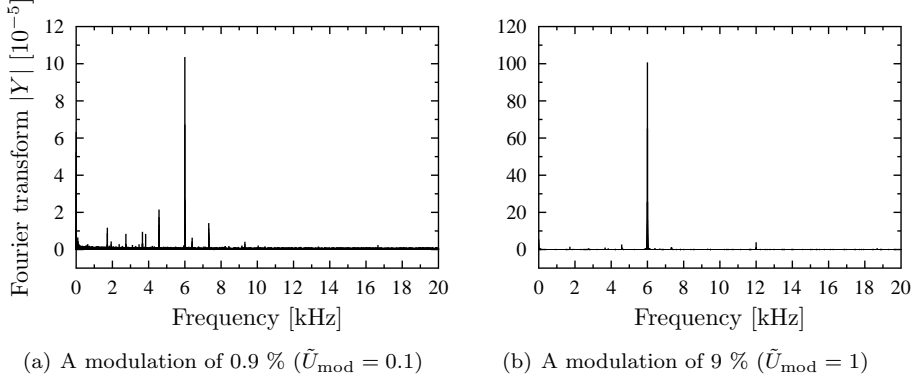


Figure 4.4: These plots show the frequency distributions of the laser intensities at different modulation strengths. The intensity is modulated at a frequency of 6 kHz, represented by the highest peak in each plot. Comparing the scales, we see that the modulation is linearly dependent on  $\tilde{U}_{\text{mod}}$ . If the modulation is high (b) such that nonlinearities cannot be neglected, the second harmonic can be observed at 12 kHz. All relevant measurements were conducted at modulation strengths where higher orders cannot be detected any more.

the exponential fit in Figure 4.5 at  $\tilde{U}_{\text{mod}} = 1$  V, we generalize

$$M(\tilde{U}_{\text{mod}}) = (8.78 * e^{-f/14.12} + 3.57) * \tilde{U}_{\text{mod}} \quad (4.34)$$

The modulation can be normalized if we set

$$\tilde{U}_{\text{mod}}(f) = \frac{M_0}{(8.78 * e^{-f/14.12} + 3.57)} \quad (4.35)$$

Then, the modulation is always given by

$$M(M_0) = M_0 [\%]. \quad (4.36)$$

### 4.2.2 Parametric Heating – Extraction of Results

We have pointed out the significance of this experiment in the introduction of Section 4. The result of a parametric heating experiment can be seen in Figure 4.6.

The number of atoms is fitted with a Lorentzian

$$L(f) = c - \frac{a}{(1 + (2 * (f - f_0)/\delta_f)^2)}, \quad (4.37)$$

with fit parameters  $c$ : off-resonant number of atoms,  $a$ : number of atoms heated out at resonance,  $\delta_f$ : width of resonance, and most importantly the resonance frequency  $f_0$ .

We can also look at the cloud width, as it shall expand near resonance due to heating. The same fit Equation (3.12) as above can be used except that two of the fit parameters have a different physical meaning:  $c$  is the cloud width off-resonance and  $a$  is the gain of width on resonance.

### 4.2.3 Influences on the Signal

Now that the methods are explained, we can study the trap frequencies in detail.

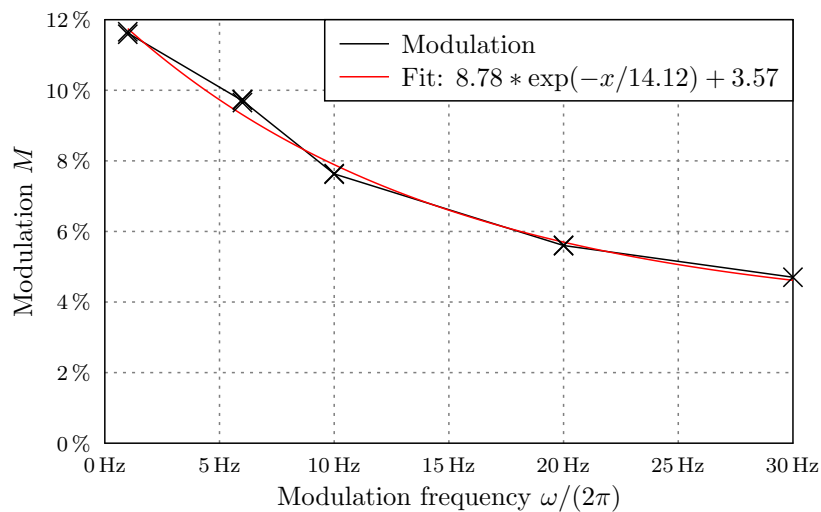


Figure 4.5: The intensity modulation decreases with growing frequency like a low-pass filtered signal. If we keep this dependency in mind, it is no handicap because it can be compensated with a frequency-dependent voltage  $\tilde{U}_{\text{mod}}(f)$ , see text.

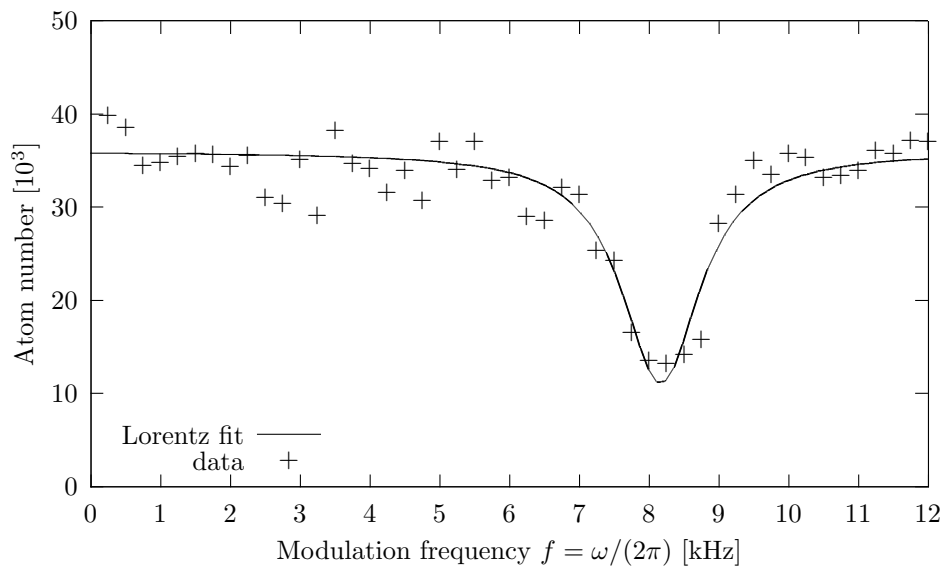


Figure 4.6: In this example of a parametric heating experiment, the number of atoms gives the information about the resonance frequency  $\omega_r$ .

**Modulation Amplitude.** At high modulations  $M$ , the number of atoms approaches zero ( $a \approx c$ ) and the resonance is broad –  $\delta_f$  is large. Compare the orange, green and blue curves in Figure 4.8. The physical explanation for this kind of behavior lies in the different amount of energy that can be transferred to the atoms. It increases with the modulation  $M$ , since the energy transferred to the atoms can in principle be in the order of the absolute modulation  $MU(\vec{r})$  of the potential. The reason for this power broadening will be given in the **Temperature** paragraph. Please note the peak's asymmetry with a smaller slope towards lower frequencies.

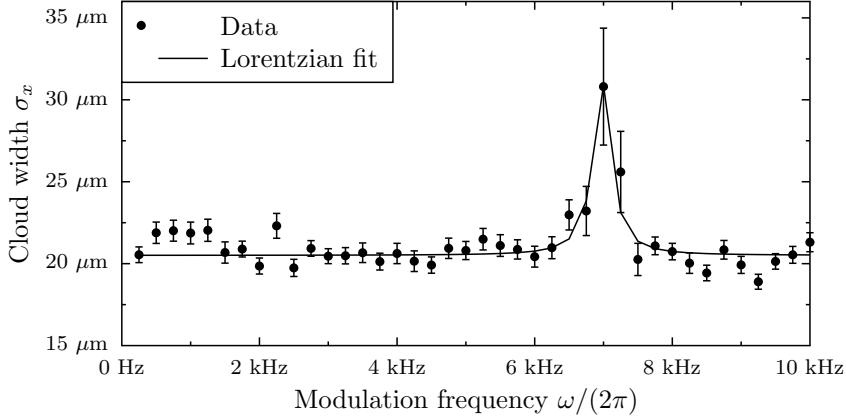


Figure 4.7: This is an example of a parametric heating experiment where the cloud width  $\sigma_x$  is used to determine the resonance frequency.

**Frequency Sweep.** For data point  $i$ , the modulation frequency is swept from  $modfreq(i)$  to  $modfreq(i+1)$  within the time  $t_{\text{sweep}}$ , usually 0.1 to 5 seconds. With this frequency sweep, it is impossible to miss the resonance frequency if it is between  $modfreq(i)$  and  $modfreq(i+1)$ . That could happen if the frequency is kept constant during modulation. For a sufficiently high sampling rate, however, that problem is not present as the frequency resolution is smaller than the resonance:

$$modfreq(i+1) - modfreq(i) < \delta_f \quad (4.38)$$

in order to have more data points in  $[f_0 - \delta_f, f_0 + \delta_f]$ . With the frequency sweep, it might be possible to address more atoms, but, since the dynamics is rather complicated, it is hard to tell.

**Modulation Time.** The energy  $E_{\text{transferred}}$  which can be transferred to the atoms is proportional to the time  $t_{\text{sweep}}$  they are exposed to the modulation. Understanding the modulation as a power  $P_{\text{mod}} = E_{\text{transferred}}/t_{\text{sweep}}$  provides an intuitive picture for this behavior.

#### 4.2.4 ODT ramp and Temperature.

We have calculated that a wide range of trap frequencies are populated at high temperatures (Section 4.1.2). We will explore this now experimentally. Once the hybrid trap is loaded in equilibrium condition, we use forced evaporation to cool down the atoms. The final power of the ODT determines the temperature of the cloud. There are parametric heating experiments with two different ODT ramps – to 15 W and to 1 W – in Figure 4.8. Even though the modulation at 15 W is higher than the modulation in the scan represented by the orange curve, the number of atoms drops only to about 50 % in contrast to 100 % (orange curve). There are two explanations for this phenomenon:

- The probability distribution over the trap frequencies is biased towards smaller trap frequencies and is more spread like in Figure 4.3 of Section 4.1.2. Therefore, only little atoms can be excited in an interval  $[modfreq(i), modfreq(i+1)]$ .
- If the final ODT power is still high (15 W), atoms that are still trapped outside the dimple, i.e. in the hybrid trap cannot be neglected. During the modulation, they can fill up the number of atoms in the dimple again. This rather technical issue could in principle be circumvented, but, in our case, the ODT power region of 1 W to 15 W is only accessible in combination with a motorized lambda plate as a part of a beam splitter. This complicates the situation.

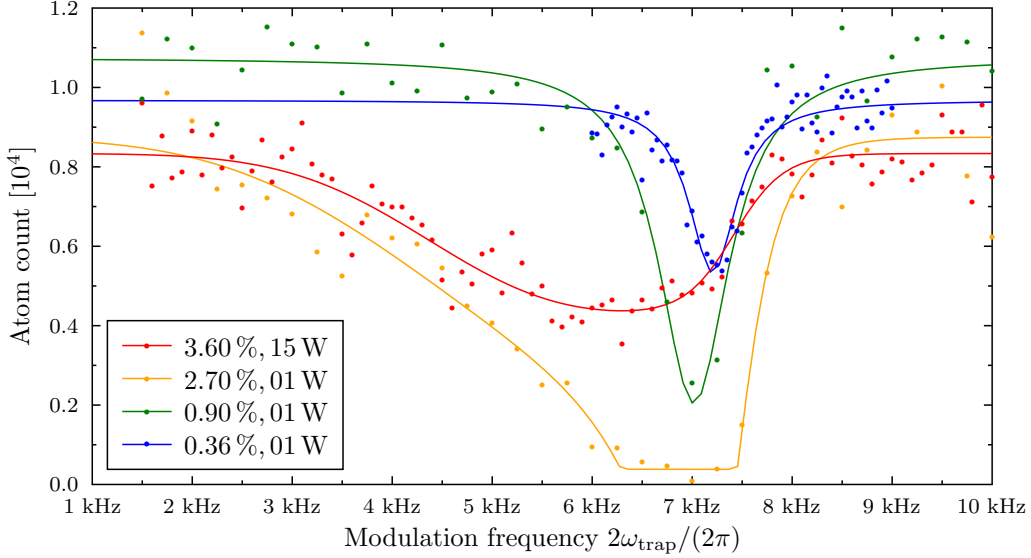


Figure 4.8: Parametric heating of the atoms in the dimple at different modulations  $M$  and final ODT powers after the ramp  $P_{\text{evap}}$  denoted in the key by “ $M$  [%],  $P_{\text{evap}}$  [W]”. The blue and green solid lines are Lorentzian fits of the data (dots). At small values of  $P_{\text{evap}}$  and small modulations, the resonance is narrow and close to double the harmonic trap frequency  $2\omega_r$ . The red and yellow lines are guides for the eye. Due to saturation (yellow) and asymmetry (yellow and red) a Lorentzian is not the correct fit model. Both curves show a dependence on  $P_{\text{evap}}$ . The surrounding particle reservoir can fill up the dimple so that the number of atoms will not drop to zero (red). The reason for the asymmetric shape (yellow and red) is the power broadening towards small frequencies as the harmonic approximation fails.

#### 4.2.5 The Position of the Dimple Focus.

The idea behind this analysis is that we can shift the dimple focus in the direction of the dimple laser beam relative to the ODT and thereby change the beam waist and maximum intensity at the position of the atoms. The atoms are still confined at the same position by the ODT. The relevant shift in both directions  $\pm \vec{e}_z$  is given by the order of magnitude of the expected RAYLEIGH range  $200 \mu\text{m} < z_R < 300 \mu\text{m}$ . This shift can be realized with the actuator of the translation stage of  $f_4$ , see Table 3.4. Within the shift range, the change of the beam convergence angle can well be neglected and therefore the RAYLEIGH range stays constant as well.

With this technique, the beam profile and the potential landscape can be measured. Since many loading processes (about 800) are necessary, one major advantage of the setup once more comes to play: the rapid production of ultra-cold atomic clouds with the scheme presented in Section 3.1. From each frequency scan, the trap frequencies have been extracted using the methods described in Section 4.2.2. They are plotted in Figure 4.9.

In order to obtain the influence of the dimple, we have to account for other potentials contributing to the overall potential first. The trap frequencies of the single harmonic potentials combine to the total trap frequencies according to Equation (4.10)

$$\omega_{\text{total}} = \sqrt{\omega_{\text{Dimple}}^2 + \omega_{\text{ODT}}^2 + \omega_{\text{BC}}^2}. \quad (4.39)$$

Therefore, to get information about the dimple potential measuring the total trap frequency, one has to calculate

$$\omega_{\text{Dimple}} = \sqrt{\omega_{\text{total}}^2 - \omega_{\text{ODT}}^2 - \omega_{\text{BC}}^2}. \quad (4.40)$$

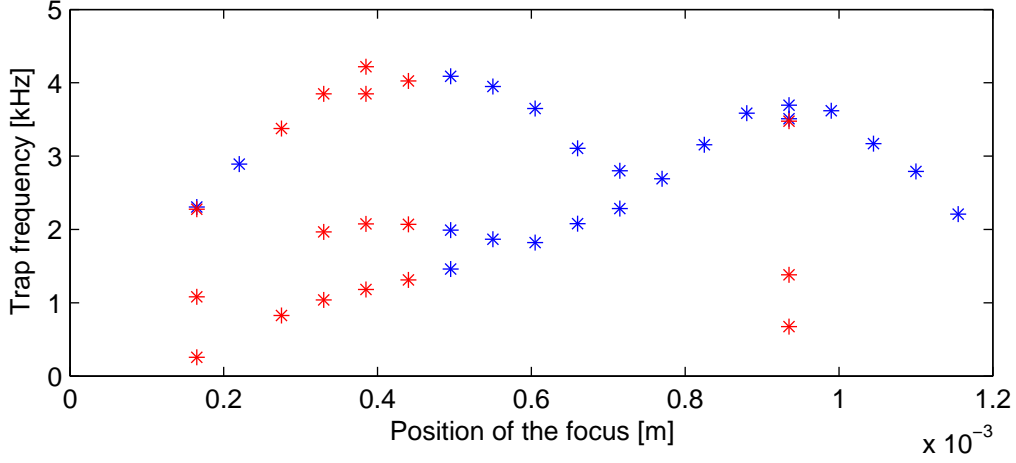


Figure 4.9: Red data points are the trap frequencies extracted from the cloud widths, blue data points are from the atom count. The  $x$ -scale is calculated from Table 3.4. The large bumps correspond to the confinement in  $\vec{e}_y$ - (left) and in  $\vec{e}_x$ - (right) directions. The feature with a peak at 0.4 mm and 2 kHz has half the frequency of the  $f_y$  curve. An explanation is the modulation of the position of the local potential minimum if the dimple is not aligned concentric with the ODT. Such a modulation is resonant at the trap frequency. For this feature, the plot shows half the trap frequency due to the division of the all resonance frequencies by 2.

The trap frequencies of the optical dipole trap and of the barrier coils' potential are given by [32]

$$\omega_{\text{ODT},x} = 2 * \pi * 35.52 * \sqrt{P_{\text{ODT}}} \frac{\text{Hz}}{\sqrt{W}} \quad (4.41)$$

$$\omega_{\text{ODT},y} = 2 * \pi * 559.7 * \sqrt{P_{\text{ODT}}} \frac{\text{Hz}}{\sqrt{W}} \quad (4.42)$$

$$\omega_{\text{BC},x} = 2 * \pi * 251.8 * \sqrt{I_{\text{BC}}} \frac{\text{Hz}}{\sqrt{W}}. \quad (4.43)$$

$P_{\text{ODT}}$  denotes the ODT laser power (here 15 W),  $I_{\text{BC}}$  denotes the current through the barrier coils (here 1.3 A).  $\vec{e}_x$  is defined as the direction of the ODT laser, and  $\vec{e}_y$  is per definition both perpendicular to  $\vec{e}_x$  and to the direction of the dimple laser beam  $\vec{e}_z$ . The barrier coils potential along  $\vec{e}_y$  can be neglected:

$$|\omega_{\text{BC},y}| \ll \omega_{\text{ODT},y}. \quad (4.44)$$

We see that the main contribution comes from the ODT along  $y$ :  $\omega_{\text{ODT},y}$ . This will be the minimum trap frequency, called  $\omega_{\text{offset},y}$ , one can measure in the  $y$ -direction. The reason why the offset trap frequencies

$$\omega_{\text{offset}} = \sqrt{\omega_{\text{ODT}}^2 + \omega_{\text{BC}}^2} \quad (4.45)$$

arising from the hybrid trap can hardly be measured at large focus shifts is the decrease of the absolute modulation with the dimple potential, i.e. proportional to

$$U_{0i}(z) = \frac{-U_{0i}}{1 + ((z - z_{\text{focus},i})/z_{Ri})^2} \exp\left(\frac{1}{1 + ((z - z_{\text{focus},i})/z_{Ri})^2}\right), \quad (4.46)$$

cf. Equation (4.1a). With this argumentation, the left feature of Figure 4.9 is identified with the direction  $\vec{e}_y$ .

Having performed these measurements at 2.75 W of possible 9.45 W, we can scale the trap frequencies with the square root behavior investigated in Section 4.2.6. We

$$\text{replace } \omega_{\text{Dimple}} \text{ with } \omega_{\text{Dimple}} \sqrt{\frac{9.45 \text{ W}}{2.75 \text{ W}}}. \quad (4.47)$$

In locations  $z$ , where we have measured both frequencies  $\omega_{\text{total},x}$  and  $\omega_{\text{total},y}$ , we can calculate the trap depth and the beam waists using equations (4.19) and (4.18 a,b) respectively. For a wider range, the trap frequencies  $\omega_{\text{total},y}$  have been continued using mirrored trap frequencies of  $\omega_{\text{total},y}$  at the intersection point in Figure 4.10. We can do this because after the subtraction of the contributions from the other potentials, the trap frequency should be symmetric in the center. To obtain the beam waist  $w_x$ , this approximation is good, since, according to Equation

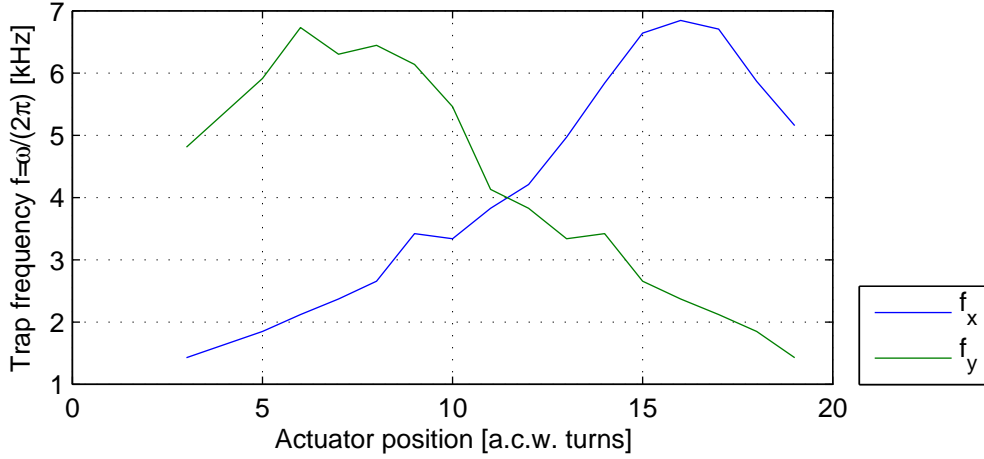


Figure 4.10: Trap frequencies of the dimple potential. The frequency part arising from other potentials has been subtracted. The frequencies  $f_y$  have been continued using the mirrored data of  $f_x$ . The data is scaled from 2.75 W to the maximum laser power of 9.45 W. For explanations, see text.

(4.18 a), it is proportional to  $\sqrt[4]{\omega_y}$ . Furthermore, this region is essential for the  $w_x$  fit in Figure 4.11 because it contains the minimum of the function. For the same reason, these data points are not crucial for the  $f_y$  fit. The respective fits are primarily interesting revealing the position scale. The fit function is from Equation (2.57) with a rescaled  $z$  axis:

$$w_i = w_{0i} \sqrt{1 + \left( \frac{\lambda a * (z - z_{\text{focus},i})}{\pi w_{0i}^2} \right)^2}. \quad (4.48)$$

For the fits, we use  $w_{0i}$ , the scaling factor  $a$  and  $z_{\text{focus},i}$  as free parameters. Both functions fit well to the data and result give rise to a different scaling than the preliminary setup had:

The trap depth can be calculated from the trap frequencies  $\omega_x$ ,  $\omega_y$  and the laser Power  $P = 9.45 \text{ W}$  using Equation (4.19). It can also be calculated with the waist fits using the same equation. Both are plotted in Figure 4.12.

As a result of this copious analysis, the trap depth is about five times smaller than expected. The beam waists in both directions reach about  $10 \mu\text{m}$  as planned but the astigmatism turned out to be stronger.

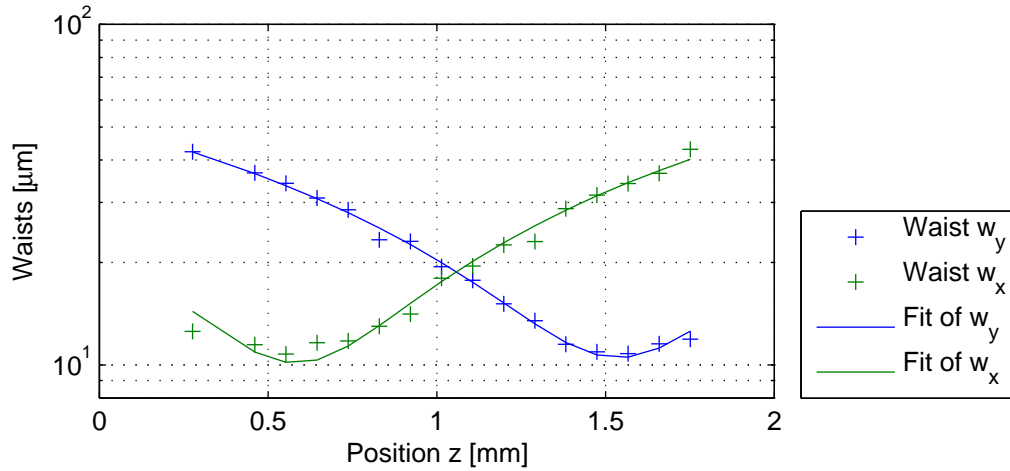


Figure 4.11: The figure shows the beam waist components of the astigmatic beam profile. The data points are calculated from the trap frequencies, the solid lines are fits using the function in Equation (4.48).

Preliminary setup, excerption of Table 3.4		
Degree of freedom	Step size	New focus position
$f_4 : -\vec{e}_z$ towards $M_5$	5 mm $\hat{=}$ 10 turns	-550 $\mu\text{m}$ $\vec{e}_z$
Setup		
Degree of freedom	Step size	New focus position
$f_4$ towards $M_5$	5 mm $\hat{=}$ 10 turns	$10 * a_x = 839 \mu\text{m}$ further
$f_4$ towards $M_5$	5 mm $\hat{=}$ 10 turns	$10 * a_y = 957 \mu\text{m}$ further
$f_4$ towards $M_5$	5 mm $\hat{=}$ 10 turns	mean value: <b>898 <math>\mu\text{m}</math></b> further

Table 4.2: The dependence of the actuator of lens  $f_4$  on the axial shift of the focus position in the preliminary setup and in the actual setup is compared.

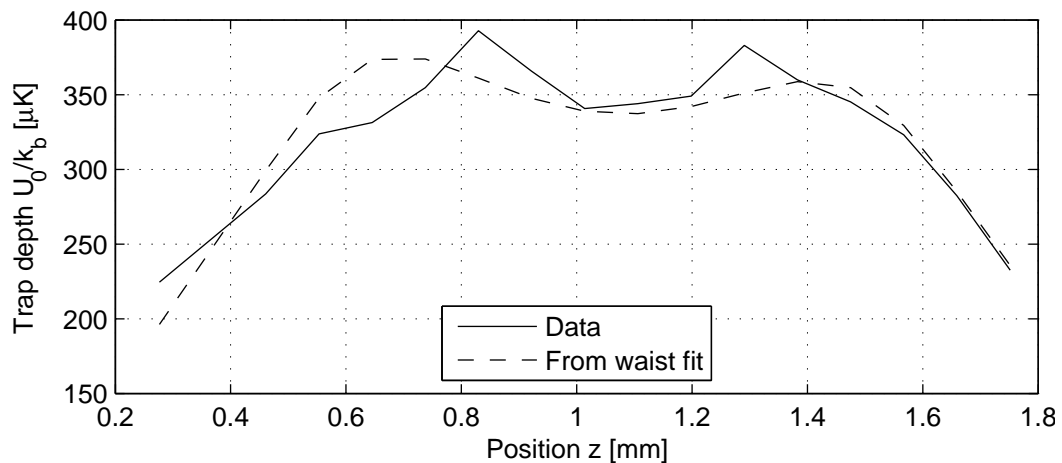


Figure 4.12: From top to bottom: trap frequencies, beam waists and trap depth. The data is scaled from 2.75 W to the maximum laser power of 9.45 W. For explanations, see text.

### 4.2.6 Dimple Laser Power.

To support the methods from Section 4.2.5, we examine the power dependence of the trap frequencies. Measuring the trap frequency along  $\vec{e}_y$ , the fit model is

$$\omega_{\text{total}} = \sqrt{\omega_{\text{ODT}}^2 + \omega_{\text{Dimple}}^2}. \quad (4.49)$$

$\omega_{\text{Dimple}}$  scales with the square root of the laser power, as can be seen from Equation (4.14). Therefore, we choose the function

$$\omega_{\text{total}} = 2\pi\sqrt{(1084\text{ Hz})^2 + a^2 * P} \quad (4.50)$$

which we fit to the measured data in Figure 4.13.

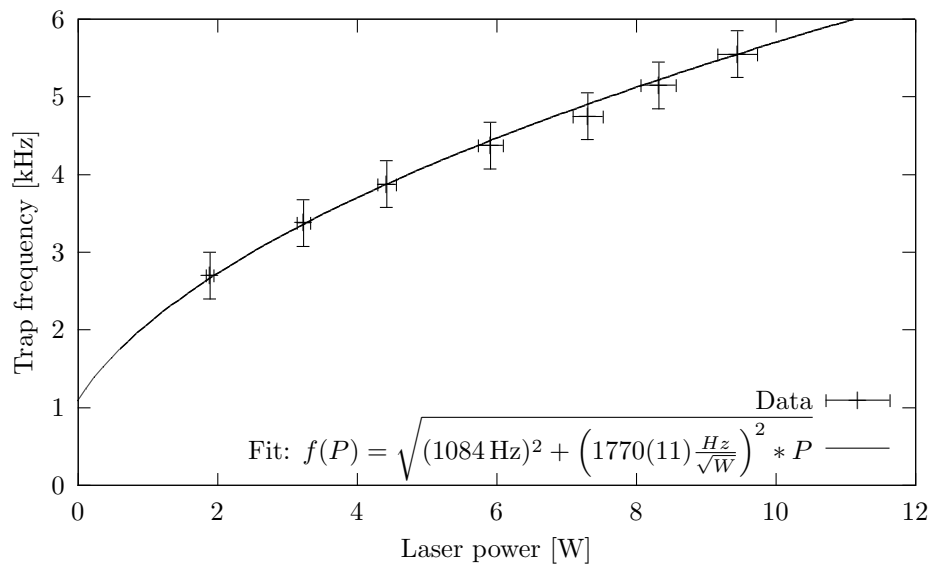


Figure 4.13: The resonance frequency has a square root dependence on the laser power.

It turns out, the dimple trap frequency is given by

$$\omega_{\text{Dimple}} = 2\pi * 1770(11) \frac{\text{Hz}}{\sqrt{W}} * \sqrt{P} \quad (4.51)$$

## Chapter 5

# Loading Performance

The influence of the final ODT power after the ramp, which, in Table 3.6 is  $PODTevap6 = 0$ , has been studied. For two different dimple laser powers (2 A and 4 A), the temperatures of the cloud in the dimple have been measured using the methods discussed in Section 5.2. The result is in Figure 5.1.

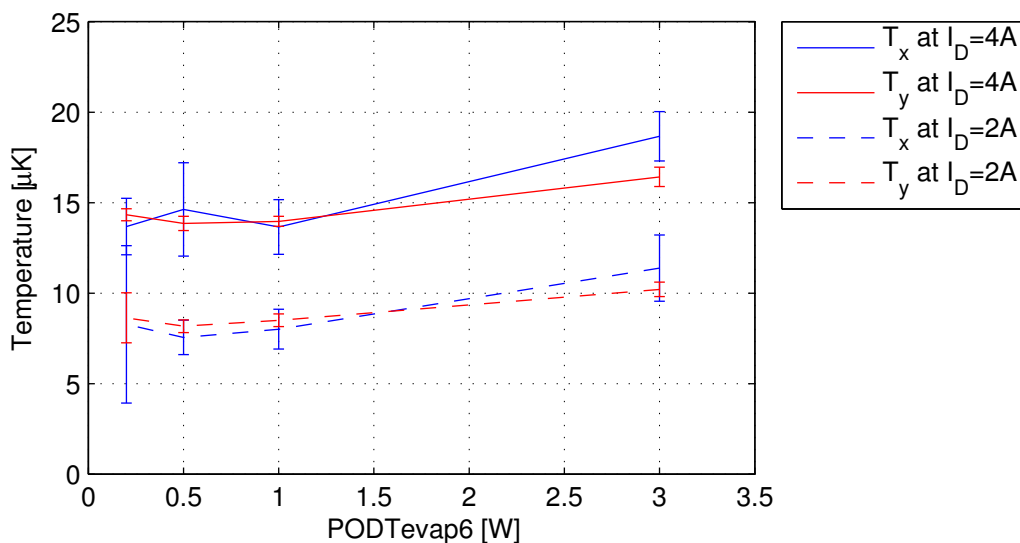


Figure 5.1: The temperature is lower in the case of low dimple laser current. The reason is simple: only atoms with small kinetic energy can still be trapped. There is only little dependence on the final ODT power. The reason can both be the magnetic potential of the barrier coils and the confinement of the dimple longitudinally, which is given by the RAYLEIGH range. In fact, it turns out in calculations of Section 6.2, having trap frequencies of  $2\pi * 287$  Hz (Barrier coils) and  $\ll 2\pi * 197$  Hz (dimple at  $I_D = 4$  A) respectively, the confinement of the magnetic field is stronger.

### 5.1 Statistics

Many physical quantities are calculated with experimental data like the number of atoms or the cloud width. The question whether some feature in that quantity has a physical meaning depends on whether the experimental data has changed by more than its standard deviation. For that

reason, we obtain statistical data loading the dimple potential 20 times in a loop with constant experimental parameters. We analyze the experimental data produced in the evaluation of the absorption pictures.

This approach includes a precise calculation of the mean number of atoms in the dimple potential.

**Cloud Width.** Figure 5.2 presents the widths  $\sigma_x$  and  $\sigma_y$  of the atomic cloud as we obtain it using the evaluation methods described in Section 3.3.

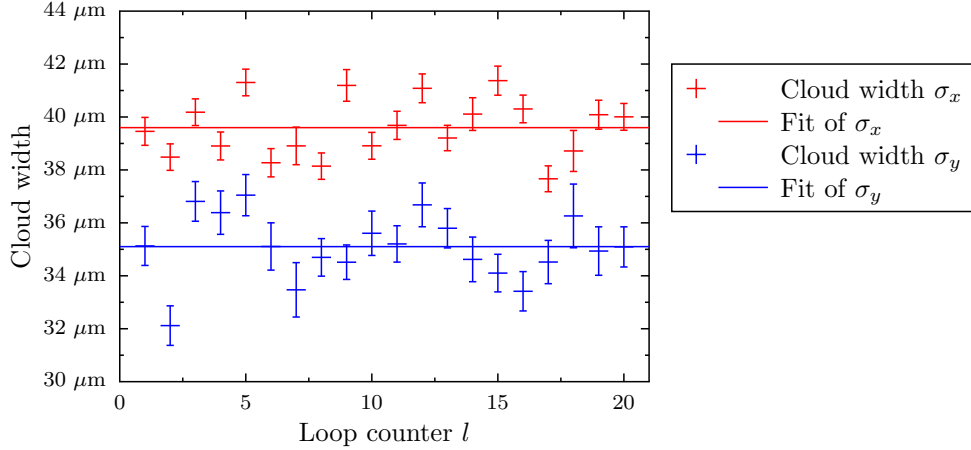


Figure 5.2: This plot shows the cloud widths in the  $\vec{e}_x$ - and  $\vec{e}_y$  directions at constant experimental parameters.

To get the average value of  $\sigma_{i \in \{x,y\}}$ , we use the errors  $\sigma_i^{\text{err}}$  from the cloud width fits as a weighting coefficient as follows:

$$\bar{\sigma}_i = \sum_l \frac{\sigma_i^{\text{err}}(l)}{\sum_l (\sigma_i^{\text{err}}(l))} \sigma_i(l). \quad (5.1)$$

$l$  denotes the loop counter. For the determination of the standard deviation, defined as  $\varsigma^*$ , we will have to calculate

$$\varsigma = \sqrt{\sum_l (\sigma_i(l) - \bar{\sigma}_i)^2}. \quad (5.2)$$

Thus, the average cloud widths with standard deviations in brackets are

$$\bar{\sigma}_x = 28.00(77) \mu\text{m} \quad (5.3)$$

$$\bar{\sigma}_y = 24.82(86) \mu\text{m}. \quad (5.4)$$

**Number of Atoms.** For the analysis of the number of atoms in Figure 5.3, we can use similar equations as (5.1) and (5.3). Three datasets are available:

- **Atom count:** The number of atoms arising from the summation of the optical density over all pixels in the region of the atomic cloud in the absorption picture.
- **Number of atoms from fit along  $\vec{e}_x$  and**

\*instead of the usual notation  $\sigma$  to prevent ambiguity with the cloud width

- **Number of atoms from fit along  $\vec{e}_y$ :** Both datasets come from Gaussian fits of the absorption picture described in Section 3.3. They include errors that depend on the quality of the imaging setup and give rise to an uncertainty in the number of atoms.

The results of the calculations are summarized in Table 5.1.

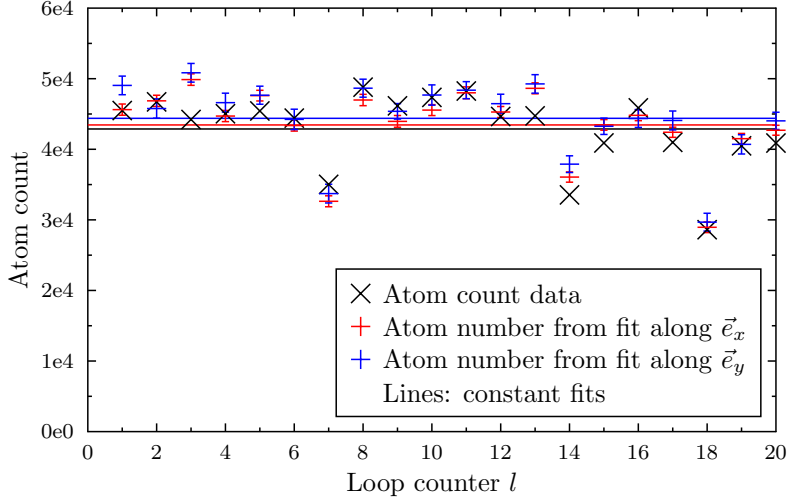


Figure 5.3: This plot shows the average number of atoms and the deviations at constant experimental parameters. Red and blue data points correspond to the numbers of atoms calculated with a Gaussian fit in  $\vec{e}_x$ - and  $\vec{e}_y$ - directions of the atomic cloud respectively. The error bars are from the errors of Figure 5.2.

Mean value and standard error of the number of atoms.		
Data type	Mean number of atoms	Standard deviation
Atom count	42 877	5 083
Fit in $\vec{e}_x$ direction	43 448	5 165
Fit in $\vec{e}_y$ direction	44 385	5 208

Table 5.1: The table shows number of atoms and their standard deviations of the three data sources described above. A discrepancy can suggest a wrong physical model which is fitted.

In conclusion, if we take the average of the numbers of atoms, we have about **44 000 atoms** trapped in the dimple. The **standard deviation is 5 000 atoms**.

## 5.2 The Temperature

We are interested in the temperature of the atomic cloud after the loading process of the dimple (for Section 6.2). For this purpose, we make time of flight (TOF) experiments as described in Section 2.1. We scan the time variable  $t_{\text{TOF}}$  from 0 to 2.5 ms and analyze the cloud width. According to Equation (2.22), the cloud width scales approximately linearly with time after some trap periods  $2\pi/\omega$ . We start the fit at

$$t_{\text{TOF}} = 400 \mu\text{s} = 2 * \frac{1}{5000 \text{ Hz}}, \quad (5.5)$$

since  $2\pi * 5000$  Hz are typical trap frequencies we measure in 4.12. The fit in Figure 5.4(a) shows that this is good approximation.

We calculate the temperatures from the slope  $a$  of the linear fit function

$$\sigma_i(t_{\text{TOF}}) = at_{\text{TOF}} + b \quad (5.6)$$

with a 2<sup>nd</sup> fit parameter  $b$  which can account for a timing offset. In the fit of  $\sigma_x(t_{\text{TOF}})$  (and  $\sigma_y(t_{\text{TOF}})$  respectively), the offset is  $b = 2.35 \mu\text{m}$  ( $2.09 \mu\text{m}$ ) which corresponds to a timing shift of  $\delta_{\text{TOF}} = 32 \mu\text{s}$  ( $31 \mu\text{s}$ ) at slopes of  $a = 73.03 \frac{\mu\text{m}}{\text{ms}}$  ( $67.23 \frac{\mu\text{m}}{\text{ms}}$ ).

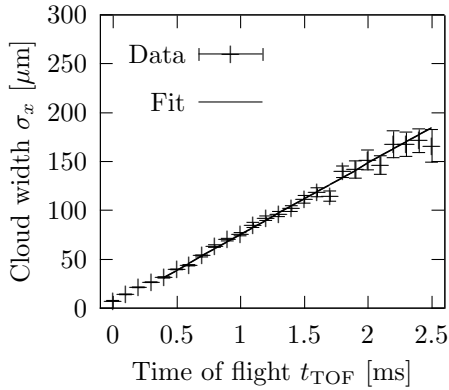
The slope is  $a = \left(\frac{\sigma_i}{t_{\text{TOF}}}\right)^2$ . Therefore, cf. Equation (2.23), the temperature can be calculated using

$$T = \frac{a^2 m}{(2k_{\text{B}})}. \quad (5.7)$$

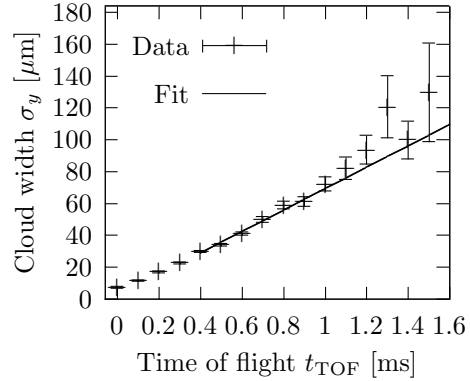
As a result, the temperatures are

$$T_x = (16.68 \pm 0.58) \mu\text{K} \quad (5.8)$$

$$T_y = (14.14 \pm 1.31) \mu\text{K} \quad (5.9)$$



(a)  $x$ -component of the cloud evolution



(b)  $y$ -component of the cloud evolution

Figure 5.4: For a temperature specification, we let the cloud expand freely and fit the cloud width (beginning at  $400 \mu\text{s}$ ) with a weighted linear regression taking the errors into account. The higher the slope, the higher was the temperature of the trapped atomic cloud. Please note the different scales. But, to compare the slopes, the aspect ratios of the axes are the same.

The Gaussian fits in the direction of  $\vec{e}_y$  are of poor quality. Probably, the aspect ratio of the absorption picture is different from 1. A thermalized gas has an isotropic velocity distribution. Therefore, after some trap periods of expansion, the aspect ratio of the expanding cloud should approach the value 1. This wrong calibration manifests most clearly in Figure 5.2, but also in the temperatures calculated here. This is why we suggest for future work\* to rescale the axes with an aspect ratio of

$$\alpha = \frac{39.598 \mu\text{m}}{35.102 \mu\text{m}} = 1.1281 \quad (5.10)$$

calculated from the aspect ratio of Figure 5.2. To keep the number of atoms in the imaging evaluation constant, the area  $\sigma_x \sigma_y$  has to stay constant:

$$\sigma'_x \sigma'_y = \sigma_x \sigma_y. \quad (5.11)$$

\*if the imaging setup stays as-is

With

$$\frac{\sigma_x}{\sigma_y} = \alpha \quad (5.12)$$

and

$$\frac{\sigma'_x}{\sigma'_y} = 1 \quad (5.13)$$

we obtain

$$\sigma'_x = \frac{1}{\sqrt{\alpha}} \sigma_x \quad (5.14)$$

$$\sigma'_y = \sqrt{\alpha} \sigma_y. \quad (5.15)$$

That means, the axes shall be scaled by

$$\text{x-Axis: } 0.9415 \quad (5.16)$$

$$\text{y-Axis: } 1.0621. \quad (5.17)$$

### 5.3 The Density Gain

For demagnetization cooling discussed in Section 2.2.2 and other spinor physics experiments, we need a high particle density. The question is to what extent the dimple potential leads to a density gain and finally which dipolar relaxation rate is present, the prerequisite of demagnetization cooling [34] [33] [28] [29].

For this analysis, we use 30 absorption pictures at a loading time when the loading process has reached its equilibrium\*. This procedure allows for a more accurate evaluation by averaging. The averaged absorption picture is printed in Figure 5.5. The absorption pictures are taken after

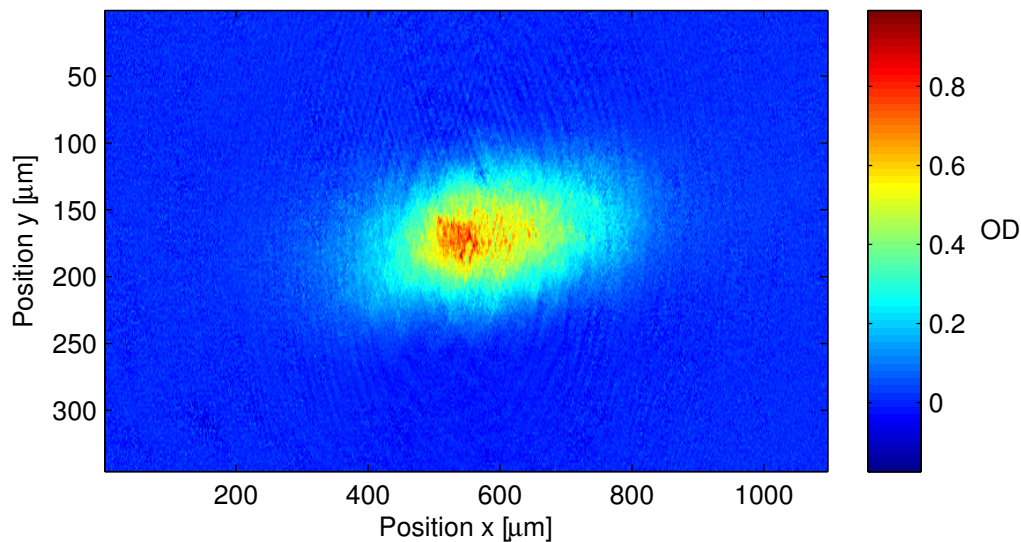


Figure 5.5: The data is an average of 30 absorption pictures.

free expansion of  $t_{\text{TOF}} = 100 \mu\text{s}$  for a moderate optical density of  $OD = 1$  at which absorption saturation and lensing effects have little impact. In the column density  $\rho_x$  of Figure 5.6, we can still distinguish the fraction of atoms originating from the dimple from the atoms outside, i.e.

\*within the limits of the standard deviations of the number of atoms and the cloud width

atoms trapped by the hybrid trap. We cannot resolve the atoms in the dimple in the column density  $\rho_y$  (Figure 5.7) because of the low fraction of atoms in the dimple in addition to the high confinement of the hybrid trap in direction  $\vec{e}_y$ . This does not render the evaluation impossible as we will see.

For the hybrid trap column density in the  $\vec{e}_x$  direction, we fit a Gaussian

$$\rho_x = \rho_{0,x}^{\text{HT}} \exp \left[ -\frac{1}{2} \left( \frac{x - x_0^{\text{HT}}}{\sigma_x^{\text{HT}}} \right)^2 \right] + c \quad (5.18)$$

with fit parameters  $\rho_{0,x}^{\text{HT}}$ ,  $x_0^{\text{HT}}$ ,  $\sigma_x^{\text{HT}}$  and  $c^{\text{HT}}$ . “HT” denotes the component of the hybrid trap and “D” will be the dimple component. For the fit, we exclude the central range where the dimple components come on top. We can also fit a bimodal Gaussian to the data, but since the imaging close to the dimple is of poor quality\*, there are large errors for the width† and the number of atoms of the dimple part. The positions of the dimple and hybrid trap can be determined by a bimodal Gaussian fit.

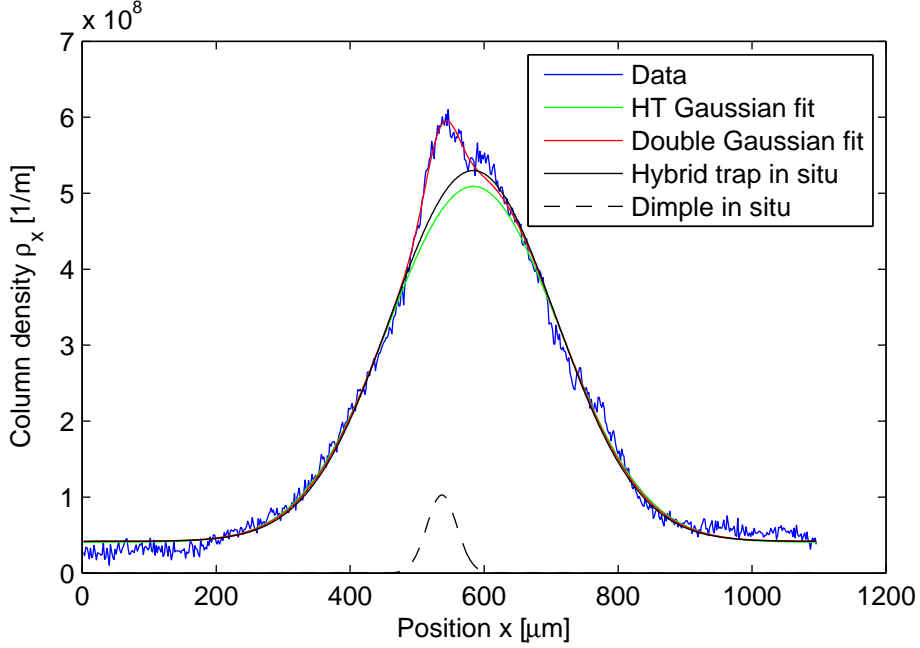


Figure 5.6: The in situ and expanded cloud (data) column densities along  $\vec{e}_x$ . Explanations and discussion are given in the text.

For the column density  $\rho_y$ , we fit a single Gaussian as well

$$\rho_y = \rho_{0,y} \exp \left[ -\frac{1}{2} \left( \frac{y - y_0}{\sigma_y} \right)^2 \right] + d \quad (5.19)$$

with fit parameters  $\rho_{0,y}$ ,  $y_0$ ,  $\sigma_y$  and  $d$ . The denotation is different from Equation (5.18) on purpose to stress that in Equation (5.18), the clouds can be distinguished.

\*We see negative optical densities at the position right of the dimple, even at low optical densities. They cause abrupt drops in the column density  $\rho_x$  seen in this data.

†The bimodal fit states a width of the dimple atomic cloud fraction which is about the same as the in situ cloud width. This is clearly wrong.

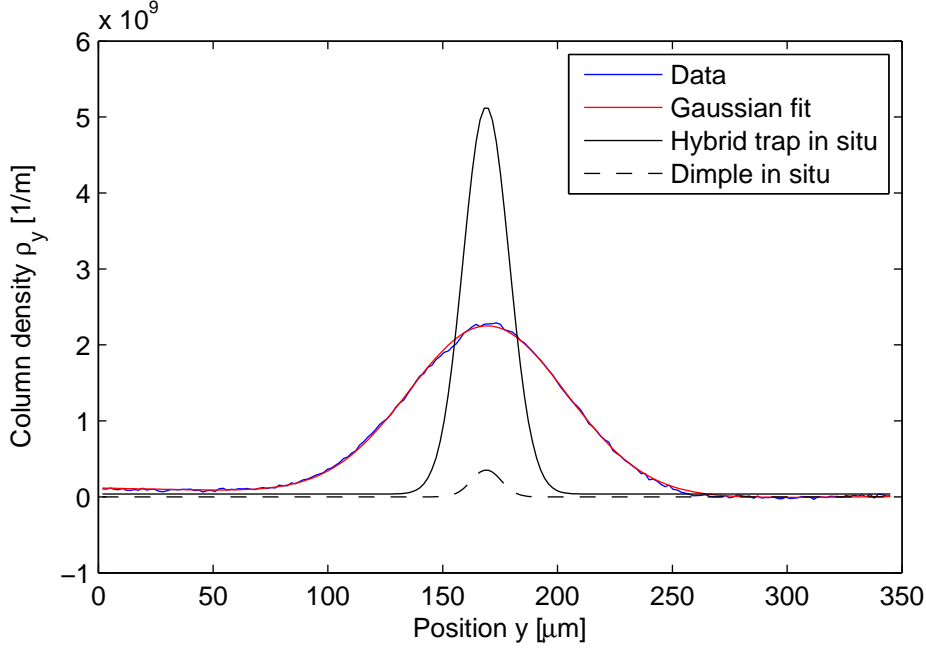


Figure 5.7: The in situ and expanded cloud (data) column densities along  $\vec{e}_y$ . Discussion in text.

The number of atoms in the dimple can be calculated. It is the area between the Gaussian fit and the data. We integrate over the range which was skipped in the fit and obtain

$$N^D = 8145. \quad (5.20)$$

For the number of atoms in the hybrid trap, We calculate the integral of the Gaussian in  $\vec{e}_x$  direction using the well known normalization factor  $\sigma\sqrt{2\pi}$  of the Gaussian function:

$$N_x^{\text{HT}} = \int_{-\infty}^{+\infty} \rho_{0,x}^{\text{HT}} \exp\left[-\frac{1}{2}\left(\frac{x-x_0^{\text{HT}}}{\sigma_x^{\text{HT}}}\right)^2\right] + c = \sqrt{2\pi}\rho_{0,x}^{\text{HT}}\sigma_x^{\text{HT}} = 149\,990 \pm 1\,040. \quad (5.21)$$

This should be similar to the integral over the  $y$ -density minus  $N^D$ :

$$N_y^{\text{HT}} = \int_{-\infty}^{+\infty} \rho_{0,y} \exp\left[-\frac{1}{2}\left(\frac{y-y_0}{\sigma_y^{\text{HT}}}\right)^2\right] + d - N^D = \sqrt{2\pi}\rho_{0,y}\sigma_y - N^D = 181\,620 \pm 1\,350. \quad (5.22)$$

We choose the inverse-error-weighted value

$$N^{\text{HT}} = 163\,730 \pm 22\,610. \quad (5.23)$$

To obtain in situ column densities, we take the trap frequencies from 4.12 at the current focal position (“8 a.c.w. turns” in that figure)

$$\omega_x^D = 2\pi * 2\,369 \text{ Hz} \quad (5.24)$$

$$\omega_y^D = 2\pi * 6\,303 \text{ Hz} \quad (5.25)$$

and the trap frequencies of the hybrid trap at  $P_{\text{ODT}} = 90 \text{ W}$  and  $I_{\text{BC}} = 1.3 \text{ A}$ , as given by equations (4.41), (4.42) and (4.43):

$$\omega_x^{\text{HT}} = \sqrt{\omega_{\text{ODT},x}^2 + \omega_{\text{BC},x}^2} = 2\pi * 289 \text{ Hz} \quad (5.26)$$

$$\omega_y^{\text{HT}} = \omega_{\text{ODT},x} = 2\pi * 5\,310 \text{ Hz}. \quad (5.27)$$

The temperature of the cloud can best be determined by the expansion dynamics of the atoms in the ODT in  $\vec{e}_y$  direction, see Figure 5.7, because we have the fastest expansion due to the high trap frequency. The temperature can be calculated with Equation (2.23) with the error coming from the standard deviation of  $\sigma_y$ :

$$T = (703 \pm 6) \mu\text{K}. \quad (5.28)$$

This is a reasonable temperature comparing it to previous work [8].

In the following part, in situ variables will be marked with a star (\*). We calculate the in situ hybrid trap cloud width using Equation (2.19):

$$\sigma_x^{\text{HT}*} = \frac{\sigma_x^{\text{HT}}}{\sqrt{1 + (\omega_x^{\text{HT}})^2 t_{\text{TOF}}^2}}. \quad (5.29)$$

The in-trap peak column density  $\rho_{0,x}^*$  is given by the integral of the Gaussian function and with the number of atoms derived above:

$$\rho_{0,x}^{\text{HT}*} = \frac{N^{\text{HT}}}{\sqrt{2\pi}\sigma_x^{\text{HT}*}}. \quad (5.30)$$

The in situ width of the atomic cloud fraction in the dimple potential is calculated with Equation (2.20), the trap frequencies  $\sqrt{(\omega_i^{\text{D}})^2 + (\omega_i^{\text{HT}})^2}$  and the temperature from above:

$$\sigma_i^{\text{D}*} = \sqrt{\frac{2k_{\text{B}}T}{m\omega_i^2}} = \sqrt{\frac{2k_{\text{B}}T}{m((\omega_i^{\text{D}})^2 + (\omega_i^{\text{HT}})^2)}}. \quad (5.31)$$

$\rho_{0,i}^{\text{D}*}$  is calculated analogue to Equation (5.30).  $\sigma_y^{\text{HT}*}$  and  $\rho_{0,i}^{\text{HT}*}$  are calculated like the respective dimple parameters, but without the summand  $(\omega_i^{\text{D}})^2$  in Equation (5.31).

The in situ positions of the two cloud fractions are given by the two positions in the bimodal fit in direction  $\vec{e}_x$  and by the position  $y_0$  of the single Gaussian fit in Equation (5.19). Now, we have all parameters for the in situ column density. However, we want the density **profile** because we want to know the peak density. The peak density will be in the plane where the foci of both the dimple laser and the ODT laser are located. We choose  $z = 0^*$ . The trap frequency in  $\vec{e}_z$  direction is

$$\omega_z^{\text{HT}} = \sqrt{\omega_{\text{ODT},z}^2 + \omega_{\text{BC},z}^2} = \sqrt{\omega_{\text{ODT},y}^2 + \omega_{\text{BC},x}^2} = 2\pi * 5\,317 \text{ Hz} \quad (5.32)$$

The contribution of the dimple can be neglected here. With the astigmatism which leads to an enlargement of the trap and taking the higher frequency of  $\omega_x^{\text{D}}$  and  $\omega_y^{\text{D}}$ , the upper limit of the dimple trap frequency can be estimated with Equation (4.26):

$$\omega_z^{\text{D}} \ll \omega_y^{\text{D}} \sqrt{\lambda/(2\pi 300 \text{ nm})} = 2\pi * 197 \text{ Hz} \ll \omega_z^{\text{HT}}. \quad (5.33)$$

The influence is even smaller than Equation (5.33) suggests, since the squared values of that equation are summed up to the (squared) total trap frequency. Therefore, both atomic cloud fractions have the same confinement in  $\vec{e}_z$  direction. The respective width is:

$$\sigma_z^* = \sqrt{\frac{2k_{\text{B}}T}{m(\omega_z^{\text{HT}})^2}}. \quad (5.34)$$

---

\*We could as well have chosen any other plane that includes all points on the  $x$ -axis where both foci are located, but we choose the same point of view as the imaging system.

Now, we have all information for the 3-dimensional density distribution

$$\mathbb{R}^3 \rightarrow \mathbb{R}, (x, y, z) \mapsto n \quad (5.35)$$

set up by the multiplication of three Gaussian functions. The positions and widths are already given by the in situ calculations and the coefficient is derived from the normalization condition applied to the three Gaussian factors corresponding to the three dimensions.

$$n_0 = \frac{N}{(2\pi)^{3/2} \sigma_x^* \sigma_y^* \sigma_z^*} \quad (5.36)$$

We calculate this factor for both the dimple and the ODT part. The resulting density is the sum of both functions. It is visualized in Figure 5.8 for  $z = 0$ .

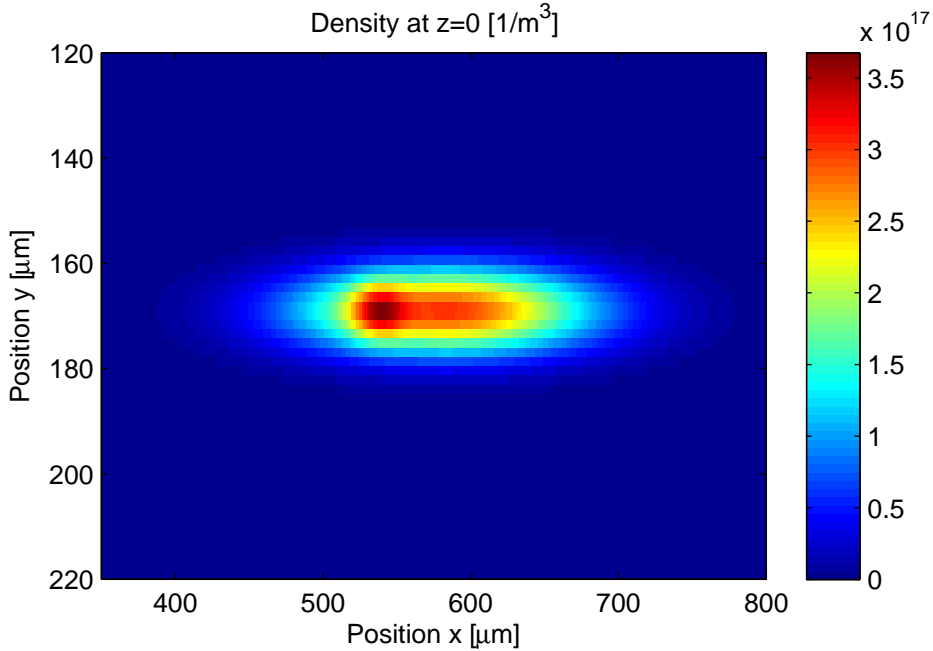


Figure 5.8: The in situ density profile at  $z = 0$ . For explanations, see text.

The maximum density in the dimple is  $n_0^D = 3.68 * 10^{17} \text{ m}^{-3}$ . Compared to  $n_0^{\text{HT}} = 3.03 * 10^{17} \text{ m}^{-3}$  in the hybrid trap, the dimple increases the maximum density by 21%.

At that peak density, dipolar relaxations take place at a rate of

$$\Gamma_{s_1} = 0.52, \text{ Hz} \quad (5.37)$$

for a single spin flip using the equations of Section 2.2.2. The temperature was taken from Equation (5.28) and the magnetic field was set to the most efficient value for demagnetization cooling

$$B = 1.31 * \frac{k_B T}{g_S \mu_B} = 6.9 \text{ G.} \quad (5.38)$$

At the mean thermal relative speed of

$$\bar{v} = 4 \sqrt{\frac{k_B T}{m\pi}} = 0.7566 \frac{\text{m}}{\text{s}} \quad (5.39)$$

the double spin flip  $s_2$  cannot occur classically since the kinetic energy of the colliding particles is lower than the potential of the final state:

$$E_{\text{kin}} < 2 * g_S \mu_B B. \quad (5.40)$$

For an estimation of the relaxation rate, the single spin flip process is sufficient. Being in the order of typical experimental time scales, the relaxation rate is promising for the realization of demagnetization cooling. However, as these measurements are conducted right after the loading process, plain evaporation has not been taken into account. Since plain evaporation takes place on a time scale of 100 ms and the demagnetization on a time scale of 1 s (see Chapter 7), the evolution of the parameters is dominated by the plain evaporation process. A simulation for demagnetization cooling after plain evaporation with a more detailed analysis is performed in Chapter 7.

## Chapter 6

# The Stability of the Setup

For an investigation whether or not the setup is suited for further fascinating experiments, one other crucial aspect besides the trap depth and the peak density is the stability. A good stability manifests itself in long lifetimes of atoms held by the dimple potential, and in the ability to reach low temperatures using forced evaporation.

### 6.1 Lifetime

We load the atoms in the dimple using the ODT ramp described in Table 3.6.

Figure 6.1 shows the evolution of the number of atoms in the dimple after the loading process. The exponential fit

$$N(t) = N_0 e^{-t/\tau} + c \quad \text{with } N_0, \tau_D, c: \text{ fit parameters} \quad (6.1)$$

of the atom count is performed after some time to reduce the influence of plain evaporation on the lifetime. We derive a lifetime  $\tau_D = 13.9$  s.

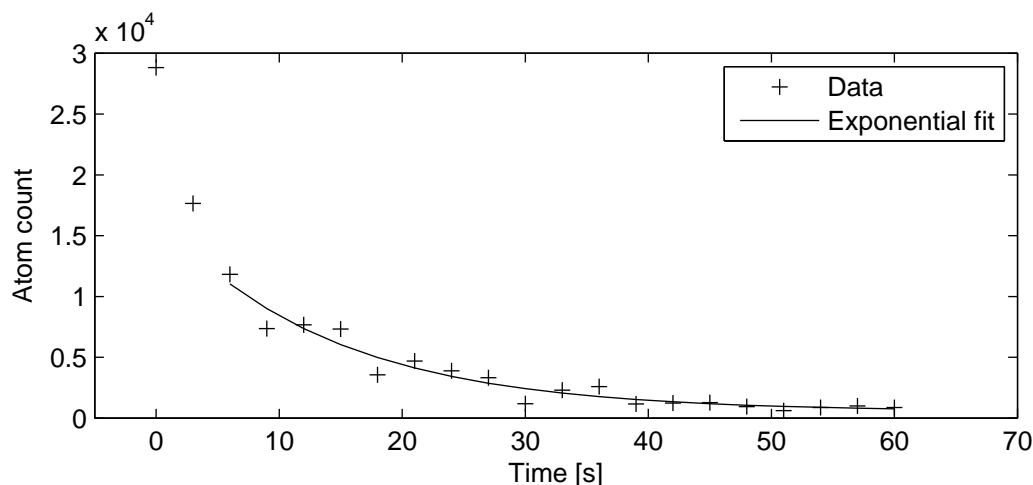


Figure 6.1: The figure shows the number of atoms in the dimple after a hold time corresponding to the  $x$ -axis. The lifetime of the atomic cloud is determined with the exponential fit.

This needs to be compared to the lifetime of atoms in the ODT. For the lifetime in the ODT, the same procedure has been performed as above. Data and the exponential fit are plotted in Figure 6.2. The lifetime in the ODT is  $\tau_{\text{ODT}} = 23.7$  s.

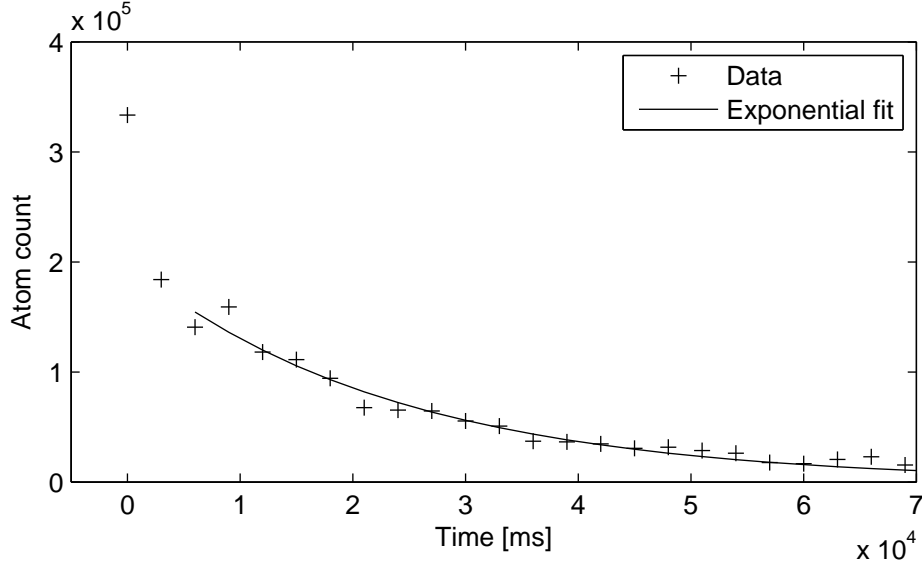


Figure 6.2: The figure shows the number of atoms in the ODT after a hold time corresponding to the  $x$ -axis. The lifetime of the atomic cloud is determined with the exponential fit. Note the difference in the atom count scale of one magnitude.

In summary, the lifetime  $\tau_D$  of atoms in the dimple potential is 41 % smaller than the lifetime  $\tau_{\text{ODT}}$  in the ODT. If  $\tau_D$  is high enough depends on the duration of the experiments. In this work, the maximum hold time was 5 s in a parametric heating experiment.

One reason for the lower lifetime is the high density. For 44 000 atoms at 15  $\mu\text{K}$  in the dimple that we measured in subsections 5.1 and 5.2, and for cloud widths resulting from the confinement of the dimple and the barrier coils, the density in the center of the cloud is

$$n_0 = \frac{44\,000}{(2\pi)^{(3/2)}\sigma_x\sigma_y\sigma_z} \approx 1.0 * 10^{19} \frac{1}{\text{m}^3}. \quad (6.2)$$

For the number of atoms of Figure 6.1, the same calculation has been performed in Figure 6.3. Since plain evaporation leads to a decrease in temperature – see Section 6.2 and Table 3.6 – Figure 6.3 only gives a lower bound of the peak density.

## 6.2 Forced Evaporation

We conduct a series of time of flight experiments with evaporation ramps described in Table 3.6 of Chapter 3. The time of flight experiments are conducted at different final dimple laser powers to vary the temperature of the remaining atomic cloud in the dimple. In that way, we can investigate once more if the setup is stable. The deeper the temperature drops, the better is the stability of the setup since vibrations, for instance, would lead to the opposing effect, heating. The heating effects are always present, but at low temperatures, they have more influence.

For a good accuracy at low particle numbers we take between 20 and 50 absorption pictures after a constant expansion time between  $t_{\text{TOF}} = 3$  ms and 5 ms.

To determine whether the temperatures are close to the phase transition to a BEC, they can be compared to the critical temperature from Equation (2.11)

$$T_C = \frac{\hbar}{k_B} \left( \frac{\omega_x\omega_y\omega_z N}{\zeta(3)} \right)^{1/3} \left( 1 - 0.7275 \frac{1}{N^{1/3}} \right) \quad (6.3)$$

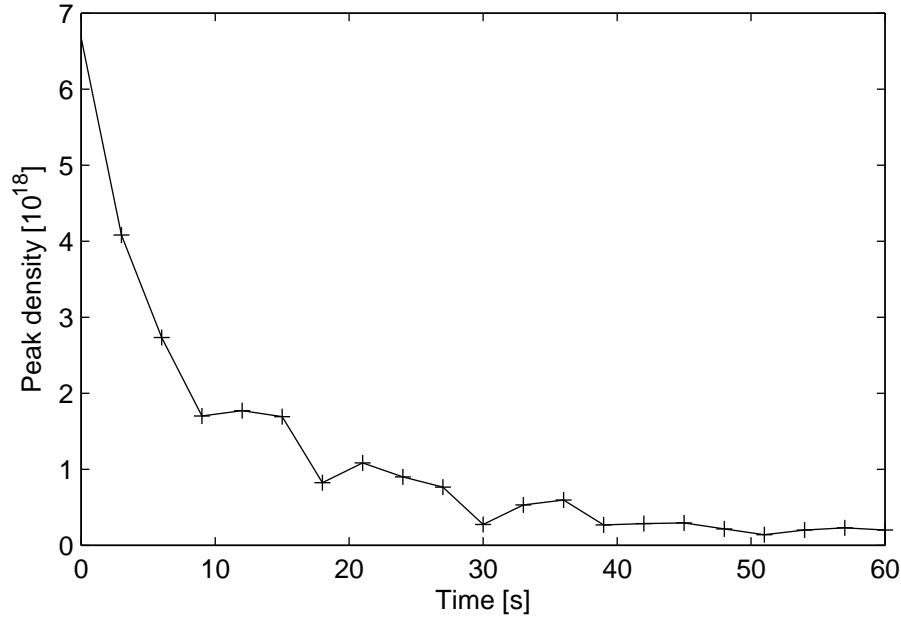


Figure 6.3: The figure shows the bottom estimation of the peak density of atoms in the dimple. The number of atoms is from Figure 6.1 and the temperature is set to the temperature after the loading process (from Section 5.2).

which is extended here with a correction factor in the second brace which accounts for the finite number of atoms [14]. The trap frequencies  $\omega_i$  have been studied in the last sections and the number of atoms  $N$  is derived from the absorption picture. We see in Figure 6.4 that the temperatures approach the critical temperatures. The fact that the laser could not be switched off completely in these experiments – the remaining laser power during expansion is 22 mW – leads to a force that prevents the atoms from expanding and thus falsifies the absorption pictures. If we compare Figures 6.5 and 6.6, we see bimodal Gaussian column densities in both cases that resemble the shape of a BEC. The fact that the central density enhancement is still present at higher temperatures is an indication for no phase transition. The temperatures are obtained by a fit of the wings of the atomic cloud. Thereby, we reduce the error of the temperatures.

We can state with this experiment that deep temperatures can be reached. This is a sign of high stability.

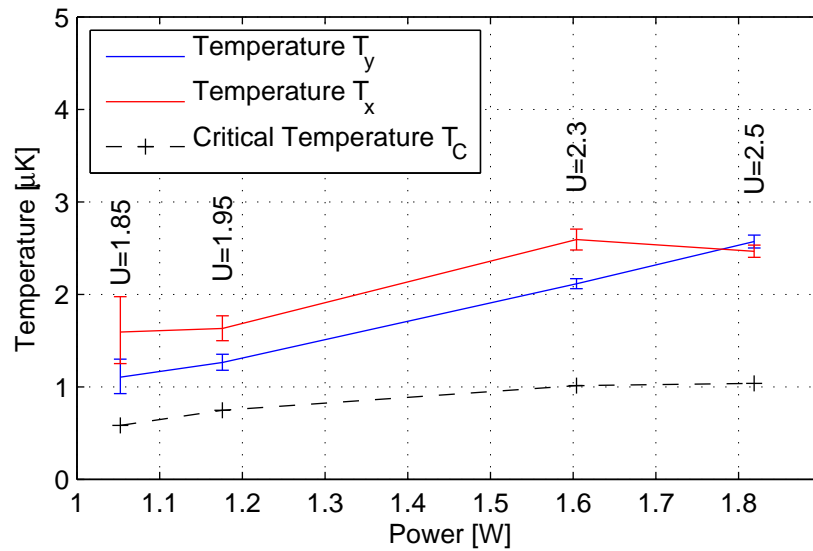


Figure 6.4: The temperature of the atomic cloud decreases when we decrease the final power of the evaporation ramp. The values of “U” are the control voltages  $U_{\text{Dimple}}$  of the AOM driver which lead to that final power on the  $x$ -axis. We see that the temperature curves approach the critical temperature  $T_C$ .

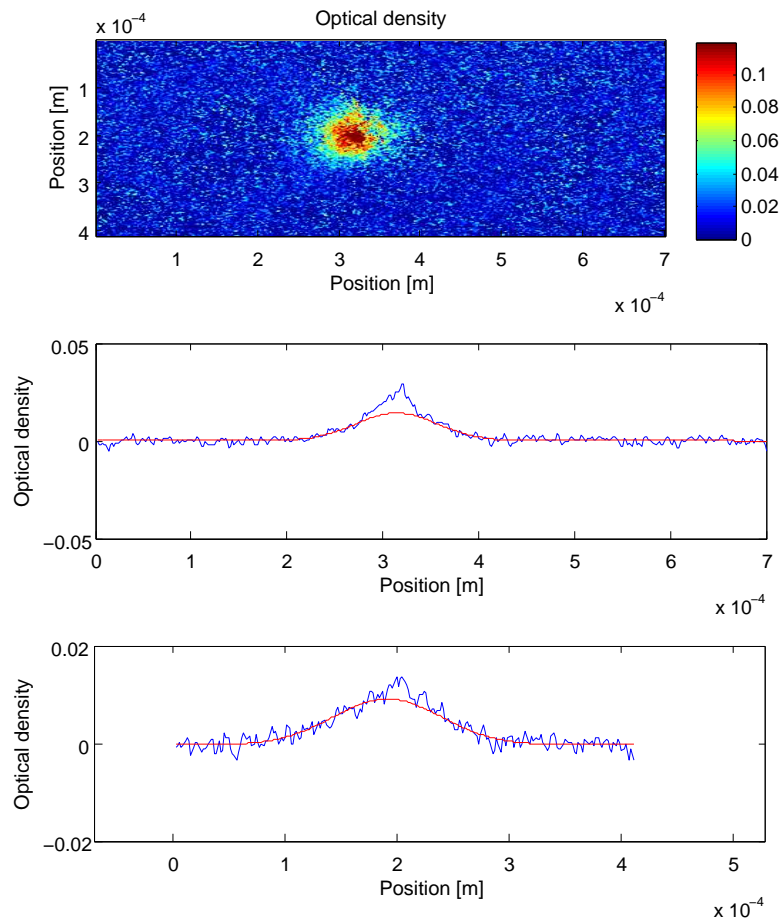


Figure 6.5: The column densities after the time of flight of 3 ms show still shapes that resembles those of condensates. However, if we go to lower powers (0.93 W), we cannot see a thermal cloud any more. Since it is impossible to have a pure condensate, we think the remaining laser intensity during expansion falsifies the absorption pictures.

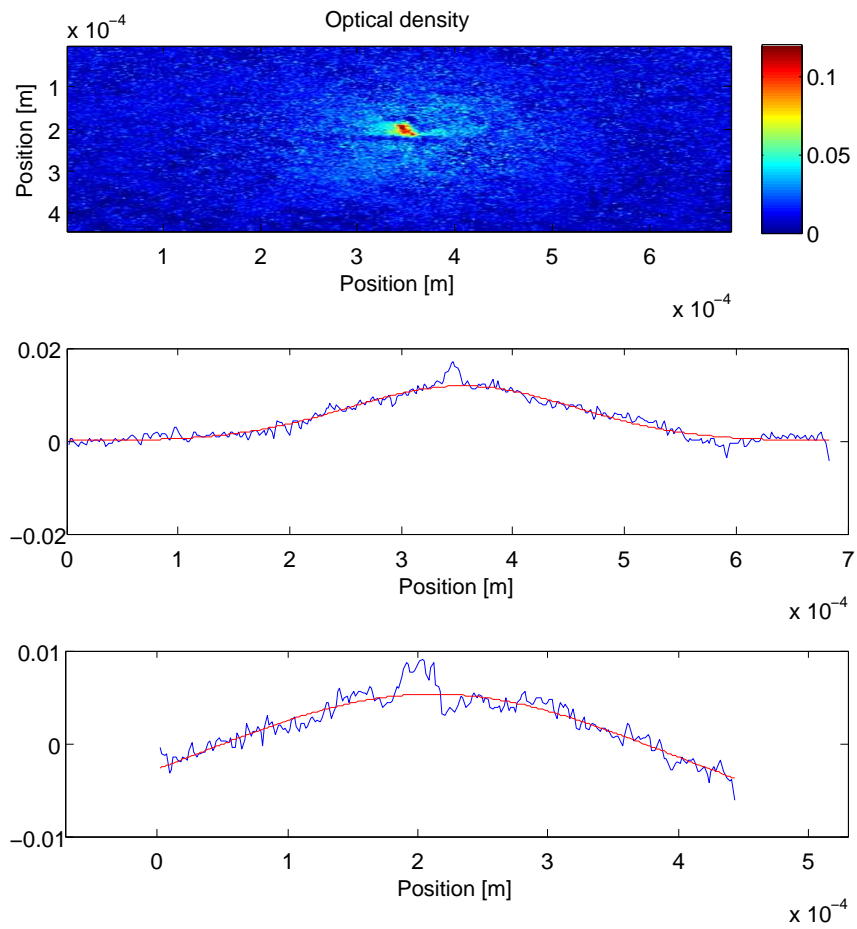


Figure 6.6: The high density in the center of the cloud is most likely due to the remaining laser intensity during the expansion time of 5 ms.

## Chapter 7

# Prediction for Demagnetization Cooling

This chapter investigates the feasibility of demagnetization cooling in our experiment with simulations based on the loading parameters. The performances of the setup including and excluding the dimple will be opposed to predict benefits.

**Adiabatic Expansion** We start at the steady state condition of the atomic cloud in a hybrid optical dipole and magnetic trap. The characterizing start parameters are the temperature  $T_1$  and the density  $n_1 = \frac{N}{V_1}$ . In order to cool the cloud with the highest efficiency, we have to satisfy the condition  $\eta_b = 1.31$  in the equation

$$B = \eta_b \frac{k_B T}{g_S \mu_B} \quad (7.1)$$

This is possible by varying the magnetic field  $B$ . However, the temperature is dependent on the magnetic field, since the latter provides the confinement in the  $\vec{e}_z$  direction. If we change the magnetic field slowly compared to the time scale of the elastic scattering rate, which is between 130 and 490 Hz [32], the particles are always in thermal equilibrium, hence we perform an adiabatic process in which the phase space density stays constant.

$$\mathcal{D}_1 = \mathcal{D} \quad (7.2)$$

With equations (2.13) and (2.12) this writes

$$\frac{V}{V_1} = \left( \frac{T_1}{T} \right)^{3/2} \quad (7.3)$$

since the particle number is conserved  $N_1 = N$ . As the cloud expands in one direction, the left side of Equation (7.3) is

$$\frac{V}{V_1} = \frac{\sigma_z}{\sigma_{z,1}} = \sqrt{\frac{T}{T_1}} \frac{\omega_1}{\omega} = \sqrt{\frac{TB_1}{T_1 B}}. \quad (7.4)$$

where we have used the proportionalities of the cloud volumes

$$V \propto \sigma_z \quad \text{and} \quad V_1 \propto \sigma_{z,1}, \quad (7.5)$$

of the widths in  $\vec{e}_z$  direction given by the trap frequencies  $\omega$  and  $\omega_1$  cf. Equation (2.20)

$$\sigma_z \propto \frac{\sqrt{T}}{\omega} \quad \text{and} \quad \sigma_{z,1} \propto \frac{\sqrt{T_1}}{\omega_1} \quad (7.6)$$

and finally the proportionalities of the trap frequencies to the square roots of the magnetic fields  $B$  and  $B_1$

$$\omega \propto \sqrt{B} \quad (7.7)$$

This is derived from  $\omega \propto \sqrt{I}$  [32] and the linear dependence of the magnetic field  $B$  on the current  $I$  through the magnetic coils. Let us substitute Equation (7.4) into Equation (7.3).

$$\frac{B_1}{B} = \left( \frac{T_1}{T} \right)^4 \quad (7.8)$$

The system of equations (7.8) and (2.40) can be solved in terms of  $B$  and  $T$ , which will be the final parameters of the adiabatic expansion and the ideal start parameters of the demagnetization cooling.

$$B = \left( \frac{1.31k_B T_1}{g_S \mu_B} \right)^{4/3} \frac{1}{(B_1)^{1/3}} \quad (7.9)$$

$$T = \left( \frac{1.31k_B (T_1)^4}{g_S \mu_B B_1} \right)^{1/3} \quad (7.10)$$

The density of the system after the adiabatic expansion is

$$n = n_1 \frac{1/V}{1/V_1} = n_1 \frac{V_1}{V} = n_1 \sqrt{\frac{T_1 B}{T B_1}} = \sqrt{\frac{1.31k_B T_1}{g_S \mu_B B_1}}. \quad (7.11)$$

With the conditions of [8]  $n_1 = 5.8 * 10^{17} \text{ m}^{-3}$ ,  $N = 2.3 * 10^5$ ,  $T_1 = 200 \mu\text{K}$ ,  $B_1 = 10 * 10^{-4} \text{ T}$  (10 G) and the phase space density\* of  $\mathcal{D} = 3 * 10^{-6}$  we calculate

$$T = 116 \mu\text{K} \quad (7.12)$$

$$B = 1.13 \text{ G} \quad (7.13)$$

$$n = 2.56 * 10^{17} \text{ m}^{-3} \stackrel{\text{def.}}{=} n_{\text{HT}} \quad (7.14)$$

as start parameters for the demagnetization cooling process.

**Dipolar Relaxation Rate** The condition for demagnetization cooling is a dipolar relaxation rate which is at least in the order of magnitude of the decay rate of the atomic cloud.

$$\Gamma = 0.17 \frac{1}{s} \quad (7.15)$$

It is realistic that with the dimple, the density after the adiabatic expansion is double as high:  $n = 2n_{\text{HT}}$ . We calculate

$$\Gamma = 0.35 \frac{1}{s} \quad (7.16)$$

for this density. The relaxation rates are one order of magnitude larger than the decay rate of

$$\frac{1}{\tau_{\text{ODT}}} \approx 0.042 \frac{1}{s} \ll \Gamma \quad (7.17)$$

which is calculated with the life time  $\tau_{\text{ODT}}$  of Section 6.1.

The prerequisite of demagnetization cooling is hence fulfilled.

---

\*The phase space density is only used here for the validation of the algebraic conversions.

**Cooling Rate** The performance of demagnetization cooling will be predicted according to [19]. The temperature slope can be estimated

$$\begin{aligned} \dot{T} &\approx -\frac{2}{3/2 + \alpha} \sqrt{\frac{k_B}{\pi m}} \frac{(\mu_0(2\mu_B)^2 m)^2}{30\pi\hbar^4} S^2 [(1 + \eta_b)S + (2 + 4\eta_b)e^{-\eta_b}] \eta_b e^{-\eta_b} n T^{3/2} \\ &\approx -5.1 \frac{\mu\text{K}}{\text{s}} \end{aligned} \quad (7.18)$$

for a harmonic trap  $U(x, y, z) = c_x x^{n_1} + c_y y^{n_2} + c_z z^{n_3}$  with  $n_1 = n_2 = n_3 = 2$ ,  $\alpha = \sum_j \frac{1}{n_j} = 3/2$ .

For a dimple trap,  $\alpha$  is larger. We assume a trap

$$U(x, y, z) = c_x x^{1/2} + c_y y^{1/2} + c_z z^2 \quad (7.19)$$

which is harmonic in  $\vec{e}_z$  direction but has a square root shape in  $\vec{e}_x$  and  $\vec{e}_y$  directions. In this case,  $\alpha = 9/2$ . This leads to a reduced temperature slope  $\dot{T} \approx 2.6 \frac{\mu\text{K}}{\text{s}}$ , but the density would be higher in case of the dimple trap, thus we perform this calculation once more for double the density and calculate the same slope as for the harmonic trap,  $\dot{T} \approx 5.1 \frac{\mu\text{K}}{\text{s}}$ . The main advantage of the dimple trap becomes evident in the evolution of the temperature. From the temperature dependence  $n \propto T^{-\alpha}$  [19] we deduce

$$\text{for harmonic traps: } nT^{3/2} \propto T^{-3/2}T^{3/2} = 1 \quad (7.20)$$

$$\text{for dimple traps: } nT^{3/2} \propto T^{-9/2}T^{3/2} = T^{-3} \quad (7.21)$$

a constant slope in the temperature evolution in a harmonic trap and in case of the dimple trap a cooling rate that amplifies with time which we refer to as *runaway behavior*. For the dimple trap, the resultant nonlinear differential equation  $\dot{T} \propto T^{-3}$  in Equation (7.18) is solved numerically and the solution  $T(t)$  is plotted in Figure 7.1 for the densities  $n = n_{\text{HT}}$  and  $n = 2n_{\text{HT}}$  together with the time evolution of the temperature in a harmonic trap.

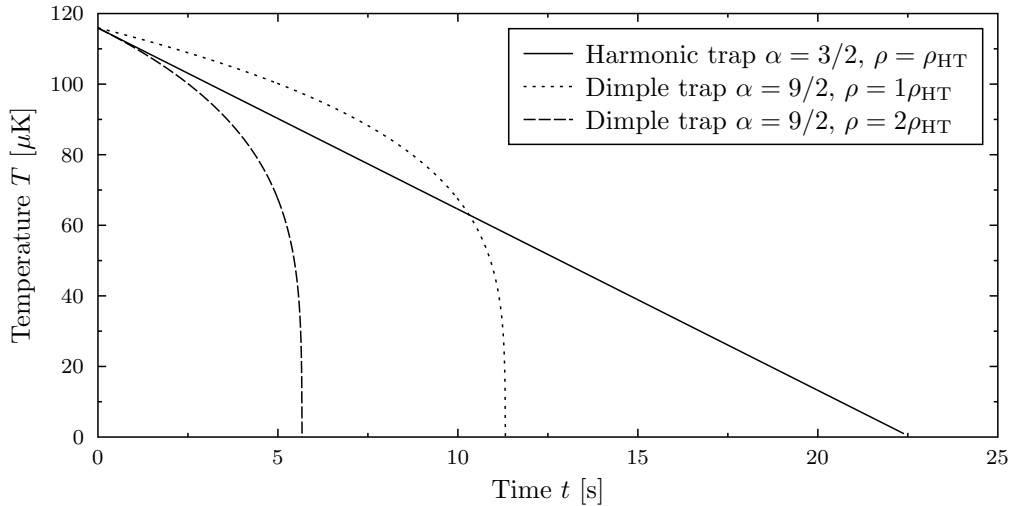


Figure 7.1: Theoretical time evolution of the temperature in the demagnetization cooling process. The solid line estimates the temperature in a harmonic trap potential, whereas the dashed lines predict the temperatures for a dimple trap at a density equal to the density of the harmonic trap (short dashes) and at double the density (long dashes). The temperature in a dimple trap shows a *runaway behavior*, i.e. an amplification of the cooling power  $\dot{T}$  in time.

The result of this simulation is convincing: If realized, this scheme would lead to a condensation after a few seconds without losses. Large condensates of more than 200 000 atoms could be BOSE-condensed.

For the simulation, the adiabatic expansion has been set after plain evaporation. One could keep higher numbers of atoms if this expansion was performed during plain evaporation since the expansion reduces the temperature.

## Chapter 8

# Summary and Outlook

We have presented the setup of a dimple trap and pointed out the difficulties, one of which is the astigmatism due to the operation on the same axis of incidence as the imaging laser. The pointing stability could be ensured by the use of two frequencies in the AOM.

Being able to cool an atomic cloud in the dimple close to degeneracy, we have shown that the dimple setup is stable and thus useful for future experiments. The life time of  $\tau_D = 13.9$  s is satisfactory for many experiments. The high density of up to  $10^{19} \frac{1}{\text{m}^3}$  might limit the life time.

A comprehensive understanding has been established of the particle dynamics in the potential created by the magnetic field, by the ODT and by the dimple. We obtained formulae describing the dependence of the trap frequencies on the beam radii in both directions for an astigmatic beam. In combination with the measurements, these formulae provide the trap depth as well as the geometry of the dimple. The trap depth is about  $400 \mu\text{K}$ . For the continuous loading scheme presented in [31], the trap depth needs to be six times higher than the kinetic energy of the incident particle beam. This mechanism can most likely not be studied without modifications, because the trap depth coincides approximately with the kinetic energy of the incident atomic beam. The most obvious optimization would be to reduce the beam waist using a different telescope system ( $f_3$  and  $f_4$ ) or to remove the dichroic mirror  $\text{DCM}_1$ . For the latter case, one could perform absorption imaging from another direction.

The dimple enhances the maximum density after the loading process by 21 %. After plain evaporation, this factor should increase since the temperature decreases. Inelastic dipolar collisions take place at these conditions with a rate of  $\Gamma_{s_1} = 0.52$ , Hz for single spin flips. For a simulation of the cooling performance, one has to consider plain evaporation which leads to a temperature drop. Since the efficiency of demagnetization cooling is best at  $\frac{g_S \mu_B B}{k_B T} \approx 1.31$ , the magnetic field has to be adjusted. The simulations show a better cooling performance for the dimple traps since the temperature dependence of the density is different. A *runaway* regime can be reached where the temperature during the cooling process diverges to minus infinity mathematically. Physically, the critical temperature could be reached within seconds.

# Bibliography

- [1] A. Aghajani-Talesh, M. Falkenau, V. V. Volchkov, L. E. Trafford, T. Pfau, and A. Griesmaier. Laser cooling of a magnetically guided ultracold atom beam. *New Journal of Physics*, 12(6):065018, 2010.
- [2] G. E. Astrakharchik and Y. E. Lozovik. Super-tonks-girardeau regime in trapped one-dimensional dipolar gases. *Phys. Rev. A*, 77:013404, Jan 2008.
- [3] D. Belkić. *Principles of quantum scattering theory*. Series in atomic and molecular physics. Institute of Physics, 2004.
- [4] P. Christian. Stabilisierung eines lasersystems zur laserkühlung von chromatomen, 2009.
- [5] C. J. Christopher Foot. *Atomic Physics*. Oxford University Press, 2005.
- [6] M. Falkenau. Chromium atoms in a deep optical dipole trap, 2008.
- [7] M. Falkenau. *Continuous Loading of an Optical Dipole Trap*. PhD thesis, Universität Stuttgart, 2011.
- [8] M. Falkenau, V. V. Volchkov, J. Rührig, A. Griesmaier, and T. Pfau. Continuous loading of a conservative potential trap from an atomic beam. *Phys. Rev. Lett.*, 106:163002, Apr 2011.
- [9] M. Fattori, T. Koch, S. Goetz, A. Griesmaier, S. Hensler, J. Stuhler, and T. Pfau. Demagnetization cooling of a gas. *Nat Phys*, 2(11):765–768, Nov 2006.
- [10] B. Fröhlich, T. Lahaye, B. Kaltenhäuser, H. Kübler, S. Müller, T. Koch, M. Fattori, and T. Pfau. Two-frequency acousto-optic modulator driver to improve the beam pointing stability during intensity ramps. *Review of Scientific Instruments*, 78(4):043101, 2007.
- [11] K. Góral, L. Santos, and M. Lewenstein. Quantum phases of dipolar bosons in optical lattices. *Phys. Rev. Lett.*, 88:170406, Apr 2002.
- [12] S. Götz. Demagnetization cooling in an ultracold chromium gas, 2006.
- [13] A. Greiner, J. Sebastian, P. Rehme, A. Aghajani-Talesh, A. Griesmaier, and T. Pfau. Loading chromium atoms in a magnetic guide. *Journal of Physics B: Atomic, Molecular and Optical Physics*, 40(5):F77, 2007.
- [14] A. Griesmaier. *Dipole-dipole interaction in a degenerate quantum gas: Bose-Einstein condensation of chromium atoms*. PhD thesis, Universität Stuttgart, 2006.
- [15] A. Griesmaier, A. Aghajani-Talesh, M. Falkenau, J. Sebastian, A. Greiner, and T. Pfau. A high flux of ultra-cold chromium atoms in a magnetic guide. *Journal of Physics B: Atomic, Molecular and Optical Physics*, 42(14):145306, 2009.

- [16] A. Griesmaier, J. Stuhler, T. Koch, M. Fattori, T. Pfau, and S. Giovanazzi. Comparing contact and dipolar interactions in a bose-einstein condensate. *Phys. Rev. Lett.*, 97:250402, Dec 2006.
- [17] R. Grimm, M. Weidemüller, and Y. B. Ovchinnikov. Optical dipole traps for neutral atoms. volume 42 of *Advances In Atomic, Molecular, and Optical Physics*, pages 95 – 170. Academic Press, 2000.
- [18] S. Hensler. *Wechselwirkungen in ultrakalten dipolaren Gasen*. PhD thesis, Universität Stuttgart, 2004.
- [19] S. Hensler, A. Greiner, J. Stuhler, and T. Pfau. Depolarisation cooling of an atomic cloud. *EPL (Europhysics Letters)*, 71(6):918, 2005.
- [20] W. Ketterle. Observation of feshbach resonances in a bose-einstein condensates. *Nature*, 392, 1998.
- [21] W. Ketterle, D. S. Durfee, and D. M. Stamper-Kurn. Making, probing and understanding bose-einstein condensates, 1999.
- [22] T. Koch, T. Lahaye, J. Metz, B. Fröhlich, A. Griesmaier, and T. Pfau. Stabilization of a purely dipolar quantum gas against collapse. *Nature Physics*, 4:218–222, 2008.
- [23] T. Lahaye, C. Menotti, L. Santos, M. Lewenstein, and T. Pfau. The physics of dipolar bosonic quantum gases. *Reports on Progress in Physics*, 72(12):126401, 2009.
- [24] T. Lahaye, J. Metz, B. Fröhlich, T. Koch, M. Meister, A. Griesmaier, T. Pfau, H. Saito, Y. Kawaguchi, and M. Ueda. *d*-wave collapse and explosion of a dipolar bose-einstein condensate. *Phys. Rev. Lett.*, 101:080401, Aug 2008.
- [25] W. Li, T. Pohl, J. M. Rost, S. T. Rittenhouse, H. R. Sadeghpour, J. Nipper, B. Butscher, J. B. Balewski, V. Bendkowsky, R. Löw, and T. Pfau. A homonuclear molecule with a permanent electric dipole moment. *Science*, 334(6059):1110–1114, 2011.
- [26] M. Lu, N. Q. Burdick, S. H. Youn, and B. L. Lev. Strongly dipolar bose-einstein condensate of dysprosium. *Phys. Rev. Lett.*, 107:190401, Oct 2011.
- [27] S. Müller, J. Billy, E. A. L. Henn, H. Kadau, A. Griesmaier, M. Jona-Lasinio, L. Santos, and T. Pfau. Stability of a dipolar bose-einstein condensate in a one-dimensional lattice. *Phys. Rev. A*, 84:053601, Nov 2011.
- [28] B. Pasquiou, E. Maréchal, G. Bismut, P. Pedri, L. Vernac, O. Gorceix, and B. Laburthe-Tolra. Spontaneous demagnetization of a dipolar spinor bose gas in an ultralow magnetic field. *Phys. Rev. Lett.*, 106:255303, Jun 2011.
- [29] B. Pasquiou, E. Marechal, L. Vernac, O. Gorceix, and B. Laburthe-Tolra. Thermodynamics of a Bose Einstein condensate with free magnetization. *ArXiv e-prints*, Oct. 2011.
- [30] C. Pethick and H. Smith. *Bose-Einstein condensation in dilute gases*. Cambridge University Press, New York, 2008.
- [31] C. F. Roos, P. Cren, D. Guéry-Odelin, and J. Dalibard. Continuous loading of a non-dissipative atom trap. *Europhysics Letters*, 61:187, 2003.
- [32] J. Rührig. Continuous loading of an optical dipole trap using ultra cold chromium atoms, 2011.
- [33] L. Santos, M. Fattori, J. Stuhler, and T. Pfau. Spinor condensates with a laser-induced quadratic zeeman effect. *Phys. Rev. A*, 75:053606, May 2007.

- 
- [34] L. Santos and T. Pfau. Spin-3 chromium bose-einstein condensates. *Phys. Rev. Lett.*, 96:190404, May 2006.
- [35] J. Stuhler, A. Griesmaier, J. Werner, T. Koch, M. Fattori, and T. Pfau. Ultracold chromium atoms: from Feshbach resonances to a dipolar Bose-Einstein condensate. *Journal of Modern Optics*, 54(5):647–660, 2007.
- [36] J. Walraven. *Elements of Quantum Gases: Thermodynamic and Collisional Properties of Trapped Atomic Gases*. unpublished, Les Houches, 2010.
- [37] J. Werner, A. Griesmaier, S. Hensler, J. Stuhler, T. Pfau, A. Simoni, and E. Tiesinga. Observation of feshbach resonances in an ultracold gas of  $^{52}\text{Cr}$ . *Phys. Rev. Lett.*, 94:183201, May 2005.